Volume 53
Number 23
7 December 2024
Pages 11253–11694

Chem Soc Rev

Chemical Society Reviews

rsc.li/chem-soc-rev

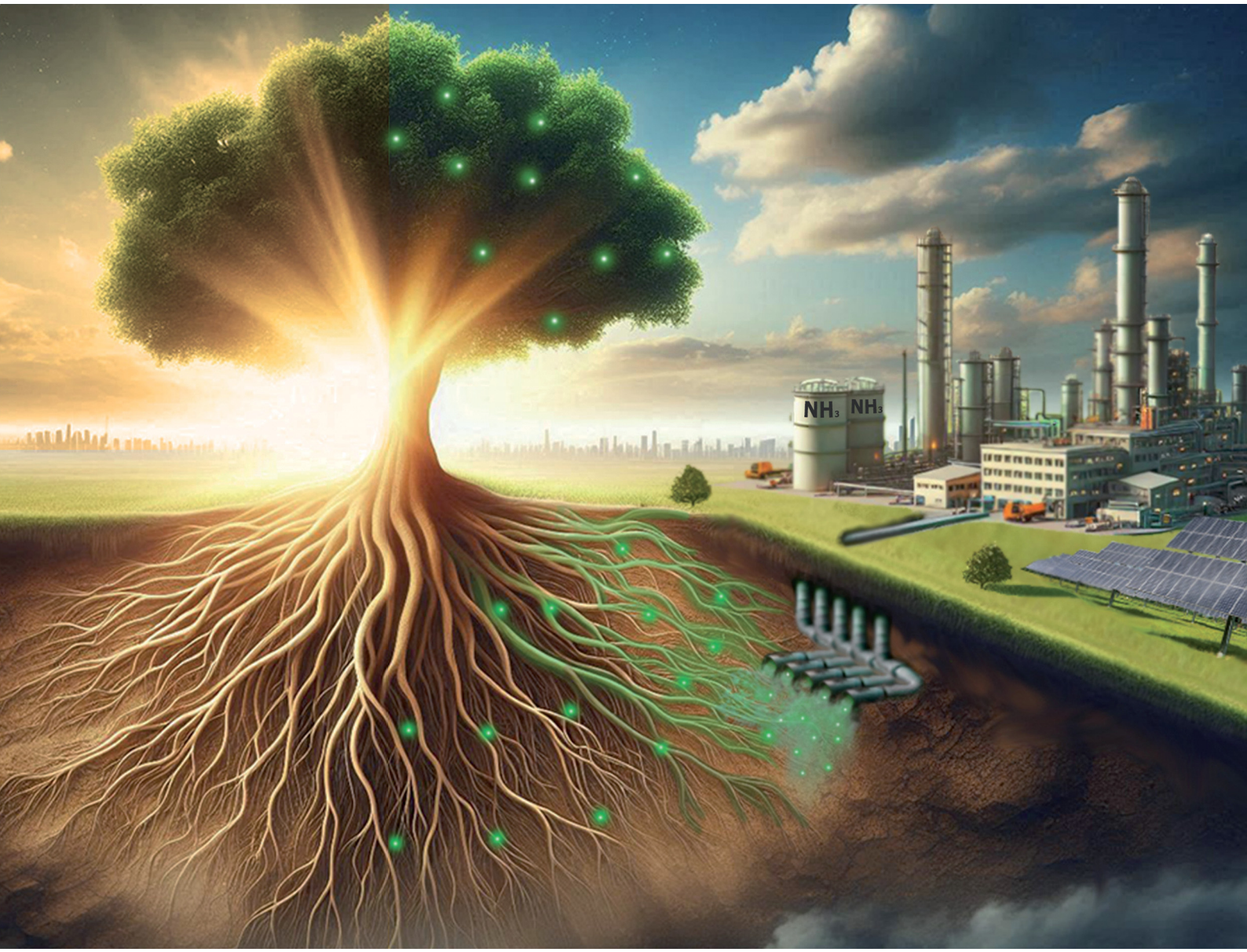

ISSN 0306-0012

ROYAL SOCIETY OF CHEMISTRY

REVIEW ARTICLE

Laura Collado, Víctor A. de la Peña O'Shea *et al.*
Light-driven nitrogen fixation routes for green ammonia production

Chem Soc Rev

REVIEW ARTICLE

View Article Online
View Journal | View Issue

Cite this: *Chem. Soc. Rev.*, 2024, **53**, 11334

Light-driven nitrogen fixation routes for green ammonia production

Laura Collado, * Alejandro H. Pizarro, Mariam Barawi, Miguel García-Tecedor, Marta Liras and Víctor A. de la Peña O'Shea *

The global goal for decarbonization of the energy sector and the chemical industry could become a reality by a massive increase in renewable-based technologies. For this clean energy transition, the versatile green ammonia may play a key role in the future as a fossil-free fertilizer, long-term energy storage medium, chemical feedstock, and clean burning fuel for transportation and decentralized power generation. The high energy-intensive industrial ammonia production has triggered researchers to look for a step change in new synthetic approaches powered by renewable energies. This review provides a comprehensive comparison of light-mediated N_2 fixation technologies for green ammonia production, including photocatalytic, photoelectrocatalytic, PV-electrocatalytic and photothermocatalytic routes. Since these approaches are still at laboratory scale, we examine the most recent developments and discuss the open challenges for future improvements. Last, we offer a technoeconomic comparison of current and emerging ammonia production technologies, highlighting costs, barriers, recommendations, and potential opportunities for the real development of the next generation of green ammonia solutions.

Received 12th February 2024

DOI: 10.1039/d3cs01075a

rsc.li/chem-soc-rev

Photoactivated Processes Unit, IMDEA Energy Institute, Móstoles, Madrid 28935, Spain. E-mail: laura.collado@imdea.org, victor.delapenya@imdea.org

Laura Collado

Laura Collado is a Senior Assistant Researcher at IMDEA Energy in charge of the photo(thermo)catalytic research line at the Photoactivated Processes Unit. She received her PhD in Chemical and Environmental Engineering from Rey Juan Carlos University in 2015, working on solar fuels production by artificial photosynthesis. She performed a PhD stay at Imperial College London (UK) to develop charge dynamics studies. In 2016, she joined Heriot-Watt University (UK) as a postdoctoral researcher. She obtained a GotEnergyTalent Marie-Skłodowska-Curie-cofund (2018) and a Juan de la Cierva-Incorporación 2020 fellowships. Shortly after, she obtained a JIN-type R + D + i project (Principal Investigator) at IMDEA Energy. Her scientific background covers light-driven catalytic processes, synthesis of multifunctional catalysts, advanced characterization and mechanistic studies.

Alejandro H. Pizarro

Alejandro Herrero is a postdoctoral researcher at the Photoactivated Process Unit at IMDEA Energy. He received his PhD in Chemical Engineering from Universidad Autónoma de Madrid (UAM) in 2013, working on the catalytic hydrotreatment of chlorinated and nitrogenated compounds in water. In 2014 he moved to Abengoa Research S.L. (Sevilla) for more than two years as a postdoctoral researcher, working on drinking water treatments for the removal of nitrate and disinfection by-products. He also worked on nitrate removal at Université du Poitiers in 2012 and at the UAM in 2017–2018. Since 2022, he was focused on photo(thermo)catalytic production of hydrogen and ammonia at IMDEA Energy.

1. Introduction

1.1. Ammonia: the key to a greener future

A transformative solution to the ever-growing energy crisis and global warming is to replace the current fossil feedstock with renewable and carbon-free energy sources. A fundamental pillar of this energy transition relies on the development of affordable, safe and sustainable technologies to store and transport renewables, which would contribute to alleviate the fossil fuels dependency and balance the mismatch between renewable energy supply and demand at the power grid. Storing cheap renewable electricity into chemical bonds (*i.e.* chemical energy storage) opens the door to a long-term energy storage, which would drive the transition towards carbon-free fuels and commodity chemicals.[1,2] Among renewables, solar energy is by far the largest exploitable energy resource on earth (4.3×10^{20} J h^{-1}).[3,4] In fact, the total sum of recoverable energy from all renewable and non-renewable reserves only covers 1% of the solar energy arriving to the earth (173 000 TW h per hour[5]), which is almost 10 000 times higher than the global primary energy consumption of the world (178 899 TW h $year^{-1}$ in 2022).[6] However, the challenge lies in the development of sustainable and cheap technologies able to harvest and storage solar energy as high-energy fuels and high-value chemicals,

Mariam Barawi

Mariam Barawi is a Senior Assistant researcher in charge of the (photo)electrochemical cells line in Photoactivated Process Unit. She obtained her PhD in 2015 at Universidad Autónoma de Madrid, investigating photo-electrochemical solar energy conversion. Thereafter she started her postdoctoral period at Istituto Italiano di Tecnologia investigating nanocrystals for Smart Windows. In 2017, she joined IMDEA Energy and has been awarded the three more prestigious Spanish Science Ministry grants (Juan de la Cierva-Formación 2017, Juan de la Cierva-Incorporación 2020 and Ramon Y Cajal 2023). Mariam is co-author of more than 50 scientific publications (>2500 citations) and has participated in more than 20 research projects, being Principal Investigator in three of them.

Miguel García-Tecedor

Miguel García Tecedor (PhD in Physics 2017, Universidad Complutense de Madrid) is a Senior Assistant Researcher at IMDEA Energy. His PhD focused on the growth and characterization of semiconducting nanostructures and their application in optoelectronics and energy. In 2015, he joined the Institute for Energy Technology (Norway) to work on organic–inorganic composites for silicon solar cells' passivation. In 2017, he joined the Institute of Advanced Materials at Universitat Jaume I as Research Scientist to investigate (photo)electrocatalytic water splitting and CO_2 reduction. In 2021, Miguel joined IMDEA Energy to work on photo(electro)catalytic approaches towards wastewater oxidation, CO_2 reduction and N_2 fixation. Miguel is co-author of 43 scientific publications and he has participated in 14 research projects, being principal investigator in two.

Marta Liras

Marta Liras is a Senior Researcher at the Photoactivated Processes Unit from IMDEA Energy since 2022. She received her PhD in organic chemistry in 2003 from Universidad Complutense de Madrid (UCM) for her work at the Organic Chemistry Institute (IQOG-CSIC) and Science and Technology of Polymers Institute (ICTP-CSIC). In 2008 she joined Marta Liras the J.C. Scaiano research group at the University of Ottawa as a postdoctoral researcher. She was awarded with Juan de la Cierva (2004), JAE-Doc (2013) and Ramon y Cajal (2016) grants. She leads the Specialized Photochemistry Group of Spanish Royal Society of Chemistry GRUFO-RSEQ. Her interests are focused on polymer design for energy applications.

Víctor A. de la Peña O'Shea

Víctor A. de la Peña O'Shea is the head of the Photoactivated Processes Unit at IMDEA Energy in Madrid (Spain) from 2015. He obtained a PhD in Physical-Chemistry from the University Autonoma de Madrid and Catalysis and Petrochemistry Institute (ICP-CSIC). His research interest is focused on different aspects of Energy production and storage technologies covering a wide range of experience on: (1) design and synthesis of multifunctional hybrid materials; (2) advanced in-operando characterization combined with theoretical calculations; and (3) construction of automatized reactors form lab to pilot plant scale, covering wide range of application from heterogeneous catalysis and solar chemistry technologies.

which could be used in a clean and decentralized manner.[2] A strong candidate to pursue the decarbonization of the energy sector is green ammonia (NH_3), which due to its versatility (*i.e.* existence of N and H elements in its structure) could confront two of the most pressing global challenges today: food and energy security in the context of a low-carbon economy.[7] Basically, ammonia is a multipurpose chemical due to its composition. N atoms provide the molecule an agrochemical value, while H atoms (*ca.* 17.6 wt%) enables the cracking of ammonia to hydrogen (H_2), which can be used in many sectors such as transportation, electricity generation and energy storage.[1,8]

In nature, ammonia is produced by a group of diazotrophic microorganisms that transform atmospheric or aqueous N_2 into NH_3 at mild conditions (<40 °C, atmospheric pressure) with a turnover frequency (TOF) of 40–120 min^{-1}.[9,10] This biological N_2 fixation ($N_2 + 6H^+ + 6e^- \rightarrow 2NH_3$) is restricted to especially cyanobacteria (*e.g. Anabaena*, *Azotobacter*) containing a metalloenzyme nitrogenase with a FeMo cofactor, which is able to convert 50–150 kg air per hectare.[11–14] However, the natural synthesis of ammonia is not sufficient to confront the current global demand. In fact, NH_3 is the second most produced chemical worldwide, after sulphuric acid, with approximately 183 Mtons of annual production,[15] and it is one of the largest-volume industrial chemicals in terms of energy use and carbon footprint.[16] Around 80% of the current NH_3 production is used as a key component of mineral fertilizers,[17] while the rest is mostly used as industrial refrigerant and chemical feedstock in the production of polyimides, nitric acid, nylon, pharmaceuticals, dyes, explosive materials, cleaning solutions, *etc.*[18–20]

Industrial NH_3 production is carried out by the traditional thermochemical Haber–Bosch (H–B) process, following the procedure first developed in the beginning of the 20th century. The H–B process requires high-purity (99.99%) H_2 and N_2 gas streams, and uses Fe- or Ru-based catalysts, typically promoted with K_2O, CaO, SiO_2, and Al_2O_3. Besides, it requires high temperature and pressure (*ca.* 350–550 °C, 20–40 MPa) to enable fast kinetics and to shift the reaction equilibrium towards NH_3 yield ($1/2N_2(g) + 3/2H_2(g) \leftrightarrow NH_3$).[16,18,21]

Although the formation of ammonia is exothermic ($\Delta H^\circ_{298K} = -45.9$ kJ mol^{-1}, $\Delta G^\circ_{298K} = -16.4$ kJ mol^{-1}, $K_{eq} = 750$) and favoured under low temperatures, the high chemical inertness of the N_2 molecule requires high temperatures to break the $N\equiv N$ bond at sufficient rates.[16,22] In fact, equilibrium calculations show that more than 99% of ammonia decomposes to N_2 and H_2 at temperatures higher than 400 °C at 0.1 MPa. Therefore, NH_3 production *via* H–B is operated under high pressures (20–40 MPa) to shift the equilibrium to the right (eqn (1)), reaching ~15% N_2 conversion to NH_3 in a single reaction, or ~97% yield when unreacted N_2 and H_2 are recirculated to the reactor.[19,22] About 96% of the supplied hydrogen is derived from fossil fuels, mainly from steam reforming of methane (72%) from natural gas or coal, and from partial oxidation of coal (26%). The remaining 4% is generated from coal or natural gas electrical generation.[18,20] Consequently, H–B is one of the largest energy consumer and greenhouse gas emitter processes. Indeed, it accounts with 3–5% of global annual natural gas consumption and 1–3% of the global electrical energy, resulting in an overall energy usage of more than 30 GJ $t_{NH_3}^{-1}$.[20,23,24] Moreover, the strict operational conditions are responsible for about 1.8% of the global CO_2 emissions per year, which represent 2.16 kg of carbon dioxide equivalent (CO_{2eq}) for each kg of NH_3 produced.[18] These CO_2 emissions are nearly twice intensive as those of crude steel production and four times those of cement industry.[25] Besides, H–B also generates vast amounts of NO_x that need to be removed *via* selective non-catalytic reduction, increasing the costs of operation.[18] It should be noted that this process also requires large-scale NH_3 plants that increase the capital expenditure and introduce geographical limitations for the construction of production facilities.[21] Apart from this, the availability of feedstock and energy supply (*i.e.* low-cost natural gas and abundant coal reserves) limits the locations where ammonia can be produced. To date, China is the largest NH_3 manufacturer (*ca.* 30% of production and 45% of associated CO_2 emissions), followed by United States, European Union, Russia, India and Middle East (*ca.* 8–10% production each). Important energy savings have been achieved over the past 20th century by shifting away from coal gasification to more efficient natural gas-based production, and implementing large centrifugal compressors, better process control and maintenance, better use of waste heat, and catalyst improvements.[26] However, efficiency gains have almost reached the theoretical minimum energy intensity,[25] thus making clear the critical need to develop alternative routes for a renewable, efficient and affordable ammonia synthesis. Over the last few years, intensive research activity is currently devoted to achieve the decarbonization of ammonia synthesis, preferably under similar mild conditions as the biological process. In 1921, renewable ammonia started to be produced from hydropower, but only one commercial plant is still operational to date.[27] At present, the annual production of renewable ammonia (<0.02 Mt) represents 0.01% of the global ammonia production. Various demonstration plants are today under operation, based on solar and wind energy coupled with electrolyzers for H_2 production.[27]

In this context, important research efforts are currently focused on finding efficient and environmental-friendly ammonia production routes, fully powered by renewable energy and operated at mild conditions. The so-called artificial N_2 fixation or nitrogen reduction reaction (NRR) is a promising candidate for the next generation of ammonia production technologies, which is included within the so-called emerging power-to-X (P2X) technologies. In brief, NRR targets the catalytic conversion of natural feedstocks (N_2/air, H_2O) into ammonia under milder conditions than the conventional H–B process, powered by renewable energies.[28,29] When NRR is powered by solar energy, this process can be carried out by different light-driven routes such as photocatalysis, (photo)electrocatalysis, and photothermal catalysis.

A close look to the state-of-the-art literature reveals an increasing publication rate over the past 10 years (including research articles and patents), which has been especially noticeable over

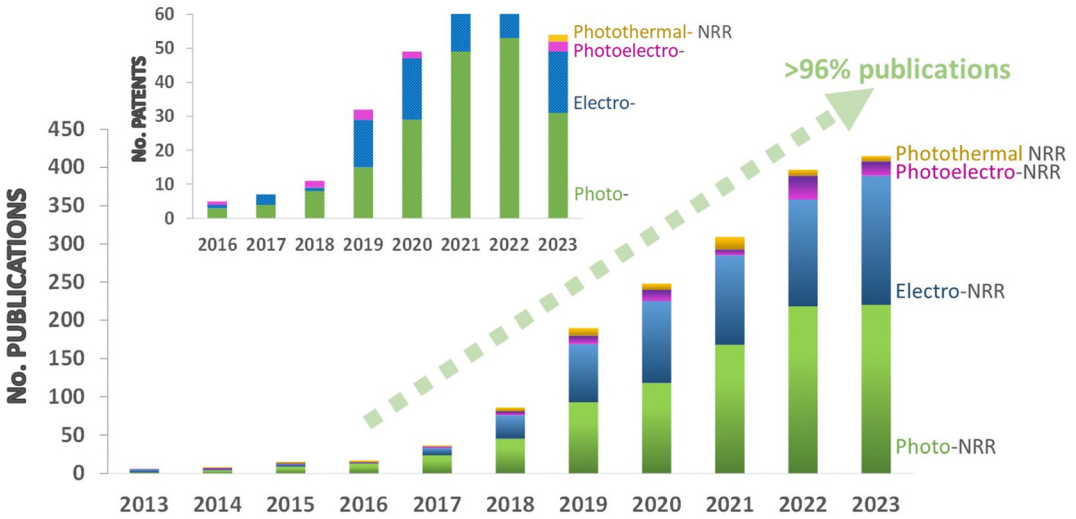

Fig. 1 Histogram showing the increasing trend in the number of publications in the NRR field over the past 10 years. Papers are classified by technologies: photocatalytic-NRR (green), electrocatalytic NRR (blue), photoelectrocatalytic NRR (pink), and photothermocatalytic NRR (yellow). Data collected from the main scientific journal databases (∑entries = 1526 in the period January 2013–December 2023). Inset shows a histogram of the numbers of NRR patents per year and per NRR technology. Data collected from Google Patents (∑patents = 325, 2013–2023).

the last 6 years (Fig. 1). This trend highlights the big potential of NRR technology to contribute to the decarbonization of the energy system and the fertilizers industry, but also other pressing sectors such as transportation or chemical industry. However, the production rates and selectivity of the current catalytic systems still fail to reach industrial interest. Therefore, research efforts still need to be directed on the development of efficient catalysts and cost-effective solutions to take a leap forward in performance for practical applications.

1.2. Scope of this review

Our first goal in this review was to provide a comprehensive comparison of green ammonia production technologies by light-mediated catalytic routes. To do so, here we revise the current status of each technology, highlighting the major advantages and challenges that must to be addressed. Further, and with the aim of progressing on green ammonia technologies, we provide a didactic overview of the fundamentals and key aspects controlling the NRR process, including possible strategies to improve the performance, intuitive guidelines for the development of photoactive materials, and an assessment of experimental methodologies and recommendations for a reliable analysis. Going beyond fundamental research, we also overview the role of ammonia in the future energy scenario, including a technoeconomic comparison of current and emerging NRR technologies for a foreseen practical application, highlighting costs, barriers, opportunities, and recommendations for improvement.

2. Fundamentals and challenges of nitrogen activation

Molecular nitrogen (N_2) is considered the most stable known diatomic molecule in nature. It contains an extremely stable N≡N triple bond and a non-bonding pair of electrons (σ* and π*) on each atom (Fig. 2). The molecular orbital configuration of N_2 leads to a large energy gap (10.82 eV) between the highest occupied and lowest unoccupied molecular orbitals (HOMO and LUMO, respectively), which hinders the electron injection. In particular, the N_2 molecule can be activated by either accepting σ electrons from N_2 *via* empty d-orbitals, or donating electrons from partially occupied d-orbitals to the π* antibonding orbitals of N_2.

This configuration provides the N_2 molecule a very short bond length of 109.8 pm and high bond strength of 941 kJ mol^{-1}.[30–32] However, this high dissociation barrier cannot fully

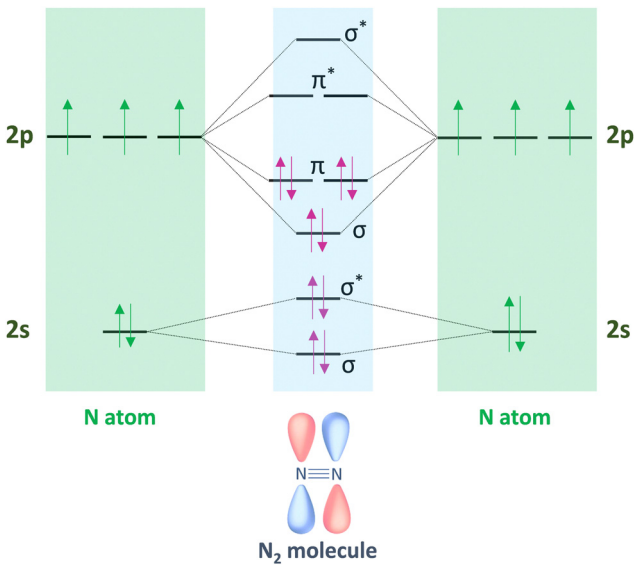

Fig. 2 Hybridization of the s–p atomic orbitals in N_2 molecule by linear combination of N atoms sharing three pairs of electrons from 2σ and π molecular orbitals.

explain the chemical inertness of N_2 if compared to other similarly triple-bonded molecules, such as acetylene (HC≡CH), which has a comparable dissociation energy (*ca.* 962 kJ mol^{-1}) but substantial more reactivity than N_2.[33] The difference arises from the high first-bond cleavage energy of N_2 (410 kJ mol^{-1}) that almost doubles that of acetylene's (222 kJ mol^{-1}), and thus hinders N≡N dissociation.[22,33] Besides, the N_2 molecule lacks a permanent dipole and therefore shows a high ionization potential (15.84 eV), a negative electron affinity (−1.90 eV), and a low proton affinity (493.8 kJ mol^{-1}), which is lower than acetylene's (641.4 kJ mol^{-1}). Besides, its large energy gap (10.82 eV) complicates the electron transfer from the catalyst surface to the N_2 molecule. All these factors strength the chemical inertness of N_2 and its difficulty for the direct protonation under ambient conditions, despite being perfectly accessible from a thermodynamic point of view[31,34,35] (eqn (1)):

$$N_2(g) + 3H_2(g) \rightarrow 2NH_3(g)$$
$$\Delta H(25\,^{\circ}C) = -92.2\ \text{kJ mol}^{-1};\ \Delta G_f^{\circ}(25\,^{\circ}C) = -16.5\ \text{kJ mol}^{-1} \quad (1)$$

N_2 fixation can be achieved in nature *via* nitrogenases under ambient conditions, or artificially *via* catalysis by substituting biological steps by chemical routes. The catalytic nitrogen reduction reaction (NRR) to ammonia is a multistep process involving the consecutive transfer of six electrons and six protons, and multiple intermediate chemical species (M–$N_xH_y^{n+}$). The half-reactions of N_2 reduction, hydrogen evolution reaction (HER), and oxygen evolution reaction (OER), together with their equilibrium potentials,[22,36] are summarized in Fig. 3.

In general, the catalytic NRR to NH_3 requires: (i) chemisorption of N_2 and hydrogen atoms on the catalyst active sites; (ii) activation and cleavage of the N_2 molecule; (iii) reductive addition of hydrogen atoms to form ammonia (NH_3) or ammonium (NH_4^+) depending on the pH media; and (iv) desorption of NH_3/NH_4^+ from the catalyst surface. The equilibrium between gas-phase ammonia [NH_3(g)], dissolved ammonia [NH_3(aq)], and ammonium ion [NH_4^+(aq)] strongly depends on the pH of the reaction media (eqn (2)), mostly existing as NH_4^+ in acidic solutions.[1,37] Under these conditions, protons are highly available and adsorb more easily on the surface of catalysts than N_2 molecules. Consequently, most surface active sites are occupied by hydrogen atoms that consume available electrons to drive the competing HER, and consequently lowering both NRR yield and selectivity.[38]

$$NH_3(g) \overset{H_2O}{\rightleftharpoons} NH_3(aq) \underset{pH>11}{\rightleftharpoons} NH_4^+(aq) + OH^-(aq) \quad (2)$$

The kinetically preferred HER ($2H^+ + 2e^- \rightarrow H_2$) can be hindered by limiting the accessibility of protons and electrons through changes in the NRR conditions; for instance, increasing the reaction pressure, moderately increasing the reaction temperature (preventing an equilibrium shift towards NH_3 decomposition), and decreasing the concentration of the proton donor.[38,39]

Nevertheless, the undesired HER is dominant in most photo(electro)chemical systems, in which electrons and protons preferentially evolves H_2 instead of reducing N_2 to ammonia, which is one of the major bottleneck of the NRR.[22,38] Besides, the low solubility and low diffusion rates of N_2 to active sites impose additional kinetic limitations in aqueous reaction media.[31]

Apart from H_2 evolution, the product distribution of NRR may contain other reduction products such as hydrazine (N_2H_4) and diazene (N_2H_2), which are singly-bonded and doubly-bonded partially hydrogenated molecules, respectively; or ammonia oxidation products such as nitrates (NO_3^-) and nitrites (NO_2^-). We note that diazene has never been

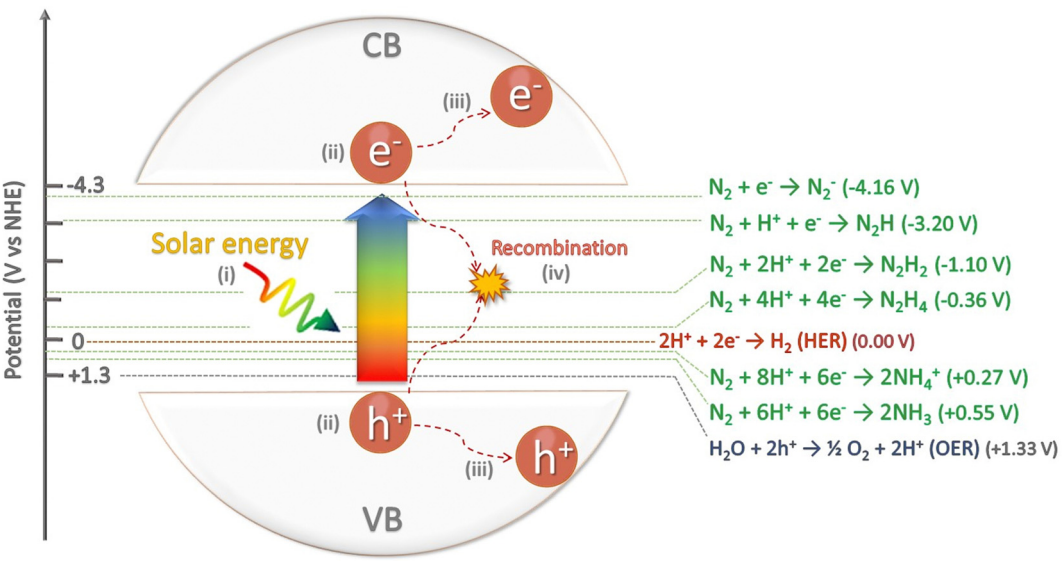

Fig. 3 Schematic energy diagram for NRR, HER and OER, including their corresponding redox potentials (V *vs.* NHE). Additionally, the scheme depicts (i) the absorption of light by the semiconductor, (ii) the subsequent photogeneration of electron/hole pairs, (iii) the migration of the carriers to the surface of the semiconductor, (iv) recombination of carriers.

spectroscopically observed in solution due to either its high reactivity and spontaneous disproportionation to N_2 and H_2 (preferably in acidic media), or its rapid conversion to N_2H_4.[22,40]

2.1. Natural N_2 fixation and global nitrogen cycle

The nitrogen cycle is one of the most critical biogeochemical cycles on Earth. It manages the fifth most abundant element in our solar system, which is also an essential bioelement present in nucleic acids and proteins.[1,41] Unreactive atmospheric N_2 can be fixed in nature mainly *via* (i) lightning strikes, or through (ii) diazotrophic microorganisms containing the enzyme nitrogenase. (i) Lightning strikes dissociate and ionize molecular N_2 and O_2 into free radicals as result of the instantaneous increase of temperature (as high as 30 000 K) and local air pressure. Free radicals combine to generate stable molecules such as nitric oxide (NO), nitrogen dioxide (NO_2), N_2, ozone (O_3) and O_2. Nitrogen oxides may further react with atmospheric water to form nitric acid (HNO_3), which may act as a soil fertilizer on the earth's surface *via* reduction of NO_3^- to NO_2^- and NH_4^+ by humic substances.[42] (ii) The second route consists on the biological N_2 fixation into terrestrial and marine ecosystems by nitrogen fixing microorganisms (bacteria and archaea). The fixed nitrogen is subsequently converted into a diverse range of N-containing compounds (*i.e.* ammonia, amino acids, nucleic acids, amines, N-heterocycles, nitrates, nitrites, *etc.*), and finally returned to the atmosphere as molecular nitrogen through microbial denitrification in soils, and fresh/marine waters.[1,41–43] These compounds are synthesized through nitrogenase enzymes under ambient conditions and without H_2. Nitrogenase (Fig. 4a) is a two-component system

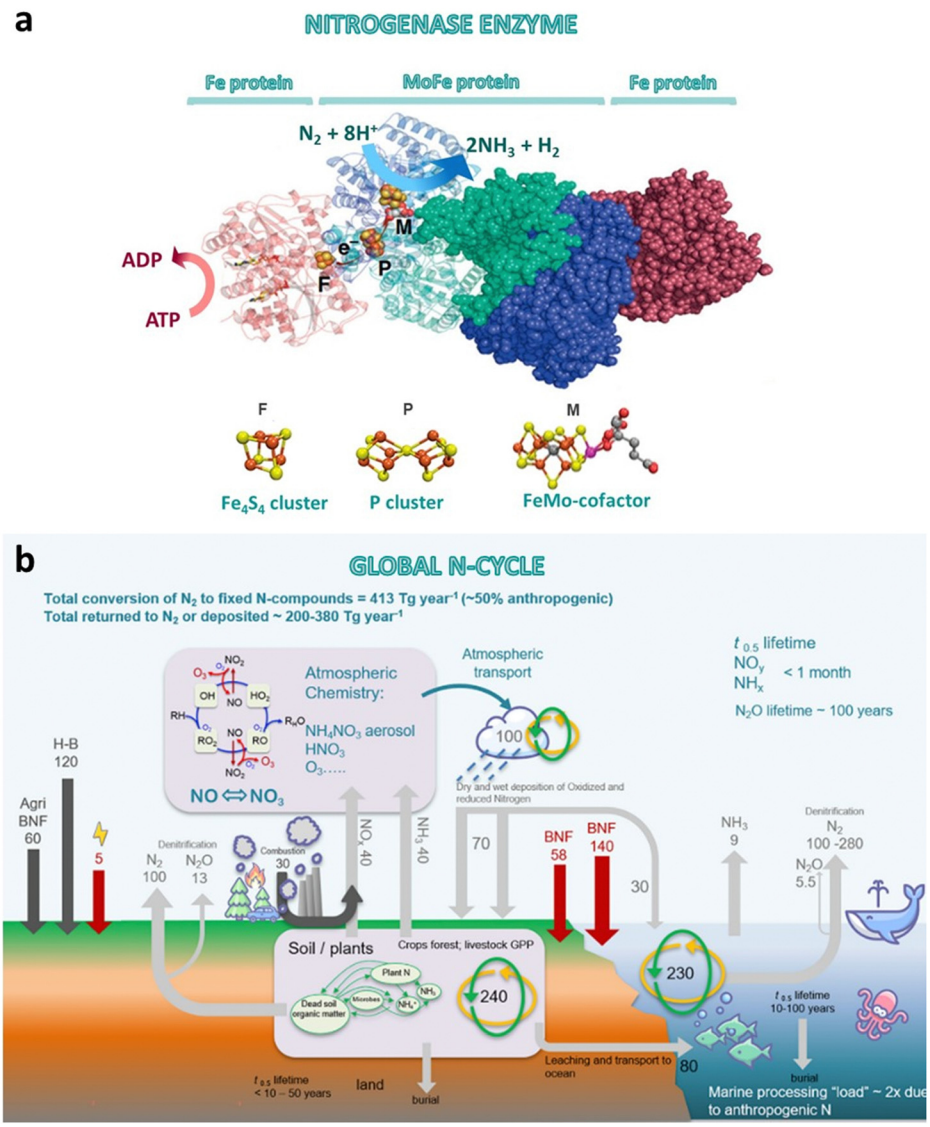

Fig. 4 (a) Structure of the nitrogenase enzyme complex, including the MoFe and Fe protein components with the three metalloclusters (Fe_4S_4 cluster, P cluster and FeMo-cofactor). The Figure also shows the ATP hydrolysis by the Fe protein, the electron transfer to the catalytic site, and the biological nitrogen fixation to ammonia (adapted from ref. 48). (b) Global nitrogen cycle and fluxes in Tg per year (BNF, biological nitrogen fixation; H–B, Haber–Bosch nitrogen fixation; GPP, gross primary productivity). Reproduced with permission from MacFarlane *et al.*[49] Copyright 2020 Elsevier Inc.

composed of two metalloproteins working in tandem: an electron-donating iron protein (Fe_4S_4 cluster) and a catalytic active site metallocofactor (MoFe protein).[12,23,42] In brief, the iron protein (also called dinitrogenase reductase or component II) acts as a strong reducing cluster, hydrolyzing adenosine 5′ triphosphate (ATP) and donating the generated electrons to the MoFe protein (also called dinitrogenase or component I), which finally reduces N_2 into NH_3.[12,23,42,44] The MoFe protein contains two metal clusters (Fig. 4a): (i) the iron–molybdenum cofactor (FeMo-co), which provides the active site for nitrogen binding and subsequent reduction, and (ii) the P-cluster [Fe_8S_7] that transfers the electrons from the Fe protein to FeMo-co.[45] Thus, the FeMo-co is the key element for the N_2 fixation mechanism.[46,47] Three classes of nitrogenase are known, which differ in the heteroatom present in the catalytic active site (Mo, V or Fe). Among them, the Mo-dependent nitrogenase is the best-studied and the most chemoselective one.[22,44,47]

For NRR, two electrons are consumed by the MoFe cofactor to bind N_2 to Mo, together with a displacement of hydrogen following the catalytic cycle shown in Fig. 4b.[23] Then, the structure of nitrogenase limits the access to electrons in order to avoid the competing HER, but the overall NRR entails 8 electron transfer reaction and one H_2 molecule release (eqn (3)). Among nitrogenases, the Mo-dependent one produces two molecules of NH_3 per H_2 (eqn (3)) at a faster rate and more efficiently (requiring less ATP per mol of N_2) than the others, which produce more H_2 than NH_3.[22,44,47,50]

$$N_2 + 8e^- + 16ATP + 8H^+ \rightarrow 2NH_3 + H_2 + 16ADP + 16P_i \quad (3)$$

In general, about 16ATP or 26–30 GJ $t_{NH_3}^{-1}$ are required to fix N_2 into ammonia under ambient conditions. This corresponds to a substantial energy expense of 244 kJ to reduce one N_2 molecule into NH_3, which results in a maximum overall efficiency of the enzyme nitrogenase of *ca.* 10–15% (150–225 GJ $t_{NH_3}^{-1}$).[23,51–53]

On the other hand, N_2 fixation can also occur *via* oxidative pathway with O_2 or H_2O to produce NO_x (x = 1, 2, 3 corresponding to oxidation states of +2, +3 and +5, respectively). NO_x are crucial feedstocks for the fertilizer and pharmaceutical industries, and are mainly produced *via* thermocatalytic ammonia oxidation. Therefore, finding a renewable nitrogen oxidation reaction (NOR) route to produce nitrate (eqn (4)) is also an appealing approach, alternative to the conventional synthesis of nitrate from NH_3 oxidation.[1,54] For practical NRR applications, NOR is thermodynamically more favourable than the competing side oxygen evolution reaction (OER, 1.23 V *vs.* RHE) and therefore, coupling NOR with NRR in a single device is emerging as a disruptive approach for the production of fertilizers directly from N_2 and even from air.[55]

$$N_2(g) + 6H_2O \rightarrow 2NO_3^-(aq) + 12H^+ + 10e^- \quad E^0 = 1.076\ V\ vs.\ RHE \quad (4)$$

Looking globally, the natural N_2 fixation provides 413 Tg y^{-1} (Tg = 10^{12} g) of reactive nitrogen (*i.e.* NH_3, NH_4^+, NO, NO_2, HNO_3, N_2O, *etc.*) to terrestrial and marine ecosystems, of which human activities contribute for half (210 Tg $year^{-1}$).[43,56] The development of intensive agriculture and new high-yielding crops over the past century is largely responsible for this anthropogenic value, which has drastically altered the nitrogen cycle. Indeed, nitrogen fertilizers frequently generate leaching of NO_3^- in drainage waters that end up in seas and open oceans (40–70 Tg $year^{-1}$), increasing the amount of reactive nitrogen to be processed in water systems. Fertilizer leakages also contribute to trace emissions of NH_3, which together with nitrogen oxides (NO_x) emissions from combustion processes, contribute to 100 Tg $year^{-1}$ to the atmosphere. Additional N_2 and N_2O emissions are emitted back to the atmosphere from denitrification in marine sediments. In turn, reactive nitrogen in the atmosphere may generate secondary pollutants, such as ozone and other photochemical oxidants and aerosols, mainly ammonium, nitrates and sulfates.[43] The human intervention in the nitrogen cycle has been key to securing food security, but is also having a negative impact on climate, biodiversity and human health. As a few examples, N_2O is a potent greenhouse gas able to trap heat about 200 times more effectively than the well-known CO_2; over-enriching of reactive nitrogen in aquatic ecosystems can lead to eutrophication and loss of biodiversity; while atmospheric aerosols can cause serious health issues such as respiratory illness, cancer, or cardiac diseases.[57] These effects highlight the importance of finding solutions to remediate the human disruption of the nitrogen cycle, which has been identified as one of the 14 Grand Challenges for Engineering in the 21st century.[57] Most negative effects would be more easily mitigated by cutting reactive nitrogen emissions to the atmosphere, since the lifetime of N-compounds range between a few hours (NH_3 and HNO_3) to few days-week (aerosols); one exception is N_2O with an atmospheric lifetime of approximately 100 years. On the other hand, removal of reactive nitrogen from oceans and terrestrial ecosystems would be slower, needing periods longer than a few decades for the later.[43] Bearing this in mind, possible technological solutions suggested by the National Academy of Engineering[57] include the recycling of organic waste (*e.g.* converting manure into pelletized organic fertilizers), and capturing and valorization of derived-greenhouse gases (CH_4, N_2O) to reduce atmospheric emissions from soils and water systems. Besides, engineering solutions could improve the efficiency of fertilizer application, reducing leaking into water bodies, runoff and erosion.

In this context, finding sustainable routes to produce valuable nitrogen-containing fuels and chemicals (*e.g.* ammonia, nitric acid, hydrazine, *etc.*) is also key to restore the nitrogen cycle and to promote an environmental-friendly nitrogen economy.[1,41] Indeed, the U.S. Department of Energy recently concluded that there is a lack of sustainable ammonia synthesis technologies and catalysts with enough activity, selectivity, and scalability to fulfil industrial requirements.[58] Research is currently in progress to adapt the enzymatic processes underlying the natural nitrogen cycle to artificial N_2 fixation routes, which can produce renewable-sourced ammonia in an efficient and affordable manner as discussed in detail in the following sections.

2.2. Artificial N_2 fixation

As mentioned above, the ultimate goal of artificial N_2 fixation is to mimic the chemistry behind the nitrogenases to photoactive catalytic systems, ultimately looking for a potential scaling-up for industrial application. However, NH_3 yields are still very low to fulfil the industrial demand, mainly due to the inertness of the N_2 molecule, and the easiness of the competitor HER. Therefore, this technology has become an on-going hot research topic for the next generation of sustainable ammonia production. On this basis, this review addresses the main light-driven catalytic routes (*i.e.* photocatalytic, photoelectocatalytic, PV-electrocatalytic and photothermal catalytic NRR) in Section 5. We note that some of these processes have recently diversified into alternative catalytic routes such as magnetic field enhanced photocatalysis,[59] sono-photocatalysis,[60,61] piezo-photocatalysis,[62,63] plasma-catalysis,[64–66] plasma-electrocatalysis,[67–70] plasma photoelectrocatalysis,[71] plasma-UV,[72] mechanocatalysis,[73,74] light-driven chemical looping,[75] and even semi-artificial photosynthesis routes based on (photo)bioelectrocatalysis,[76–78] which are out of the scope of this review.

3. NRR mechanism

As shown in Section 2.1, N_2 fixation to ammonia occurs in nature *via* a multi-proton and electron transfer process, with the hydrolysis of 16 adenosine triphosphate (ATP) molecules per molecule of N_2. From a mechanistic point of view, the NRR process involves four main steps: (i) N_2 adsorption on the catalytic active sites; (ii) N≡N bond cleavage by either proton transfer from a proton donor or by electron injection from an external circuit; (iii) hydrogenation through proton-coupled-electron transfer (PCET) processes; and (iv) formation and desorption of NH_3.[38] The overall hydrogenation of N_2 to ammonia is a 6 electron-proton transfer process, in which the first hydrogenation ($*N_2 + H^+ + e^- \rightarrow *N_2H$) is commonly regarded as the rate-limiting step (where * indicates a surface site).[38] Subsequent protonation to NH_3/NH_4^+ occurs *via* two possible intermediates: hydrazine (N_2H_4) and diazene (N_2H_2),[79] which can be both hydrogenated more easily than N_2 due to their higher proton affinities (853.2 kJ mol^{-1} and 803 kJ mol^{-1} for hydrazine and diazene, respectively, *vs.* 493.8 kJ mol^{-1} for N_2).[22]

The reaction mechanism for heterogeneous NRR can be divided into dissociative or associative, depending on the adsorption and hydrogenation modes of nitrogen on the catalyst surface (Fig. 5). In the dissociative pathway, the triple N≡N bond is first cleaved on the catalyst surface and then, the protons and electrons are added to the adsorbed N atoms to form NH_3.[38,80] However, it is extremely difficult to directly break the N≡N bond due to its high bond strength (941 kJ mol^{-1}). This explains why the industrial Haber–Bosch process, which follows the dissociative pathway, requires harsh reaction conditions.[81] In general, the dissociative pathway is favored over catalytic surfaces with highly negative N_2 adsorption energies, such as over early transition metals (*e.g.* Sc, Y, Ti, Zr).

In the associative pathway, the hydrogenation of N_2 proceed before the N≡N triple bond is broken, leaving one N atom adsorbed on the catalyst surface for further hydrogenation to NH_3. Addition of hydrogen can occur following distal or alternating pathways, depending if the two N atoms are hydrogenated alternatively or if the terminal N atom is hydrogenated preferentially.[38,80] The possible formation of N_2H_4 by-product (alternating) is a key distinction between these two pathways. Further, the alternating pathway can also start with a side-on N_2 adsorption, known as the enzymatic pathway.[81]

Moreover, a special pathway for N_2 reduction is the Mars–van Krevelen (MvK) mechanism, mostly prevalent for metal nitrides.[82–84] In this case, ammonia is produced by the reduction of the surface nitrogen atoms of the catalyst, creating N vacancies that are further replenished by N_2 molecules. Thus, the MvK mechanism is thermodynamically more favorable than the dissociative and associative pathways, because the formation of the first NH_3 molecule does not involve the breaking

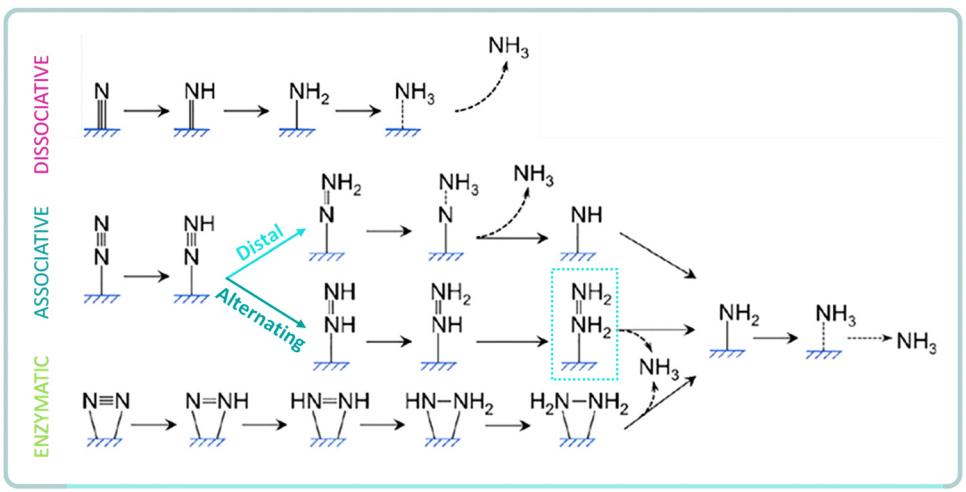

Fig. 5 Schematics of possible pathways for NRR to ammonia on heterogeneous catalysts. Adapted from ref. 32.

down of the triple bond in the N_2 molecule (*i.e.* it is formed from the N site on the nitride surface), which significantly lowers the energy barrier for NH_3 formation.[85,86] However, the catalysts following this MvK mechanism can easily deactivate if the N vacancy is filled with a different atom or if the adsorbed N_2 is not activated.[84]

An additional surface-hydrogenation mechanism was recently suggested by Ling *et al.*[87] for catalysts with weak N_2 binding strength, such as noble-metal catalysts. This approach considers that H^+ reduction is the first step rather than N_2 adsorption, and thus N_2 can be activated and reduced into $*N_2H_2$, and further reduced into NH_3 spontaneously.

Among all mechanistic pathways, biological N_2 fixation is believed to be associative by coordination of N_2 to the metal centre in the FeMo nitrogenase. However, the addition of hydrogen *via* distal or associative pathways is still under investigation.[53] In the case of artificial NRR, the dissociative pathway is highly uncommon for catalysts working at room temperature, which generally follow an associative pathway due to the lower energy input required to break the N≡N bond.[8,38,42,53] However, the NRR mechanism still suffer from uncertainties and this limits the performance enhancement. Relevant insights into the natural N_2 fixation process have revealed the nitrogenase structure and functioning (*i.e.* crystallographic structure of Fe and MoFe proteins), the specific role of the metal clusters (FeMo-co and P-cluster, see Section 2.1), or the existence of different types of nitrogenases.[45] However, structural or fundamental studies have not provided a full picture of the catalytic mechanism under real operating conditions, which is essential to guide a rational design of catalysts for selective NRR. Unclear key factors include the clarification of the specific catalytic sites for activation and reduction steps, the timescale of charge carriers and catalytic events, the changes on the physicochemical and optoelectronic properties of catalysts under illumination and/or heating, and the associated changes on their structure–reactivity. The combination of *in situ* characterization, photophysical measurements and theoretical calculations offers a powerful understanding approach to bridge the gap between mechanistic understanding and catalysis.

3.1. Advanced characterization to understand the NRR mechanism

With appropriate experimental design, *in situ* and *operando* spectroscopic studies can reveal the chemical structure, electronic states of active sites, and reaction intermediates during the catalysis in real time, providing insights into their dynamic evolution. This type of analysis also enables the identification of the deactivation modes of a catalyst. Besides, *in situ* or *operando* characterization can provide a deeper understanding of the catalyst defects, which is a very important feature in photo(thermo)catalysis. In particular, some techniques such as X-ray photoelectron spectroscopy (XPS), electron paramagnetic resonance (EPR) and X-ray absorption spectroscopy (XAS) can discern the type and concentration of defects, allowing real-time monitoring of the status of defects and their evolution during the NRR.[88] In this work, we revise some of the most interesting works that use advanced spectroscopic techniques during reaction to shed some light into the understanding of the light-driven NRR mechanism.

In situ XAS can provide information about the electronic properties and oxidation state changes during the reaction. Hou *et al.*[89] examined the electronic properties of W in a WO_3-based catalyst during the photocatalytic NRR by using *in situ* X-ray absorption near-edge spectroscopy (XANES) and extended X-ray absorption fine structure (EXAFS). The W L3 edge variation of the absorption edge position was found to be almost negligible when the catalyst was only immersed in water under N_2 atmosphere, while it changed to a lower energy under light irradiation, suggesting that W was partially reduced to generate oxygen vacancies during the reaction. Furthermore, the coordination number of the W–O shell in the catalyst decreased from 5.4 to 4.4 during the photocatalytic NRR, which coincided with the variation of the electronic structure of W but also with the formation of NH_3 on the surface of catalysts due to the generation of OVs. This study demonstrates the power of XAS to identify the *in situ* formation of active sites, such as OVs, and to determine their relevance during catalytic reactions for the understanding of the reaction mechanism.

X-ray absorption technique can be performed using hard or soft radiation, depending on the target elements to analyze. When dealing with light elements, it is necessary to move to *in situ* soft X-ray absorption spectroscopy (sXAS). While hard XAS provides bulk information, sXAS allows a penetration depth of around few nanometers in total electron yield (TEY) mode, thus enabling a more accurate tracking of slight variations on the catalyst-reactant interface.[90] In this regard, *in situ* synchrotron radiation soft XAS (*in situ* sXAS) was used to probe the variation of the electronic structure of a model catalyst (*i.e.* Ni single-atom and CeO_2 co-modified reduced graphene oxide), as well as to monitor the photogenerated electron flow during photocatalytic NRR.[91] *In situ* sXAS directly revealed the migration of photoexcited electrons from the light-absorbing unit of CeO_2 to the Ni active sites atoms *via* the electron-transfer bridge of reduced graphene oxide, and then flew toward adsorbed N_2 molecules, providing a direct evidence for the photogenerated electron flow.

Regarding a more surface characterization, some works in literature report quasi-*in situ* XPS analyses, while full *in situ* or *operando* analysis are very scarce. Quasi *in situ* XPS can monitor the formation of defects at the atomic level during the catalytic reaction, as well as to identify their chemical state.[92] For instance, Hou *et al.*[89] tracked the chemical and defect structure of WO_3 during N_2 photofixation by monitoring the O 1s XPS spectra before and after exposing the catalyst to reactants and illumination. Zhang *et al.*[93] proved changes in the chemical state and the electron structure of a $PdCu/TiO_2/Si$ photocathode during the Li-mediated PEC NRR by using *operando* synchrotron XPS. By monitoring the photocathode surface under dark and illumination conditions, they observed the generation and separation of photogenerated electrons and their migration from the nanostructured n^+p-Si optical absorber to the alloyed

PdCu nanoparticles. The resulting electron-rich Pd and Cu sites may serve as a Lewis base, facilitating the adsorption and reduction of Li^+ to Li on the PdCu/TiO_2/Si photocathode surface. A very recent work by Zeng *et al.*[94] reports a true *in situ* XPS analysis to elucidate the NRR mechanism. In particular, they used this technique to analyze the charge transfer between a heterojunction composed by δ-Bi_2O_3 and BWO catalysts. *In situ* XPS revealed that red-shift of the binding energies of W 4f, Bi 4f and O 1s under illumination, compared to the analyses in dark conditions. The shift of binding energies demonstrated that the photogenerated electrons flowed from the conduction band of BWO to the valence band of δ-Bi_2O_3 under illumination, also suggesting a Z-scheme charge transfer pathway within the heterojunction. Another very recent work by Cheng *et al.*[95] also used *in situ* XPS to show the light-induced electron transfer from $ZnIn_2S_4$ to MXene quantum dots during photocatalytic NRR.

Other techniques such as *in situ* EPR spectroscopy allow to analyse the attenuation and generation of defects during N_2 photoreduction. According to the EPR principles, unpaired free electrons in atomic or molecular orbitals will be excited to higher energy levels upon the application of an external magnetic field, thus generating a characteristic signal. For instance, *in situ* EPR experiments under constant N_2 flow recently revealed the role of defects and electron-rich $Cu^{\delta+}$ in promoting the N_2 photoreduction performance of zinc aluminium layered double hydroxide (ZnAl-LDH) nanosheets.[96] The authors found that the 0.5%Cu–ZnAl-LDH sample exhibited a stronger EPR signal, Cu^{2+} (3d9), than the CuZnAl-LDH containing much more copper (as Cu^{2+}). This implied that the generation of oxygen defects increased the number of free electrons in the Cu sites of 0.5%Cu–ZnAl-LDH. Furthermore, the EPR signal intensity of Cu^{2+} for 0.5%Cu–ZnAl-LDH decreased under UV-vis irradiation, demonstrating the transfer of photogenerated electrons to the Cu centers.

In surface chemistry, *operando* infrared spectroscopy can generally identify adsorbed intermediates or products, while *operando* Raman spectroscopy is able to identify other N_2-containing reaction intermediates.[86] Fang *et al.*[97] recently used *in situ* Fourier transform infrared (FTIR) spectroscopy to investigate the photocatalytic N_2 reduction to ammonia in a BiOBr/MXene-Ti_3C_2 composite as catalyst. *In situ* FTIR showed the formation of N_xH_y intermediates by a continuous protonation process of N_2 molecules. Wang *et al.*[98] used *in situ* diffuse reflectance infrared Fourier transform spectroscopy (DRIFTS) to investigate the photocatalytic NRR mechanism over a Fe-doped TiO_2 S-scheme anatase/rutile homojunction. Their experiments revealed the appearance of ammonium and NRR intermediates absorption bands upon illumination, namely $-N_2H$, $-N_2H_2$, –NH, and $-NH_4^+$ centered at 1661, 1585, 1500, and 1319 cm^{-1}, respectively. Besides, they did not find any band associated to the formation of $-N_2H_4$, leading them to conclude that the photocatalytic NRR mechanism followed a distal pathway. In other work, Ajmal *et al.*[99] used *in situ* DRIFT spectra to study the chemical adsorption of N_2 at the surface of an electron-deficient boron-doped carbon nitride catalyst. *In situ* DRIFT and density functional theory (DFT) calculations proved that B–N sites were catalytic active centers for N_2 chemisorption by electron pair acceptance (σ-donation), while the presence of electron-withdrawing boron in the carbon nitride inhibited HER and promoted N_2 adsorption through electron back-donation to N_2.

Surface-enhanced Raman spectroscopy (SERS) can be used to identify key intermediate species for nitrogen fixation at the catalyst-reactant interface, providing mechanistic insights into NRR mechanisms and leading to the design of more efficient catalysts. Nazemi *et al.*[1] used *operando* SERS to identify NRR intermediates at the electrode–electrolyte interface over plasmonic transition metal nanoparticle hybrids. They found that hydrazine is consumed as an intermediate of the NRR, following an overall associative reaction mechanism. We also highlight that the recent advances in microscopic techniques may also enable to image nanoscale defects and their associated changes during NRR. *In situ* scanning electron microscopy (SEM) and transmission electron microscopy (TEM) provide a unique possibility to obtain real-time data on the morphological and microstructural evolution of defective catalyst surfaces at the atomic level,[100,101] as well as atomic disorder and local rearrangement under heating conditions.[102]

4. Strategies to boost NRR

The performance of NRR catalysts is mostly limited by the sluggish activation of the inert N_2, the competing HER, and some technical difficulties associated with the reaction systems. Different strategies are presented below to control the main reaction limitations of the NRR.

4.1. Overcoming the main thermodynamic and kinetic limitations

From a thermodynamic point of view, the activation and reduction of the N_2 molecule is constrained by its short bond length (109.76 pm), the high dissociation energy (941 kJ mol^{-1}) of the N≡N bond, the high ionization potential (15.85 eV) for N_2 adsorption on the catalyst surface, the endothermic first proton addition to N_2 (ΔH^0 = 37.6 kJ mol^{-1}), and its low electron affinity (−1.903 eV).[81] On the kinetics point of view, NRR is mainly impeded by the large energy gap (10.82 eV) between the HOMO and LUMO of N_2 (*i.e.* electron transfer process limitation), the lack of a dipole moment and its low polarizability.[81,82] Besides, finding catalysts with fast NRR kinetics is difficult since their catalytic activity strongly depends on the adsorption energy of the different surface reaction intermediates (Fig. 6a).[103] For instance, transition metals that bind nitrogen too weakly (right-side of the volcano plot, *e.g.* Cu, Ag) are limited by N_2 activation (N_2 adsorption as N_2H^*), whereas strong-binding metals (left-side of the volcano plot, *e.g.* Ru, Mo) are limited by hydrogenation due to a slow N–H formation, either through protonation of NH* to form NH_2* or by removal of NH_2* as NH_3.[103–105] Metals located at the top of the volcano plot (*e.g.* Ru, Fe, CoMo alloy) are expected to be

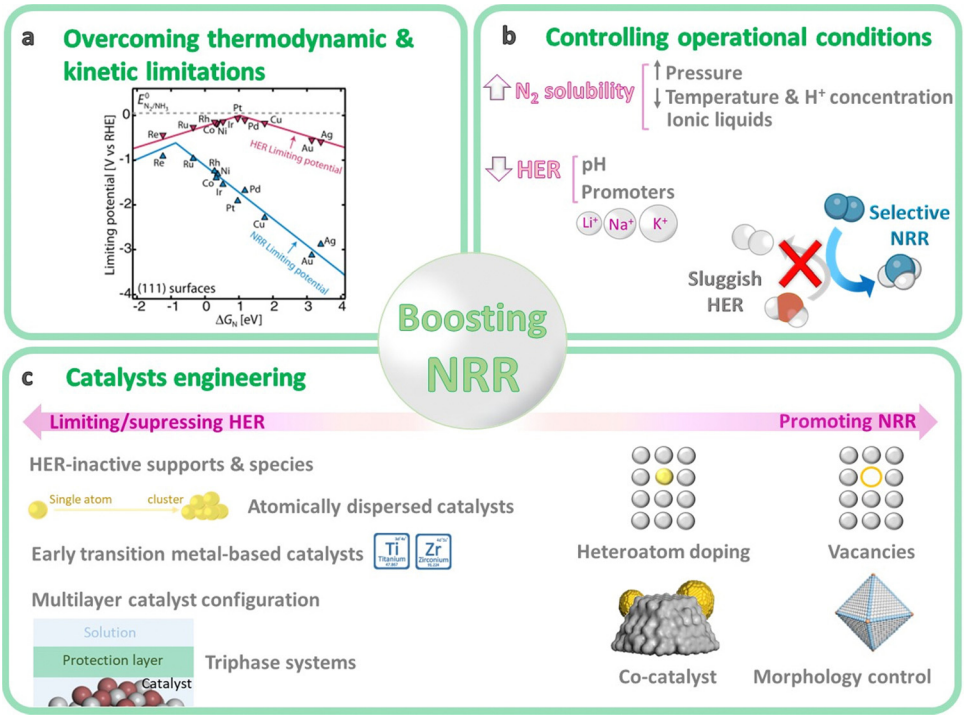

Fig. 6 General overview of the main strategies to boost NRR performance, in terms of reaction engineering (a) and (b) and catalyst engineering (c). Volcano plot in Fig. 6a reprinted from ref. 104 Copyright 2017 The American Association for the Advancement of Science.

highly active for NRR, since they have an intermediate nitrogen binding. However, these metals have a higher adsorption ability towards H atoms and exhibit a significant activation barrier for both N_2 dissociation and N–H bond formation. For that reason, the Haber–Bosch process is conducted at high temperature to reach acceptable reaction rates.[104,105] Unfortunately, no metal exists with an intermediate N* binding and a low N_2 dissociation energy (bottom middle of volcano plot).[105] Therefore, active site engineering is key to lower the activation barriers and achieve a preferential adsorption of nitrogen rather than hydrogen. Widely studied strategies include heteroatom doping, vacancies construction, co-catalyst loading, morphology control, *etc.* (more details in Section 4.4).

4.2. Limiting the competing hydrogen evolution reaction (HER)

The competitor hydrogen evolution reaction (HER, $2H^+ + 2e^- \rightarrow H_2$) is a two-electron transfer reaction with one catalytic intermediate (H*, where * indicates a surface site), in which the overall reaction rate is limited by the adsorption of hydrogen (Volmer step), its binding strength to the catalyst surface, and the final desorption of the H_2 molecule (Heyrovsky–Tafel steps) (eqn (5)–(7)).[104]

$$\text{Volmer step: } H^+ + e^- + * \rightarrow H^* \quad (5)$$

$$\text{Heyrovsky step: } H^* + H^+ + e^- \rightarrow H_2 + * \quad (6)$$

$$\text{Tafel step: } 2H^* \rightarrow H_2 + 2* \quad (7)$$

Thus, both NRR and HER involve proton-coupled electron transfer (PCET) reactions. The difference between them is that the HER is dependent on the electron–proton concentration in the reaction medium (*i.e.* first-order kinetics: HER α $[H^+]^1$ $[e^-]^1$), while NRR is independent (HER α $[H^+]^0$ $[e^-]^0$).[38,82,106] Thus, an effective strategy to improve the selectivity to NH_3 consists on limiting the accessibility of protons and electrons to the catalyst surface. On the one hand, restricting the accessibility of protons is important because H atoms adsorb more easily than nitrogen.[107] This can be achieved by either modifying the operational conditions (*e.g.* pH and reaction media, details in Section 4.3), or designing specific catalyst configurations (details in Section 4.4.3). On the other hand, limiting the electron accessibility during NRR can help to control HER, and this can be also achieved through catalyst engineering (details in Section 4.4.3).

4.3. Tuning the operational conditions

The rational control of the operational conditions during NRR is crucial to promote N_2 activation and limit the competing HER (Fig. 6b). The poor solubility of N_2 in the aqueous medium (about 2 vol%) is one of the most crucial factors responsible for the low NH_3 production rates. The low solubility of N_2 implies mass transfer limitations. Lowering the reaction temperature (room temperature and slightly below) can enhance N_2 solubility, and boost NRR selectivity due to the inhibition of the H_2 production at some extent, which is favored at higher temperatures (>40 °C).[38] However, low temperatures also restrict N_2 diffusion, which could be overcome by increasing the reaction pressure. Increasing the operating pressure helps to shift the chemical equilibrium towards NRR, by suppressing HER that is predominant under ambient pressure conditions. However,

higher pressures may also add technological complexity and cost.[38,88] Moreover, N_2 solubility can be improved by increasing the N_2 flow rate, or using gas-diffusion electrodes (GDEs) in (photo)electrochemical flow cell reactors to increase the local N_2 concentration. Further, another efficient strategy to improve N_2 solubility is the use of aprotic ionic liquids to solvate N_2 gas in the reaction solution.[82] This approach can solubilize 20 times more N_2 than aqueous solutions, and limits the proton reduction side reactions due to the lower water content.[10] This growing research field has shown interesting improvements, some related to a better interaction of N_2 with the polar part of the ionic liquids (*e.g.* 1-butyl-3-methylimidazolium tetrafluoroborate, [bmim][BF_4];[108] 1-alkyl-3-methylimidazolium ($C_n$mim, n = 2,4,6) tris(pentafluoroethyl)-trifluorophosphate, [eFAP][109]), or a better solvation of N_2 in the presence of highly fluorinated anions.[110]

On the other hand, changes on the reaction media may shift the chemical equilibrium towards NRR, suppressing the competing HER. For instance, controlling the pH medium is a simple way to limit the concentration of protons available for the NRR process. For aqueous solutions (the most common medium for ambient NRR), the pH determines whether H_2O (basic medium) or H_3O^+ (acidic medium) are the proton donors during NRR (Fig. 7). Neutral solutions or electrolytes (*e.g.* phosphate-buffered saline, PBS), with intrinsically limited proton availability, are the most suitable reaction media for NRR.[82] Under this conditions, H_2 generation is constrained because of a restricted Volmer step (Fig. 7). This involves a first high energy barrier for water dissociation, which does not exist in acidic medium,[38] thus retarding HER and favoring NRR.

Another effective change for decreasing the availability of protons consists on adding alkali metal cations (*e.g.* Li^+, Na^+, K^+) to the reaction medium. These ions tend to form solvation shells and hence steric effects, which remarkably restrict the transfer rate of H_2O molecules to the catalyst surface, thus suppressing HER. In general, the smaller the cation, the easier is the formation of the dehydrated cation layer on the surface of the catalyst.[38,82] Thus, the smallest Li^+ ions are preferred for non-aqueous electrolytes, although commercial Li salts need to be pre-treated to remove NO_x impurities (see Section 6.3). However, high concentrations (>1.0 mol L^{-1}) of bigger cations such as K^+ prevent HER side reactions, and may facilitate the adsorption and activation of N_2 by creating electronic and electric-field effects that polarize nitrogen molecules.[10,111]

4.4. Rational catalysts engineering

Previous sections reflect that the challenging NRR usually impose several limitations to the conventional catalysts, such as high energy barriers for N_2 adsorption and activation, slow electron transfer kinetics to N_2, and unwanted side reactions (hydrogen evolution, ammonia oxidation, nitrogen oxidation). From the viewpoint of material design, an efficient light-driven NRR catalyst should possess suitable surface properties and composition to facilitate the strong binding with N-adatoms rather than H-adatoms, well-defined nanostructure (*e.g.* nanoparticles), high density of active sites (*i.e.* high surface area and porosity), suitable band alignment, high conductivity to facilitate electron transfer, and long durability.[112]

Regarding composition, catalytic active sites need to have strong interactions with the N_2 molecule to achieve an effective photochemical activation. Transition metals (*e.g.* Fe, Mo, V, Ti, Al) can weaken or break the strong triple N≡N bond by donating electrons from their atomic d orbitals into the antibonding π* orbitals of N_2. In contrast, main-group elements (*e.g.* B, C, Bi, S) lack accessible d orbitals but have abundant valence electrons, so they activate N_2 by p-electron backdonation into the unoccupied antibonding orbitals of N_2.[32,81,113] Besides, some main group non-metals, such as C, B, P, S and F can construct abundant defect sites for N_2 adsorption, either through heteroatom doping or vacancy engineering.[81]

This section summarizes the main catalyst engineering strategies to boost NRR performance, which are mainly based on structure modulation and interface engineering (Fig. 6c). These strategies can improve the adsorption and activation of N_2 on the catalytic active sites, tailor the band structure of the semiconductors, and enhance the charge transfer processes. Widely studied approaches include morphology control (plane/corner/edge sites, pores, *etc.*), crystal regulation (amorphous

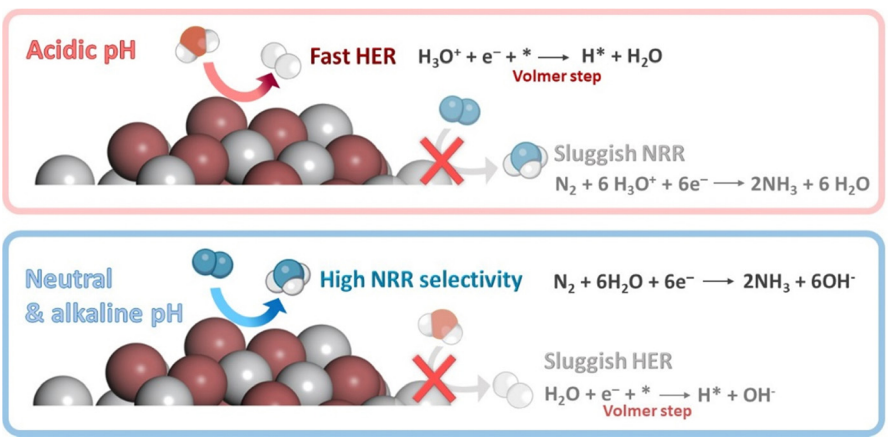

Fig. 7 Effect on pH on the competition between the HER and NRR under ambient conditions.

layers, lattice strain, *etc.*), heteroatom doping, vacancies construction (oxygen, nitrogen and metal vacancies), co-catalyst loading, *etc.* In addition, other engineering strategies focus on restricting or even suppressing the HER activity, mainly using inactive HER supports, early transition metals with stronger nitrogen binding ability, atomically dispersed catalysts or multilevel configurations (Fig. 6c and Fig. 8).

4.4.1. Surface engineering. Intrinsic defects, metal dopants, single sites and co-catalysts have been proposed to be active sites for N_2 chemisorption and activation. Surface engineering helps to create these sites by generating more exposed active centers, modifying the energy-band structure of the semiconductors, enhancing conductivity, promoting ion diffusion, and improving the electron–hole separation, which ultimately impact on a better catalytic performance.[114,115]

4.4.1.1. Vacancy engineering. Defect-rich materials (with anion/cation vacancies) generally exhibit remarkably higher NRR performance than their pristine counterparts, due to the introduction of new active sites, the modulation of their energy-band structure, and the associated improvement of surface reaction kinetics.[31]

Anion vacancies (oxygen, nitrogen and sulfur) can serve as electron traps, promoting the separation of photogenerated carriers in the parent semiconductor, and lowering the reaction barriers through the generation of electron-rich Lewis-base sites for N_2 activation.[31,116] Among them, oxygen vacancies (OVs) are the most popular anion defects in transition-metal oxides due to their low formation energy.[116] They can be easily synthesized by different methods, including thermal annealing, heterogeneous ion doping, wet chemical reduction, and high-energy particle (such as electrons or Ar^+ ions) bombardment.[81] Among advantages, OVs expose extra coordinatively unsaturated sites for the adsorption of the inert N_2 molecule, and these sites increase in concentration as the thickness of photo(electro)catalysts approaches atomic scales (*i.e.* $\approx$1 nm).[117] Besides, OVs facilitate the activation of N$\equiv$N bond by promoting the electron-donating ability of adjacent metal atoms to the π^* antibonding orbitals of N_2 molecule.[81] Besides, OVs may narrow the band gap by up-lifting the valence band maximum and conduction band minimum.[118] This effect results in an extended visible light absorption range, and better separation of photogenerated charges.[116,119] However, high amounts of OVs can excessively distort the crystal structure of the metal oxides, causing electronic delocalization and creating recombination centers of the photogenerated electron–hole pairs.[119,120]

For instance, Hirakawa *et al.*[121] reported the creation of a large number of surface oxygen vacancies in a commercial rutile TiO_2 sample (JRC-TIO-6), in which surface Ti^{3+} species efficiently produced NH_3 from N_2 and water under ambient conditions with a solar-to-chemical conversion (SCC) efficiency 0.02%. Zhao *et al.*[117] demonstrated that ultrathin CuCr-layered double hydroxides (LDHs) nanosheets containing abundant OVs were able to reduce N_2 at wavelengths up to 500 nm. The incorporation of Cu(II) ions introduced structural distortions and compressive strain, creating a high concentration of OVs that improved N_2 adsorption and photoinduced charge transport in the nanosheets. As result, CuCr-LDH achieved a NH_3 evolution rate of $\approx$7.1 μmol L^{-1} under monochromatic illumination at 500 nm (quantum yield (QY) $\approx$0.10%). However, the concentration of defects could not be fully controlled because it was dependent to the morphology control (*i.e.* minimum LDH thickness synthetically achievable of 2.4 nm). Later on, Zhao *et al.*[122] were able to control the concentration of OVs in ultrathin TiO_2 nanosheets by doping with copper ions. The introduction of Cu as a dopant (6 mol% Cu) in TiO_2 introduced substantial compressive strain and created additional OVs, which extended the photoresponse up to 700 nm wavelength. Ammonia evolution rates of 78.9 μmol h^{-1} g^{-1} were achieved under solar irradiation, while full visible light illumination led to NH_3 production rates of 1.54 μmol h^{-1} g^{-1} (600 nm) and 0.72 μmol h^{-1} g^{-1} (700 nm), with corresponding QY of 0.08% and 0.05%, respectively.

The beneficial effect of strain-induced OV defects was recently demonstrated by Li *et al.*[123] from distortion-corrected elemental electron energy loss spectroscopy (EELS) mapping images and spectra, and DFT calculations. These authors constructed a semiconductor/plasmonic heterostructure composed by cerium oxide nanosheets with abundant strain-OV defects, on which they anchored Au hollow nanomushrooms. They found a large formation of Ce^{3+} and OVs at the interface, induced by interfacial strain, which promoted the activation of N$\equiv$N bonds and facilitated the adsorption/desorption of N intermediates. Besides, they found that the hot electrons generated by plasmonic Au were efficiently transferred into the cerium oxide through the heterostructure interface, which also inhibited their reverse movement by the Schottky barrier, thus facilitating an efficient electron–hole separation. As result, the cerium oxide/Au heterostructure photocatalyst delivered a NH_3 production rate

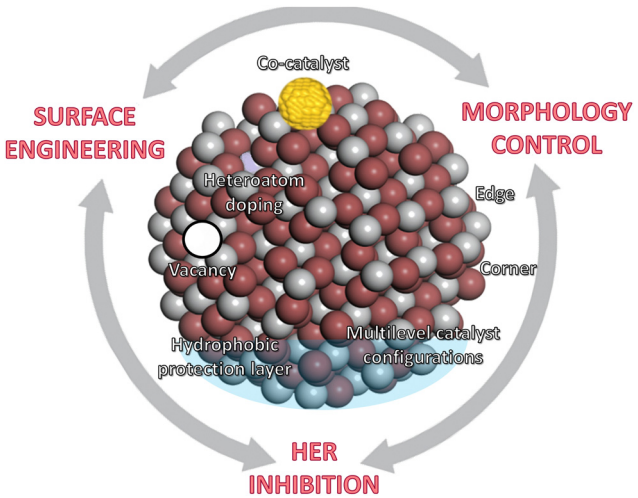

Fig. 8 Catalyst engineering strategies to boost NRR performance, mainly based on surface modification and functionalization, morphology control, and synthetic strategies for suppressing HER.

of 215.14 μmol h^{-1} g^{-1} and a solar-to-chemical conversion (SCC) efficiency of 0.1% under simulated AM 1.5G solar illumination.

Yang *et al.*[124] reported a photocatalytic system based on Au nanocrystals anchored on ultrathin TiO_2 nanosheets with oxygen vacancies. Here, OVs act as active sites for N_2 chemisorption and activation, while N_2 is reduced to NH_3 by the hot electrons generated from plasmon excitation of Au nanocrystals. Au/TiO_2-OV (1.5 wt% Au) reached a NH_3 yield of 130.5 μmol h^{-1} g^{-1} with an apparent quantum efficiency (AQE) of 0.82% at 550 nm. Sun *et al.*[125] presented a non-noble-metal photocatalyst based on sulfur vacancy-rich oxygen-doped 1T-MoS_2 nanosheets. The authors associated the high content of sulfur vacancies with a better N_2 adsorption and activation, enhanced light absorption, and better charge separation and transfer, which led to an excellent photocatalytic performance of 8220.83 μmol L^{-1} h^{-1} g^{-1} (AQE = 4.4%) under simulated solar light illumination.

Nitrogen vacancies (NVs) may also facilitate N_2 adsorption and activation, since they provide an electron-deficient environment due to their similar structure and size with N atoms in the N_2 molecule. Besides, they are an ideal active site for NRR owing to their relatively weak HER activity.[81] Nevertheless, we note that NVs have found to be unstable for electrochemical NRR, leading to deactivation or false-positive results.[81] For instance, Guo *et al.*[126] embedded plasmonic Au nanoparticles in the mesopores of nitrogen-deficient hollow carbon nitride spheres. The NVs served as N_2 chemisorption and activation sites, while the interfacial plasmon-induced charge separation led to a visible-light driven ammonia production of 783.4 μmol h^{-1} g^{-1}, with an apparent quantum yield of 0.64% (at 550 nm) and a solar-to-ammonia (STA) conversion efficiency of 0.032% in pure water and under simulated AM1.5 G sunlight. Liang *et al.*[127] also explored the creation of nitrogen vacancies in a boron-doped graphitic carbon nitride, finding that nitrogen defects improved N_2 adsorption, visible light absorption, and charge carrier separation efficiency. Their optimized catalyst achieved a NH_3 conversion rate of 435.28 μmol h^{-1} g^{-1} under visible light illumination.

On the other hand, the construction of cation vacancies is a less explored field for NRR, and most examples include electrocatalysts. However, this is also an interesting approach for light-driven NRR applications. The introduction of these local charge defects in transition metal oxides can change their surface electronic structure, create new active sites, and improve the charge transfer processes. The typical preparation methods of cation vacancies include chemical synthesis, plasma/chemical etching, thermal annealing in a reducing atmosphere, ion irradiation, heterovalent doping, and stripping.[115] Ding *et al.*[128] investigated the effect of titanium vacancies (V_{Ti}) on the photocatalytic NRR performance of an undoped anatase TiO_2, which was changed from n-type to p-type with V_{Ti}. They found that cation vacancies lead to local charge defects that enhance carrier separation and transport, while trapped electrons can activate and reduce N_2 to NH_3. This material achieved a N_2 fixation performance in air, water and UV-visible illumination of 47.13 μmol h^{-1} g^{-1}, which increased to 64.82 μmol h^{-1} g^{-1} under N_2 atmosphere.

4.4.1.2 Heteroatom doping. Heteroatom doping is an effective approach to improve N_2 activation and hydrogenation, as result of the modification of the chemical composition of the catalysts, their electrical properties, and the creation of structural distortions that increase the concentration of OVs.[31,129] Specifically, electron-deficient dopants induce defect levels that may promote conductivity, provide coordination active sites and even suppress HER by limiting proton adsorption (Lewis acid H^+).[129] Zhang *et al.*[130] reported a photocatalytic NH_3 yield of 195.5 μmol h^{-1} g^{-1} (STA of 0.028%), from pure water and AM 1.5G light irradiation, using Mo-doped $W_{18}O_{49}$ (1 mol% Mo) ultrathin nanowires. This study reveals that the defect states created upon Mo doping polarize the chemisorbed N_2 molecules, facilitating the dissociation of the $N\equiv N$ bond through proton coupling; and elevate the defect-band center toward the Fermi level increasing the driving force towards NRR. Li *et al.*[131] studied the beneficial effect of a non-metal dopant (boron) on the photocatalytic NRR performance of the carbon nitride g-C_3N_5. The doped B-C_3N_5 showed a NH_3 production rate of 421.18 μmol h^{-1} g^{-1}, which was 1.72 times as high as that of g-C_3N_5. The authors inferred that B sites (B–O–H), acting as Lewis acid, played an excellent role in adsorption and protonation of nitrogen, while O–H sites act as Brønsted acid and would protonate the activated nitrogen. Xie and co-workers[132] explored the photocatalytic NRR performance of a single Cu atom-modified carbon nitride, achieving 186 μmol h^{-1} g^{-1} under visible illumination and in the presence of ethanol as electron scavenger, with a quantum efficiency (1.01%) at 420 nm monochromatic light.

On the other hand, NRR performance can be improved with electron-rich dopants (*e.g.* Fe, Mn, Ni, Co). Bo *et al.*[133] reported a 5.3-times higher NH_3 production of Fe-doped TiO_2 nanofibers than pristine TiO_2 (12.1 *vs.* 64.2 μmol h^{-1} g^{-1}, respectively). Besides, they combined *in situ* characterizations with first-principles simulations to demonstrate that Fe dopants modulate the electronic structure nearby oxygen vacancies, facilitating the adsorption and polarization of N_2, and even altering the hydrogenation of N_2 from the associative alternating pathway to a more favorable associative distal pathway. Li *et al.*[134] also demonstrated that doping with metal ions with exposed d orbitals, such as Fe^{3+}, promotes the generation of OVs that are found to be the main active centers for photocatalytic NRR. The authors created OVs in Fe-doped Bi_2MoO_6 by alcohothermal synthesis, showing that metal–alcohol (*e.g.* Fe^{3+}–ethylene glycol) coordination promotes the reduction of Bi^{3+} to Bi^0 to generate OVs, which in turn promotes charge separation and photocatalytic activity. They obtained a 16-fold enhancement of photoactivity, compared to bulk Bi_2MoO_6, with an external quantum yield (EQY) of 2.8% at 420 nm. Regarding Bi-based semiconductors, Yang *et al.*[135] demonstrated the regulation of the electronic structure of Bi_2MoO_6 by Co doping, which led to the creation of dual active sites (*i.e.* Bi and Co sites) that

achieved 7.2 higher NH_3 production (95.5 μmol h^{-1} g^{-1}) than bare Bi_2MoO_6.

4.4.1.3 Co-catalysts. Surface functionalization of semiconductors with co-catalysts, such as noble metal or non-metal nanoparticles, is another strategy to boost NRR. In particular, co-catalysts can be used to trap and separate the photogenerated charge carriers, act as active sites for the adsorption and activation of the N_2 molecule, and decrease the NRR overpotential.[136]

Regarding noble metal co-catalysts, Ranjit *et al.*[137] concluded that the photocatalytic NH_3 yield was highly dependent on the nature of noble metals (Ru, Rh, Pt, Pd) deposited on TiO_2. In particular, they found higher productions and selectivity to NH_3 by successively increasing the metal–hydrogen bond strength (Ru > Rh > Pd > Pt), due to the stabilization of H adatoms (H*) that effectively suppress HER. Qiu *et al.*[138] anchored plasmonic Au nanocrystals on Mo doped $W_{18}O_{49}$ nanowires, reaching a photocatalytic NH_3 production rate of 399.24 μmol h^{-1} g^{-1} and a AQE of 0.611% at 540 nm. The synergistic effect created between Mo doping and Au nanocrystals not only extended the visible light absorption range, but also decreased the desorption energy of NH_3, which accelerated the regeneration of the active sites and further improved NRR.

Bu *et al.*[111] studied the combined effect of plasmonic sensitization and the addition of alkali metal cations (Li^+, Na^+, and K^+) on the overall improvement of the photocatalytic NRR. Plasmonic Au/P25 achieved a NH_3 yield and selectivity of 85 μmol h^{-1} g^{-1} and 75% under UV-visible illumination, which increased to 0.43 mmol h^{-1} g^{-1} and 94.5% (AQE of 0.62% at 550 nm) when promoted by K^+. The authors concluded that the addition of the alkali promoter chemically facilitated the activation and reduction of N_2, while the attachment of Au nanocrystals sensitized the photocatalyst with hot electrons to improve nitrogen fixation.

Liu *et al.*[139] studied different transition metal (Cu, Fe Ni) modified TiO_2 nanosheets founding a better NRR performance and stability than pristine TiO_2. Under the simulated sunlight illumination, the catalyst Cu/TiO_2-1.0% reached a NH_4^+ generation rate of 6.78 mmol h^{-1} g^{-1} using glycerol as the sacrificial agent, which was 6-times higher than that of TiO_2. This better performance was ascribed to the enlarged specific surface area and visible absorption range, as well as to a lower radiative recombination and more efficient charge transfer after loading copper. Ray *et al.*[140] reported a robust nickel phosphide (NixPy) co-catalyst coupled to ZnO nanorods, which achieved a NH_4^+ production rate of 2304 μmol h^{-1} g^{-1} without using any organic scavenger, which was 3.3 times higher than that of the neat ZnO sample. The NixPy co-catalyst increased the visible light absorption ability of ZnO, accelerated the transfer of photoexcitons, and subsequently facilitated the NRR.

2-Dimensional (2D) co-catalysts has been also proposed to facilitate charge separation and promote N_2 chemisorption and activation. For instance, Liao *et al.*[141] increased by 5 times the NH_3 production of bare TiO_2 P25 by using a Ti_3C_2 MXene as a co-catalyst, achieving 10.74 μmol h^{-1} g^{-1} under full spectrum light irradiation and using water as the proton source. They inferred that Ti_3C_2 MXene co-catalysts favored the separation of photogenerated carriers by storing the photogenerated electrons in P25, and by promoting the chemisorption and activation of N_2 molecules. Similarly, Shen *et al.*[142] reported the use of a 2D black phosphorus nanosheets (BPNSs) co-catalyst coupled to CdS to achieve a rapid charge separation and transfer within the heterojunction. The authors obtained a 3.73-fold higher NH_3 production (359.51 μmol h^{-1} g^{-1}) than that of bare CdS, in the presence of methanol as the sacrificial reagent and under visible light illumination ($\lambda > 420$ nm).

4.4.2. Morphology control. A commonly adopted catalyst design strategy is morphological control. Some examples of structural modifications include the creation of 1-D nanowires, 2-D nanosheets, and 3D porous/hollow structures. In general, large specific surface areas maximize the availability of active sites and facilitate reactants diffusion. Besides, the formation of stepped surfaces on active sites and edge-rich shapes are found to be the most favorable configurations for N_2 dissociation.[105,143] Bian *et al.*[144] synthesized edge-rich black phosphorus nanoflakes (~90 nm wide) by a chemical etching exfoliation method, obtaining a stable ''polycrystalline'' like structure covered by edges of crystal-domains. These authors reported a NH_3 production rate of 2.37 mmol h^{-1} g^{-1} under visible-light irradiation and using Na_2S/Na_2SO_3 as hole scavenger, which ascribed to the increased catalytic/adsorption sites rendered by the edge-rich surface. On the other hand, Cui *et al.*[145] synthesized different Cu ion-doped $W_{18}O_{49}$ materials with ultra-thin nanowire and sea urchin-like microsphere morphologies by a simple solvothermal method. They obtained a higher formation of OVs for the microspheres, which facilitated N_2 chemisorption and activation through proton coupling. Besides, they associated the improved NH_3 generation with the formation of ultrafine Cu_2O NPs with a high content of defective trap states, which could facilitate the efficient capture of photoexcited electrons to drive NRR to NH_3. Xue *et al.*[146] reported a photocatalytic NH_3 production of 8.16 mM h^{-1} g^{-1} over a porous few-layer g-C_3N_4. This material surpassed by 2.8 times the NRR performance of pure g-C_3N_4 (2.90 mM h^{-1} g^{-1}). The authors associated the improved photoactivity with the few-layer morphology and the ultrathin nature of the catalyst, which provided a larger specific surface area, more exposed active sites, narrowed bandgap, and reduced diffusion path of charges and protons from the bulk to the surface. Ultra-small (<2 nm) metal-based nanoclusters, a special class of materials with only few numbers of atoms, have a big potential for NRR due to their atomic-level properties and their unsaturated surface active sites.[129] Li *et al.*[147] synthesized a Ge^{4+} doped GaN nanowires, which were able to stabilize ultra-small Ru subnanoclusters (~0.8 nm) with high loading density up to 5 wt%. They demonstrated that Ge-doped GaN could act as an efficient electron donor for the Ru co-catalyst, forming a metal/semiconductor interfacial Schottky barrier junction, and resulting in partially negatively charged Ru species with an enhanced photocatalytic performance.

In addition, morphological control can be employed as a strategy for broadening the light absorption range of semiconductors, aiming at full spectrum utilization. In particular, tailoring the particle size of the catalysts can change their band gap energy through quantum sizing effects. For instance, Sun *et al.*[148] reported the synthesis of bismuth monoxide (BiO) quantum dots (size of 2–5 nm), which delivered an ammonia synthesis rate of 1226 μmol h^{-1} g^{-1} in water and under simulated solar illumination, which did not show obvious deactivation even after 120 h. Later on, Liang *et al.*[149] proposed a heterojunction between BiO quantum dots and nitrogen defective ultrathin carbon nitride. This system comprised low-valent Bi^{2+} and nitrogen vacancies, which enhanced the optical absorption ability of the heterojunction, improve charge separation, and led to a NH_3 production rate of 576.11 μmol h^{-1} g^{-1} under visible light illumination (AQE = 0.53% at 400 nm).

4.4.3. Catalyst configurations focused on HER inhibition. It is well known that H atoms adsorb easier than nitrogen on the surface of most catalysts. Thus, selecting supports and active species with poor HER activity is key to achieve a high NRR selectivity (see also Section 4.2). For instance, early transition metals (*e.g.* Ti, Zr, Y, Sc) are good candidates to restrict the HER process, due to their stronger binding ability towards N atoms than H atoms.[38] Additional configurations include single-atom catalysts, multilevel catalyst configurations, or building hydrophobic protection layers.

4.4.3.1. Single-atom catalysts. Atomically dispersed catalysts have recently emerged as an appealing strategy to boost N_2 activation and regulate the catalytic pathways (*i.e.* increase NRR selectivity and inhibit HER).[150] This approach affords highly exposed metal centers in which d orbitals of transition metals are hybridized with *p* orbitals of main group elements, leading to a partial electron transfer from the metal atom to the support material.[150] The so-called single-atom catalysts (SACs) are generally used for electrocatalytic applications, including e-NRR. However, their use in light-driven NRR is scarce to date and mostly based on theoretical studies.[151,152] Reported experimental works are based on single metal atoms (Mo, Cu) immobilized on a carbon nitride (C_3N_4) photocatalyst. Li and co-workers[153] synthesized a Mo-C_3N_4 forming two-coordinated MoN_2 species, which effectively adsorbed N_2 and weaken the N≡N bond. These authors achieved a visible-light driven NH_3 evolution rate of 50.9 μmol g^{-1} h^{-1} in pure water, and 830 μmol h^{-1} g^{-1} using ethanol as electron scavenger with a quantum efficiency of 0.70% at 400 nm. Liu *et al.*[154] studied the incorporation of La single atoms in an oxygen-deficient MoO_{3-x}, founding a strong N_2 activation ability due to the back-donation of electrons from La atoms to 2π* molecular orbitals of adsorbed N_2. This single atom La photocatalyst delivers an impressive NH_3 production rate of 209.0 μmol h^{-1} g^{-1} under visible illumination, without any sacrificial agent. Li *et al.*[155] successfully anchored single Pt atoms at the $-N_3$ sites of stable and ultrathin covalent triazine framework (CTF) nanosheets, aiming to achieve a better separation of photogenerated carriers. They obtained an averaged NH_4^+ production rate of 171.4 μmol h^{-1} g^{-1} (AQE = 1.4% at 420 nm) under visible light irradiation and in the absence of any sacrificial agent.

4.4.3.2. Multilevel catalyst configurations. An additional approach consists on building multilevel catalyst configurations, which may help to limit the electron accessibility during the NRR to control HER. However, it should be noted that an excessive low electron transfer to the active sites can conduce to low NRR efficiencies. Examples of this type of configuration include support–semimetal catalyst (*e.g.* Sn, Bi), support–conductive polymer catalyst (*e.g.* polyaniline (PAN), polyimide, polypyrrole), and support–insulator–catalyst (see Fig. 9).[38]

4.4.3.3. Hydrophobic protection layer. Since N_2 molecules have poor solubility and diffusion coefficient in water, the photo(electro)catalytic ammonia production rates can be limited by diffusion processes in conventional liquid–solid diphase systems.[42] Gas pre-saturation can improve the reaction efficiency but the slow gas diffusion to the catalytic centers cannot be increased, and this inevitably results in low reaction kinetics.[156] An efficient strategy to circumvent these solubility and diffusion limitations consists on building a hydrophobic protection coating on the catalytic active sites, creating a gas–solid–liquid triphasic system. This configuration is based on the cooperative interaction between micro-/nanocomposites

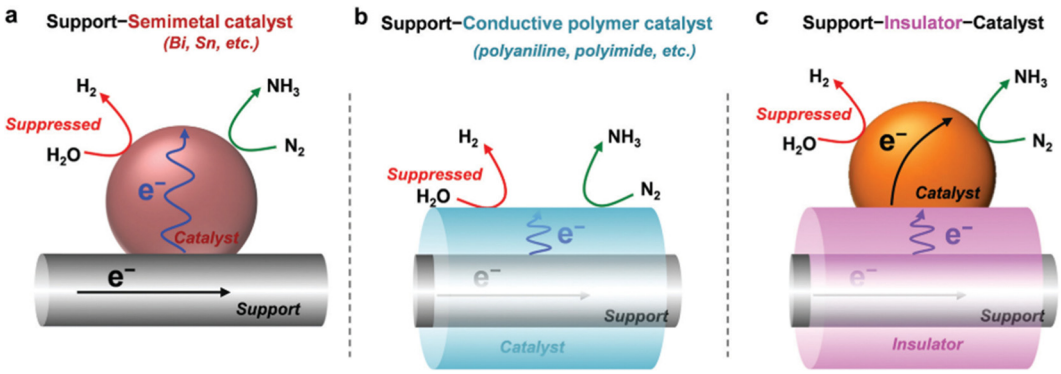

Fig. 9 Multilevel catalyst configurations for limiting the electron accessibility in NRR, including (a) support–semimetal catalyst; (b) support–conducive polymer catalyst; and (c) support–insulator catalyst. Reprinted with permission from ref. 38 Copyright 2021, Royal Society of Chemistry.

and low surface energy materials. Here, catalyst nanoparticles are located at the gas–liquid interface through surface tension regulation, and reactant gases (N_2 or air) are continuously fed to the system. The creation of such gas–solid–liquid triphase limits the coverage of H_2O molecules on the catalyst surface, because this configuration forms gas pockets trapped inside the structure when they are immersed in water. Thus, N_2 molecules can be readily delivered to the catalytic sites from the gas phase, reaching much higher local nitrogen concentrations and eliminating the gas diffusion limitation of conventional diphase systems.[42,156] Besides, this approach is an efficient strategy to lower HER kinetics and thus favor NRR selectivity. In addition, triphase systems holds a great economic potential because they also restrict the possible oxidation of ammonia, thus allowing the direct use of air instead of pure nitrogen.[156]

Some successful examples of hydrophobic layers reported for light-driven NRR include alkanethiols, porous poly (tetrafluoroethylene) (PTFE) frameworks,[157] Poly(*N*-isopropylacrylamide) (PNIPAm),[158] polydimethylsiloxane (PDMS),[159] carbon cloth,[160] or zeolitic imidazolate frameworks (ZIF)[85] with hydrophobic cavities that block water and favor N_2 permittivity.

5. Ammonia production technologies

5.1. Thermocatalytic-NRR

The thermocatalytic synthesis of ammonia from its elements is considered as one of the greatest discoveries of the 20th century, providing enough fertilizer supply to sustain the growing world population.[161] Ammonia is produced nowadays in large plants (1000 to 1500 t day^{-1})[20] *via* the H–B ammonia synthesis loop (Fig. 10a), which is also known as the industrial process that made bread from air.[162,163] At present, conventional H–B plants produce ammonia using natural gas (50%), oil (31%) or coal (19%) as fossil feedstock.[164] Ammonia is produced by shifting the reaction equilibrium ($1/2N_2 + 3/2H_2 \leftrightarrow NH_3$) of a high purity N_2/H_2 gas mixture towards the formation of ideally 22.7 mol% NH_3 (relative to stoichiometric conversion),[165] under high temperature and pressure (*ca.* 350–550 °C, 20–40 MPa) and in the presence of an alkali-promoted Fe catalyst (either magnetite or wüstite).[16,18] This historical technology is able to convert N_2 and H_2 to NH_3 in a single reaction with around ~15% efficiency, and requires the recirculation of unreacted N_2 and H_2 to achieve overall NH_3 conversion of *ca.* 97%.[16,22]

5.1.1. Active materials and surface reactivity. Fe- and Ru-based catalysts were the first materials used for thermocatalytic ammonia production, mainly due to their optimal adsorption/desorption energies (Fig. 10b). Among Fe catalysts, magnetite (Fe_3O_4) was considered one of the best performing catalysts during the first years of development of the technology. Fe and Ru catalysts were commonly mixed with electronic and structural promoters to achieve higher NH_3 yields. Electronic promoters (*e.g.* alkali or alkaline earth metals, rare earth oxides or metallic oxides[167–169]) increase the electron density on the metal surface (*e.g.* Ru, Fe) and this may weaken the N_2 triple bond.[168,170] On the other hand, structural promoters (*e.g.* Al_2O_3, TiO_2, Cr_2O_3, MgO, MnO, CaO or SiO_2) generally improve the specific surface area and neutralize acidity.[168] Specifically, promoted Ru/C catalyst was used in the industrial KAAP (Kellog advanced ammonia process) process, achieving NH_3 yields of 40–50%.[171] These catalysts allowed to operate at milder conditions (370–400 °C, 50–100 atm) than Fe catalysts and showed a higher resistance to O_2, H_2O or CO poisoning.[168,172] Other widely used catalysts include FeO (wüstite), CeO_2, and catalysts based on transition metals located at both sides of the volcano plot, such as Co and Mo (*e.g.* Co–Fe_3O_4, Co–Mo–nitride, *etc.*).[173,174]

Over the past years, alternative catalysts have emerged for low-temperature ammonia synthesis such as electrides, hydrides, oxides and amides, among others. Electrides are very unique crystals with cavity-trapped electrons, which can act as electron-donating materials. Some examples studied for ammonia synthesis include Ru/C12A7:e^-,[175–177] Ru/Ca_2N:e^-,[178] LaRuSi,[179] Ru/BaO/CaH_2,[180] Ru/LaScSi.[181] An

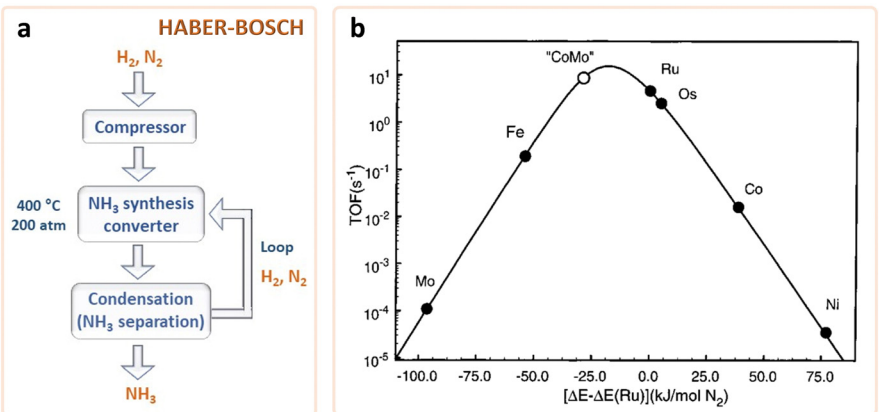

Fig. 10 (a) Simplified diagram of Haber–Bosch ammonia synthesis. Reprinted with permission from ref. 26 (b) Volcano plot for ammonia synthesis on late transition metals, showing the ammonia production rate as a function of the nitrogen adsorption energy. The point denoted as "CoMo" represents a mixed site containing both Co and Mo. Reprinted with permission from ref. 166 Copyright 2001 ACS.

outstanding NH_3 production rate of 2.7 mmol h^{-1} g^{-1} was obtained by Kitano and co-workers[177] using Ru/C12A7:e^- (360 °C, 0.3 MPa). They used the high electron density of electrides and their reversible hydrogen storage–release ability to avoid the well-known hydrogen poisoning of Ru. A year later, these authors developed a best performing Ru/Ca_2N:e^- electride[178] able to work even at 200 °C, which delivered a maximum NH_3 production rate of 3386 mmol h^{-1} g^{-1} (at 340 °C, 0.1 MPa) comparable to the reference Ru(2%)–Cs/MgO. Under similar reaction conditions, these authors also obtained outstanding ammonia production rates (*ca.* 4002 mmol h^{-1} g^{-1}) exploring the partial conversion of a pure hydride (Ru/CaH_2) into an electride (Ru/$CaH_{2-x}(e^-)_x$), due to the easy desorption of hydrogen (>200 °C) from CaH_2 surface in presence of a Ru catalyst.[178]

In the case of hydrides, these materials are attractive candidates for ammonia production due to their strong reducing character and their reversible H_2 storage capacity, as they are used as electron/proton donors. Some examples of the most active metallic hydrides reported for thermocatalytic NH_3 production include LiH,[182,183] VH,[184] binary hydrides (BaH_2,[180,185] TiH_2,[186] CaH_2,[178,180] ZrH_2[187]), mixed-anion hydrides (Ca_2NH, Li_4RuH_6[188]), nitride-hydrides (Mn_4N,[189] BaCrHN[190]), perovskite and lantanide oxyhydrides (Ru/$BaCeO_{3-x}N_yH_z$, $BaTiO_{2-x}H_x$),[191–194] hydride-based electrides.[195] Interestingly, hydrides have achieved NH_3 synthesis in the range of 50–100 μmol h^{-1} g^{-1} using mild temperatures such as 50–150 °C, and using catalysts based on Co–BaH_2, CaFH hydride, Fe–BaH_2–BaO/CaH_2 and BaCr nitride-hydride (BaCrHN).[190,196,197]

Other interesting materials include metal oxides (*e.g.* oxygen vacancy-rich CeO_2)[198–200] or amide-based catalysts, which have shown a strong electron donation from $Ca(NH_2)_2$ to Ru metallic phase, achieving NH_3 productions at temperatures below 200 °C during 700 h.[201–206]

5.1.2. Reactor engineering. Industrial reactors for ammonia synthesis loop mainly consist on catalytic converters, centrifugal compressors, and condensers. The catalytic converters can be classified into tube cooled and multibed converters patterns, either with axial, cross-flow or radial gas flows.[171] The space velocities (WHSV) in these production units reach values between 10 000 to 40 000 mL g^{-1} h^{-1}, and can achieve ammonia productions higher than 100 $mmol_{NH_3}$ h^{-1} g^{-1}.[171,173,207] The catalytic converters are resistant to carbonization[171] and steel embrittlement due to hydrogen diffusion.[208,209] However, new steel alloys were introduced to prevent the nitridation of iron when it is in contact with ammonia at high temperatures.[171] The centrifugal compressors, which replace reciprocating compressors,[208] allow to reach the required operation pressures (150–250 bar) in the synthesis loop, as well as to recycle the gas stream to reach more than 20% of ammonia in each pass.[171] Today, industrial ammonia plants have an integrated design to improve energy recovery and efficiency. Relevant technological improvements include: revamping or modernization of existing converters; use of bigger converters with more efficient designs; development of innovative radial-flow ammonia converters with a very low pressure drop to increase ammonia yield; use of lower pressure systems; and implementation of energy saving designs.[210,211]

5.2. Photocatalytic-NRR

5.2.1. Active materials and surface reactivity. The first work on photocatalytic nitrogen fixation in water was reported by Schrauzer and Guth[212] in 1977. These authors obtained an optimum ammonia production rate of 5.2 nmol h^{-1} g^{-1} at 40 °C, using a Fe-doped TiO_2 catalyst under UV illumination (360 W Hg-Arc lamp). Later on, a compilation of subsequent results was summarized by Schrauzer,[213] who further proposed a N_2 photoreduction pathway *via* stepwise diazene and hydrazine intermediates. Since then, photocatalytic-NRR works have grown exponentially (Fig. 1), putting the focus on active materials and reaction optimization. In general, NH_3 production rates in aqueous phase are in the μmol–mmol range, with some works that have reported rates close to 30 mmol h^{-1} g^{-1} (Table 1). Until now, the most active photocatalysts reported so far are based on graphdiyne, graphitic carbon nitride (g-C_3N_4), bismuth oxyhalides, TiO_2-based materials, and even metal organic frameworks (MOFs), all frequently modified with metal co-catalysts and dopants (*e.g.* Co, Fe, Cu, Ni, Ru). Many of these works also use sacrificial agents and illumination sources based on Xe lamps (generally 300 W power, with or without wavelength filters).

The most active NRR photocatalyst reported to date is based on stable porous graphdiyne (GDY) decorated with Co quantum dots,[214] which achieved a maximum NH_3 production rate of 26.5 mmol h^{-1} g^{-1} and a AQE of 8.7% without any sacrificial agent (see Fig. 11 and Table 1). This high catalytic performance was ascribed to the rapid conversion of valence states of Co species (Co^{2+}/Co^{3+}) together with the GDY. Recently, a similar heterojunction based on magnetite/GDY[236] showed a remarkable NH_3 production of 1.8 mmol h^{-1} g^{-1} without sacrificial agent. These authors demonstrated that the coordination environment and valence state of the Fe atoms in magnetite can be also modified by incorporating GDY, resulting in a high-performance heterojunction.

An extraordinary NH_3 production rate of 23.5 mmol h^{-1} g^{-1} was reported by Liu *et al.*[215] using g-C_3N_4 nanorod arrays modified with cyano groups (–C≡N) and K centers. Interestingly, this work used air as N_2 source and reported an operational temperature of 5 °C. This good performance was explained by the coexistence of both sites: –C≡N groups with electron donation effect for N_2 activation, and K centers that act as electron trapping sites, promoting charge separation. Zhang *et al.*[216] combined a 3D porous g-C_3N_4 with NVs and $CoFe_2O_4$ to create a Z-scheme heterojunction that achieved a NH_3 production rate of 14.7 mmol h^{-1} g^{-1}. This catalytic system presented wider light absorption, faster electron transfer rates and stronger N_2 adsorption and activation than the g-C_3N_4 counterpart. Fan *et al.*[224] supported OV-rich $In(OH)_3$ on g-C_3N_4, obtaining a OD/2D heterojunction with many chemisorption sites for N_2, efficient electron–hole separation and thus prolonged carriers lifetime.

Table 1 Best performing photocatalysts (mmol range) for ammonia production

Photocatalyst	T (°C)	Phase	Light source	Reagents	Hole scavenger	NH_3 production rate[a] (mmol h^{-1} g^{-1})	STA (%)	AQE,[b] ξ[c] (%)	Year	Ref.
Porous graphdiyne with Co QD[d]	20	Liquid	300 W Xe lamp	N_2, Na_2SO_4 (0.1 M)	—	26.5	—	8.72[b] (500 nm)	2021	214
Bi defective K/g-C_3N_4	5	Liquid	300 W Xe lamp	Air, H_2O	Methanol	23.5	—	—	2022	215
g-C_3N_4/$CoFe_2O_4$	Room	Liquid	250 W Xe lamp	N_2, H_2O	—	14.7	—	—	2023	216
Bi_5O_7Br	Room	Liquid	300 W Xe lamp	N_2, H_2O	—	12.7	—	—	2020	217
Ni-ZrO_2/Bi_2O_3	Room	Liquid	Sunlight (65500 lux)	N_2, H_2O	TEOA[e]	9.7	—	—	2023	218
Porous few-layer g-C_3N_4	Room	Liquid	500 W Xe lamp (AM 1.5G)	N_2, H_2O	Methanol	8.2	—	—	2020	146
Bi_2Te_3/BiOCl	Room	Liquid	UV and Vis	N_2, H_2O	Methanol	7.9	—	—	2018	219
Cu/TiO_2	Room	Liquid	300 W Xe lamp (AM 1.5G)	N_2, H_2O	Glycerol	6.8	—	—	2020	139
S-doped g-C_3N_4	Room	Liquid	500 W Xe lamp	N_2, H_2O	Methanol	6.0	—	—	2018	220
FeS_2-FeP-CeO_2	25	Liquid	250 W Hg lamp	N_2, H_2O	Methanol	5.6	—	—	2019	221
UiO-66(−NH_2)/$CuInS_2$	Room	Liquid	250 W Xe lamp	N_2, H_2O	Methanol	4.0	—	—	2023	222
Ru/H_xMoO_{3-y}	Room	Gas	300 W Xe lamp (420 nm filter)	N_2, H_2	—	4.0	—	6.0[b] (650 nm)	2022	223
In$(OH)_3$/C_3N_4	25	Liquid	300 W Xe lamp (420 nm filter)	N_2, H_2O	TEOA[e]	3.8	—	—	2020	224
KOH treated g-C_3N_4	25	Liquid	300 W Xe lamp	N_2, H_2O	Methanol	3.6	—	21.5[b] (420 nm)	2018	225
Ag-Bi_2S_3/MnOS	Room	Liquid	300 W tungstate lamp	N_2, H_2O	Methanol	3	—	—	2023	226
Au-Os/Cs_2O	60	Gas	Solar simulator	N_2, H_2	—	2.7	—	—	2015	227
CL@BiOBr-OV/Au[f]	Room	Liquid	300 W Xe lamp	N_2, H_2O	—	2.6	—	—	2022	228
Black phosphorus	Room	Liquid	LED lamp (420 nm)	N_2, H_2O	Na_2SO_3 and $Na_2S\cdot 9H_2O$	2.4	—	—	2020	144
MOF-74@C_3N_4	Room	Liquid	300 W Xe lamp	N_2, H_2O	Methanol	2.3	—	—	2020	229
TiO_2/$SrTiO_3$/g-C_3N_4	Room	Liquid	300 W Xe lamp	N_2, H_2O	Methanol	2.2	—	3.03[b] (365 nm)	2020	230
Bi_5O_7I	20	Liquid	300 W Xe lamp	N_2, H_2	Methanol	2.2	—	5.1[b] (365 nm)	2016	231
ZnInCuS QD[d]/BiOI	Room	Liquid	250 W Hg lamp (420 nm filter)	N_2, H_2O	—	2.1	0.24	—	2023	232
g-C_3N_4	Room	Liquid	300 W Xe lamp (AM 1.5G filter)	N_2, H_2O	Methanol	1.9	—	7.79[b] (370 nm)	2023	233
BiMnO/BiOIBr	Room	Liquid	Solar simulator	N_2, H_2O	Methanol	1.8	—	3.6[b] (420 nm)	2023	234
MPc-POF[g]	Room	Liquid	300 W Xe lamp	N_2, H_2O	Methanol	1.8	—	0.5[b] (400 nm)	2023	235
Graphdiyne@Janus magnetite	Room	Liquid	300 W Xe lamp	N_2, Na_2SO_4 (0.1 M)	—	1.8	—	—	2021	236
ZnCuInS–BiOI	Room	Liquid	250 W Hg lamp	N_2, H_2O	—	1.6	0.36	—	2023	232
NC-g-C_3N_4[h]	Room	Liquid	300 W Xe lamp (AM1.5)	N_2, H_2O	Methanol	1.6	—	—	2019	237
Zr/MOFs	Room	Liquid	150 W Xe lamp (420 nm filter)	N_2, H_2O	—	1.5	—	—	2023	238
Bi@BiOBr	Room	Liquid	300 W Xe lamp	N_2, H_2O	—	1.4	—	—	2021	239
TiO_2/BiOBr	Room	Liquid	300 W Xe lamp	N_2, H_2O	Methanol	1.4			2021	240
WS_2@TiO_2	Room	Liquid	Simulated sunlight (AM1.5)	N_2, H_2O	Na_2SO_3 (0.01 M)	1.4	—	—	2020	241
Bi_5O_7Br	Room	Liquid	300 W Xe lamp (400 nm filter)	N_2, H_2O	—	1.4	—	2.3[b] (420 nm)	2017	242
H-Bi_2MoO_6	Room	Liquid	300 W Xe lamp	Air, H_2O	—	1.3	—	2.4[b] (420 nm)	2016	243
Ru–Pd/g-C_3N_4	Room	Liquid	300 W Xe lamp	N_2, H_2O	Ethanol	1.3	—	6[c]	2021	244
BiO quantum dots	25	Liquid	500 W Xe lamp	N_2, H_2O	—	1.2	—	—	2017	148
$CeCO_3OH$/g-C_3N_4/CeO_2	Room	Liquid	500 W Xe lamp	Air, H_2O	—	1.2			2019	245
$CeCO_3OH$	Room	Liquid	300 W Xe lamp	N_2, H_2O	—	1.1	—	0.98[b] (380 nm)	2022	246
TiO_2/Au/K^+	Room	Liquid	Xe lamp (400 nm filter)	N_2, H_2O	Methanol	1.0	—	0.93[b] (550 nm)	2021	247
TiO_2/MIL-88A(Fe)/g-C_3N_4	25	Liquid	300 W Xe lamp	N_2, H_2O	Methanol	1.0	—	—	2023	248
Fe-doped BiOCl	Room	Liquid	300 W Xe lamp	N_2, H_2O	—	1.0	—	1.8[b] (420 nm)	2019	249

[a] Photocatalytic activity determined from experimental data from each reference. [b] Apparent quantum efficiency. [c] Photonic efficiency. [d] Quantum dots. [e] Triethanolamine. [f] CL: carbonized loofah sponge. [g] POF: porous organic framework. [h] NC: nitrogen defects and cyano groups.

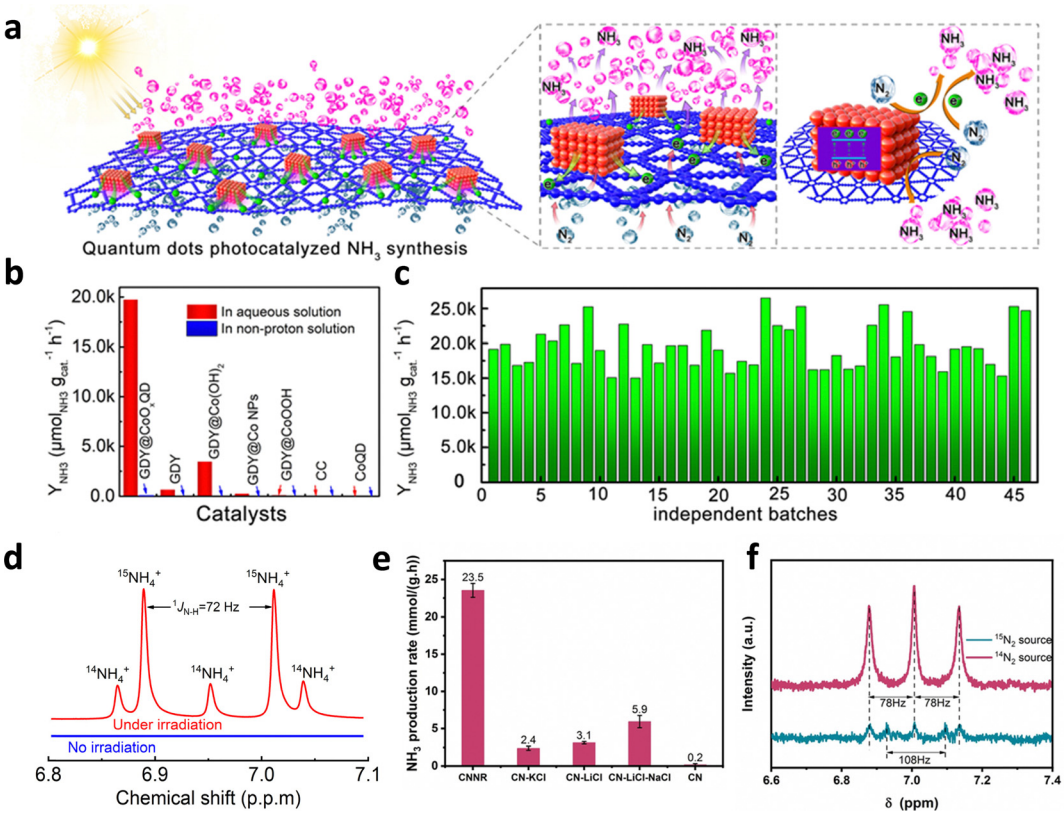

Fig. 11 (a) Schematics of photocatalytic NRR on porous graphdiyne decorated with Co quantum dots; (b) NH_3 production rates in different solutions and (c) in independent experiments; (d) $^{15}N_2/^{14}N_2$ isotopic labeling tests under (red) and without (blue) irradiation. Reprinted with permission from ref. 214 Copyright 2021 Elsevier. (e) Photocatalytic NH_3 production with different g-C_3N_4 samples; (f) ^1H NMR spectra for nanostructured g-C_3N_4. Reprinted with permission from ref. 215 Copyright 2022 Elsevier.

In the case of bismuth oxyhalides (BiOX, X = Cl, Br, I), the formation of OVs with abundant localized electrons on the surface play a critical role for NRR, mainly for N_2 adsorption and activation.[217–239] These materials have been combined with other inorganic semiconductors within binary heterojunctions to boost performance.[219–240]

Of special interest is the more recently emerged sunlight-driven nitrogen fixation from air. The big challenge of this approach relays on the competition between N_2 and O_2 for photogenerated electrons, since O_2 is more easily reduced than N_2 due to its lone pair electrons and this suppresses NH_3 formation.[250] Hirakawa *et al.*[121] demonstrated that air bubbling suppresses NH_3 formation over a commercial TiO_2 sample with a large number of surface Ti^{3+} species. Despite this, the sustainability benefits of aerobic NRR is encouraging the development of research works on this field using a wide variety of materials, such as bismuth molybdate,[243] Fe–WO_3,[251] Ti/Mo composite,[252] CoF_2O_4,[253] Co_3O_4@Schiff,[254] and binary[255–257] or ternary[258] heterojunctions. In this aerobic route, both NRR and NOR may coexist (Fig. 12). Zhao *et al.*[256] reported that the reaction mechanism towards ammonia follows an alternative redox pathway, in which N_2 and O_2 can be trapped at OVs, generating nitric oxide (*NO) as active intermediate that is further photoreduced to ammonia. DFT calculations supported this point by founding a lower free energy barriers for N_2 activation ($*N_2 \rightarrow *N–NO$, −0.08 eV) and and rate-limiting step ($*NO \rightarrow *NHO$, 1.23 eV) than traditional NRR ($*N_2 \rightarrow *N–NH$, 1.48 eV and $H_2N–NH_2 \rightarrow *NH_2$, 1.29 eV, respectively).

5.2.2. Reactor engineering. In general, photocatalytic NRR tests are carried out in liquid-phase, using stirred batch reactors or flowing fixed bed reactors made of glass or provided with a quartz window for illumination. Homogeneous or heterogeneous photocatalysts are dispersed in a N_2-saturated solvent, most often pure water. NRR tests are usually performed under mild reaction conditions, such as low temperature (room T – 60 °C) and atmospheric pressure, either in the presence or absence of sacrificial agents. These one-pot reaction configurations possess intrinsic limitations to achieve a high ammonia yield and selectivity. Namely, soft reaction conditions limit the solubility of N_2 in water, while the lack of separation of redox processes favors the simultaneous occurrence of parallel reactions (*e.g.* HER, oxidation of ammonia into NO_x or N_2 by photogenerated holes).

A rational configuration of photocatalytic reaction systems holds the potential to improving ammonia yield and selectivity. Next-generation photoreactors should enable the spatial separation of ammonia and oxidative species to avoid back reactions, for instance by using products separation membranes. This spatial separation would also maximize the utilization of photogenerated carriers towards target products, that

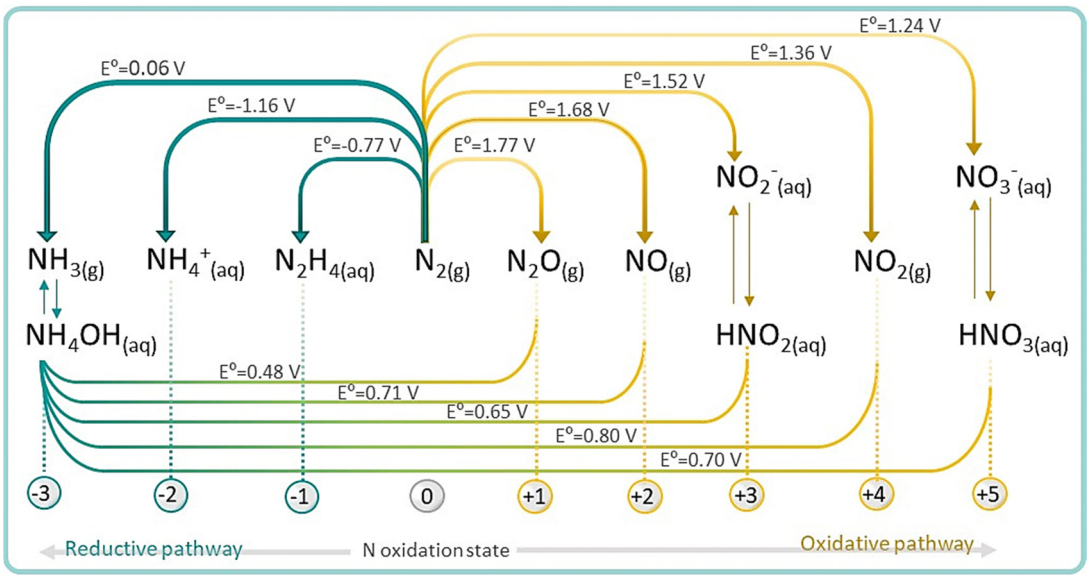

Fig. 12 Possible reductive and oxidative pathways (left- and right-side figure, respectively) in N_2 photofixation. Redox potentials (E°) are referred to the normal hydrogen electrode (NHE). Adapted from ref. 259.

is the production of ammonia using photoelectrons, and the synthesis of nitrates consuming photoholes. This approach would further increase the added value of the photocatalytic process if nitrogen fixation products are even enriched by forming ammonium nitrate or urea.

5.3. Photoelectrocatalytic- and (PV)-electrocatalytic- NRR

The use of the light to reduce the necessary potential of a certain electrocatalytic reaction has already been extensively employed among the scientific community.[260,261] As previously occurred with other interesting chemical reactions, there are two main strategies to achieve this purpose: (i) the direct use of photoelectrocatalytic materials (*i.e.* semiconductors able to generate electron–hole pairs and also drive the desired reaction[262,263]), or (ii) coupling of a photovoltaic cell, which generates the carriers, with an electrocatalytic material that drives the chemical reaction.[264–266] Aiming to ease the readers comprehension, these two ammonia production technologies will be described separately in the following sections.

5.3.1. Photoelectrochemical (PEC) ammonia production. The use of renewable energies to electrocatalytically reduce N_2 is one of the most promising approaches for sustainable ammonia synthesis. In fact, electrochemical N_2 conversion efficiencies are very high when compared to photocatalysis.[88] The electrochemical N_2 reduction reaction (e-NRR) takes place at the electrolyte–electrode interface, in which protons need to be transferred from the electrolyte, and electrons on the electrode surface are transferred to adsorbed N_2 molecules for subsequent activation. Usually, both the first electron transfer process ($N_2 + e^- \leftrightarrow N_2^-$; −3.37 V *vs.* RHE, pH = 14) as well as the first proton addition ($N_2 + H^+ + e^- \leftrightarrow N_2H^+$; −3.20 V *vs.* RHE) can be activated with applied potential, which in principle are not thermodynamically favorable.[88] However, the presence of deficient sites and the occurrence of the competing HER usually lead to minimal yield and low faradaic efficiency (FE) during the electrocatalytic synthesis of ammonia. That is why the integration of electrocatalysis and photocatalysis in a photoelectrochemical (PEC) cell is an effective way to overcome these dark NRR limitations (Fig. 13). PEC-NRR offers reduced energy consumption than NRR and other advantageous green features, such as the direct conversion of solar energy into chemical energy, which can potentially lead to higher overall efficiency compared to dark electrocatalysis. Additionally, it exhibits several advantages over conventional photocatalysis since the generated electrical field can induce exciton separation, helping charge separation while reducing charge recombination. Furthermore, a photoelectric synergy is reflected in the coexistence of photochemical and electrochemical reactions.

Since the first photoelectrochemical cell (PEC) publication in 1972,[262] its applications have evolved from water splitting[270] to other fields such as fuel production through CO_2 conversion,[271] reduction of organic compounds and the degradation of contaminants.[271] However, the use of PEC cells in the field of nitrogen reduction reaction (NRR) is still quite limited.[272] Photoelectrochemical N_2 reduction involves three principal stages: (i) charge carriers photogeneration, (ii) separation of charge carriers to the active sites, and (iii) N_2 molecules absorption and reduction reaction, very similar to the photocatalytic process. However, in this case, photogenerated electrons and holes separate to different reaction sites, unless charge recombination. Electrons migrate to the surface of the photocathode and holes goes to the (photo)anode. Thus, electrons drive the N_2 reduction on the active sites of the photocathode ($N_2 + 6H^+ + 6e^- \rightarrow 2NH_3$, $E^0 = -0.148$ V *vs.* RHE), while holes drive the oxidation evolution reaction (OER) on the (photo)anode ($2H_2O + 4h^+ \rightarrow 4H^+ + O_2$, $E^0 = 1.23$ V *vs.* RHE). Despite its promising features, PEC-NRR is still at a

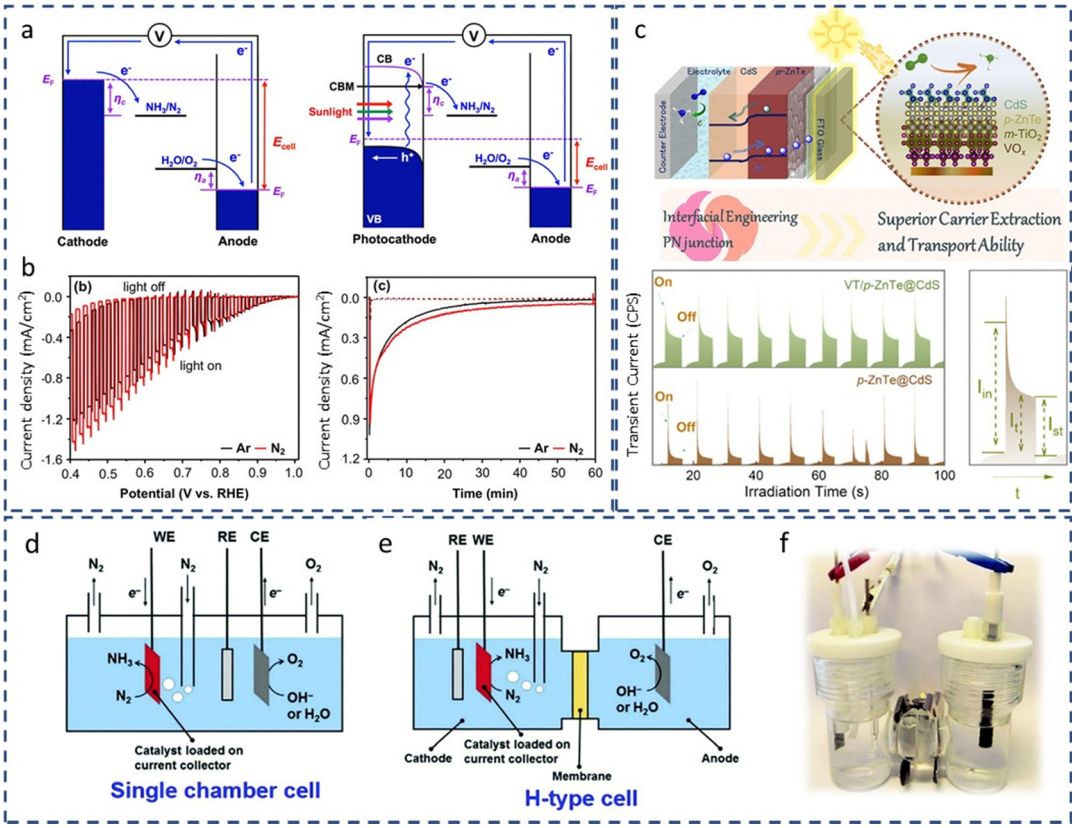

Fig. 13 (a) Comparison of electrochemical (left) and photoelectrochemical NRR (right), depicting the beneficial effect of using a photocathode to decrease the overall cell voltage needed for NRR. (b) *J*–*V* plot (5 mV s^{-1}) and *J*–*t* plot (at 0.6 V *vs.* RHE) of a CuO measured under Ar (black) and $^{15}N_2$ (red) in 0.1 M KOH solutions under AM 1.5G, 100 mW cm^{-2}. The dark currents in the *J*–*t* plot are shown as dotted lines. Reproduced with permission from Jang *et al.*[267] Copyright 2020 American Chemical Society. (c) Scheme of a solar-electrolytic cell, transient photocurrent and dynamics for VT/p-ZnTe@CdS and p-ZnTe@CdS photocathodes. Reproduced with permission from Jia *et al.*[268] Copyright 2023 American Chemical Society. Schematic representation of (d) a single-chamber and (e) an H-type cell with a proton exchange membrane. (f) Photograph showing an H-type cell, highlighting the working electrode (WE), reference electrode (RE), counter electrode (CE), and membrane. Reproduced with permission from Pang *et al.*[269] Copyright 2021 Royal Society of Chemistry.

development stage since the catalytic performance is not yet suitable for practical applications. Typically, PEC-NRR occurs on the surface of p-type materials (photocathodes) with intrinsic structural defects, which may lead to poor visible-light absorption, high exciton recombination, and serious light corrosion. Over the last years, PEC-NRR investigations have focused on developing high-performance photoelectrode materials, which include inorganic semiconductors with suitable band gaps, metallic modifications, organometallic frameworks with tunable structures, and single atoms with notable active sites (see Table 2). Metal oxides have been thoroughly explored as potential photo(electro)catalysts for various catalytic reactions in the energy and environmental sectors. These materials provide benefits such as high catalytic activity, cost-effectiveness, and straightforward preparation. Especially, p-type semiconductors have been tested as photocathodes for PEC-NRR due to their suitable band structures and efficient carrier transport.

Fig. 13a shows a recent study from Jang *et al.*[267] who explored the feasibility of PEC-NRR using CuO and Cu_2O photocathodes, as well as its associated reaction mechanism. The authors observed that both systems exhibited substantial faradaic efficiencies for NH_3 production (17% and 20%, respectively) with minimal H_2 production. Interestingly, the external bias (0.6 V *vs.* RHE for CuO and 0.4 V *vs.* RHE for Cu_2O) were less negative than the thermodynamic reduction potential for NRR (0.092 V *vs.* RHE at pH = 13), demonstrating the potential of the photogenerated electrons used for NRR depend on the conduction band minimum of the photocathode. However, they found cathodic photocorrosion of CuO (see Fig. 13b), and pointed out the need for a protection layer. In literature, the surface of Cu_2O photocathodes has been coated with different systems to improve the NH_3 yield and stability, for instance using Cu metal–organic frameworks (MOF) to build Cu-MOF/Cu_2O[292] or Ag-doped Ni MOF heterojunctions.[292]

Very recently, He *et al.*[273] tested a novel donor-site-acceptor system based on a covalent organic framework (COF) and a graphite oxide. They found that the active boron sites, embedded between the acceptor and the donor units, effectively activated chemisorbed N_2 with a continuous electron flow after photoexcitation. This system achieved a faradaic efficiency around 91.6% and 108.2 μg h^{-1} mg_{cat}^{-1} (at −0.4 V *versus* RHE)

Table 2 Selected photoelectrodes for PEC-NRR

Photoelectrode material	Electrolyte	Light source	Max. photocurrent density (mA cm^{-2})	NH_3 production rate	Year	Ref.
COF/GO[a]	0.5 M Na_2SO_4	300 W Xe lamp, 200 mW cm^{-2}	−0.3 mA at −0.7 V RHE	108.20 μg h^{-1} mg^{-1}	2024	273
Ti–WO_3/$SrWO_4$	0.05 M H_2SO_4	AM 1.5G, 100 mW cm^{-2}	−2.05 mA at −0.6 V RHE	11.17 μg h^{-1} cm^{-2}	2024	274
Vo–TiO_2/Ag/TiO_2	0.2 M Na_2SO_4	300 W Xe lamp	−0.5 mA at −0.4 V RHE	51.20 g h^{-1} cm^{-2}	2023	275
PdCu/TiO_2/Si	1 M $LiClO_4$	AM 1.5G, 100 mW cm^{-2}	−4 mA at 0 V *vs.* Li	43.09 μg h^{-1} cm^{-2}	2023	93
Mo_2C/GaN/InGaN	0.05 M H_2SO_4	100 W Xe lamp (AM 1.5G)	−1.4 mA at −0.8 V RHE	7.93 μg h^{-1} cm^{-2}	2023	276
VO_x/m-TiO_2/p-ZnTe@CdS	0.05 M H_2SO_4	Xe lamp, 200 mW cm^{-2}	−4 mA at −0.7 V *vs.* RHE	6.23 μg h^{-1} cm^{-2}	2023	268
PANI-ASSM[b]/CdS-Co_3S_4	H_2SO_4	40 W blue LED	−22 mA at 0.5 V	12.33 μg mol^{-1} h^{-1}	2022	277
CoV-LDH[c]	0.1 M Na_2SO_4	AM 1.5G, 100 mW cm^{-2}	−1 mA at −0.4 V RHE	8.97×10^{-7} mol h^{-1} cm^{-2}	2022	278
Mo-doped WO_3@CdS	0.5 M H_2SO_4 + 5% H_2O_2	300 W Xe lamp	−0.05 mA at −0.3 V *vs.* RHE	38.99 μg h^{-1} mg^{-1}	2022	279
Bi_2S_3 quantum dots on MoS_2	0.1 M Na_2SO_4	300 W Xe lamp	−1.7 mA at −0.6 V *vs.* RHE	18.50 μg h^{-1} mg^{-1}	2022	280
Metal–organic iron terephthalate structure (MOF-235)	0.1 M Na_2SO_4	Hg lamp	−20 mA at −0.7 V *vs.* Ag/AgCl	0.72 μg h^{-1} cm^{-2}	2022	281
$BiVO_4$/PANI[d]	0.1 M Li_2SO_4	300 W Xe lamp	−0.05 mA at −0.35 RHE	0.93 μg h^{-1} cm^{-2}	2021	282
p-type $BiVO_4$	0.1 M Li_2SO_4	300 W Xe lamp	−0.2 mA at −0.2 V RHE	1.6×10^{-8} mol h^{-1} cm^{-2}	2021	283
Cu_2S–In_2S_3	0.2 M K_2SO_4	Xe lamp (100 mW cm^{-2})	−3 mA at −0.9 V *vs.* RHE	23.67 mg h^{-1} cm^{-2}	2021	284
Au/SiO_2/Si	0.05 M potassium phosphate buffer	AM 1.5G, 100 mW cm^{-2}	−0.05 mA at 0.2 V *vs.* RHE	22.0 μg h^{-1} cm^{-2}	2021	285
$MoSe_2$@g-C_3N_4	0.1 M KOH	300 W Xe lamp	−12 mA at −0.5 V *vs.* RHE	7.72 μmol h^{-1} cm^{-2}	2021	286
CuO and Cu_2O	0.1 M KOH	300 W Xe lamp	−1.5 mA at −0.4 V *vs.* RHE	5.3 μg h^{-1} cm^{-2} (CuO) 7.2 μg h^{-1} cm^{-2} (Cu_2O)	2020	267
$W_{18}O_{49}$	0.5 M Na_2SO_4	Xe lamp (1 sun)	−150 mA at −1.8 V Ag/AgCl	9.82 μg h^{-1} cm^{-2}	2020	287
Black phosphorus nanosheets	0.1 M HCl	Xe lamp	−10 mA at −0.5 V *vs.* RHE	102.4 μg h^{-1} g^{-2}	2020	288
NV[e]-g-C_3N_5/BiOBr	0.05 M HCl + 0.05 M Na_2SO_4	Xe lamp (solar simulator)	−1.2 mA at −0.2 V	29.4 μg h^{-1} mg^{-1}	2020	289
Au/PTFE[f]/TS[g]	0.05 M H_2SO_4 + 0.05 M Na_2SO_3	AM 1.5G, 100 mW cm^{-2}	—	≈18.9 μg cm^{-2} h^{-1}	2019	157
MoS_2@TiO_2	0.1 M Na_2SO_4	300 W Xe lamp	−4 mA at −0.6 V *vs.* RHE	1.42×10^{-6} mol h^{-1} cm^{-2}	2019	290
BiOI-OVs[h]	N_2-saturated H_2O	100 mW cm^{-2}	0.4 V *vs.* RHE	140 nmol h^{-1} cm^{-2}	2019	291

[a] COF/GO: Covalent organic framework/graphite oxide. [b] PANI-ASSM: Polyaniline-coated anodized stainless-steel mesh. [c] LDH: Layered double hydroxide. [d] PANI: Polyaniline. [e] NV: Nitrogen vacancy. [f] PTFE: poly(tetrafluoroethylene). [g] TS: Ti layer on Si surface. [h] OVs: oxygen vacancies.

in several cycles, reaching the target value set by the U.S. Department of Energy (90%).

Regarding other active metals for PEC-NRR, Mo is a very interesting candidate since natural nitrogenase contains Mo active sites. Based on DFT calculations, Nørskov and co-workers[293] studied the prospect of electrochemical reduction of N_2 to NH_3 under ambient conditions, and anticipated that Mo provides many additional active sites for N_2 reduction. On this basis, several Mo-based catalysts have been developed for (photo)electrochemical N_2 fixation, and are actually the subject of a recent bibliographic review.[129] We highlight the work by Ye *et al.*[290] who developed a functional MoS_2@TiO_2 structure as a photocathode for PEC-NRR under ambient conditions. They achieved a NH_3 yield rate of 1.42×10^{-6} mol h^{-1} cm^{-2} and a faradaic efficiency of 65.52%, which was a remarkable result at that time. This performance was due to an efficient interfacial charge transport and the synergistic effects between the MoS_2 and TiO_2 counterparts. Another recent example[286] published in 2021 reported the use of $MoSe_2$@g-C_3N_4 as photocathodes, which demonstrated to be inherently active, selective and robust catalysts for PEC-NRR. These cathodes exhibited good NH_3 yield rate (7.72 μmol h^{-1} cm^{-2}) and FE (28.91%) at −0.3 V *versus* RHE at room temperature and pressure. This performance was attributed to the synergistic effects and electronic coupling between $MoSe_2$ and g-C_3N_4 and the improvement in the light harvesting capacity and charge separation efficiency, which led to slow recombination rates and longer lifetime of photogenerated electron–hole pairs.

Other strategy to improve PEC-NRR performance is the construction of a PN junction to accelerate the photogeneration of charge carriers and improve their spatial separation.[289] In this line, we highlight the contribution of Jia *et al.*[268] who developed a photocathode composed by a PN junction (p-ZnTe@CdS) and a VOx/TiO_2 interlayer. This heterostructured photocathode achieved an AQE of 0.6% and a N_2 to NH_3 conversion performance of 6.23 μg h^{-1} cm^{-2} (Fig. 13c). Very recently, Wang *et al.*[274] prepared a Ti–WO_3/$SrWO_4$ heterojunction by simple hydrothermal and spin-coating approaches and use it as photocathode. They found out that this catalyst inhibited the photogenerated carrier's complexation. Ti acted as the N_2 adsorption site, promoting nitrogen activation and thereby improving the carrier transport efficiency and NH_3 synthesis performance. At −0.5 V *vs.* RHE, the ammonia production reached 11.17 μg h^{-1} cm^{-2}, which surpassed that of $SrWO_4$ by four times. Moreover, Ti–WO_3/$SrWO_4$ exhibited high stability and N-gas sensitivity during NRR, showing its suitability for photoelectrocatalytic ammonia synthesis.

On the other hand, vanadium-based materials are promising catalysts for N_2 fixation, as vanadium nitrogenase acts as an important component of the N_2 cycle in nature. In this transition metal, the unoccupied 3d orbital of V facilitates the adsorption of N_2 and serves as a bridge to allow the transfer of photoexcited electrons from the catalyst to the N_2 molecules. $BiVO_4$ is a very suitable matrix for V localization due to its good physicochemical properties, low cost, and very high photostability. However, $BiVO_4$ is generally considered as an n-type semiconductor and therefore, it is frequently used as a photoanode in PEC systems but not for NRR. In contrast, Bai *et al.*[283] reported for the first time the use of a p-$BiVO_4$ photocathode for PEC-NRR under ambient conditions. Interestingly, density functional theory (DFT) calculations revealed that V sites worked as essential active centres for N_2 adsorption/activation. They obtained a NH_3 evolution rate of 11.6×10^{-2} μmol h^{-1} cm^{-2} and a faradaic efficiency of 16.2% at 0.1 V *versus* RHE in 0.1 M Li_2SO_4 solution. Bai *et al.*[282] incorporated PANI (polyaniline) on the $BiVO_4$ surface to create a Z-scheme heterojunction, which accelerated the separation and transfer of photogenerated carriers leading to a NH_3 yield rate of 0.93 μg h^{-1} cm^{-2} and FE = 26.43%.

5.3.2. (PV)-electrocatalytic ammonia production. Only few works have reported the electrocatalytic production of ammonia coupled with a photovoltaic cell. In 2022, Li *et al.*[294] reported a 3.4% solar-to-ammonia from nitrate using a Fe single atom catalyst over 2D MoS_2 nanosheets coupled with an PV cell. In this work, the authors found that Fe–MoS_2 catalyst exhibited excellent NO_3RR performance with a faradaic efficiency as high as 98% for NH_3 production at low overpotentials, *ca.* < -0.5 V *versus* RHE. The DFT analysis explained the higher ability of individual Fe atoms on MoS_2 to activate NO_3^-, due to the strong interaction between the $2\pi^*$ orbital of NO species and the *d* band orbitals of Fe atoms, which resulted in a lower energy barrier for the limiting de-oxidation of NO* to N*. Finally, the authors coupled the catalysts to an InGaP/GaAs/Ge triple-junction solar cell, achieving a STA conversion efficiency of *ca.* 3.4% with a yield rate of 510 μg h^{-1} cm^{-2}. Very recently, K. Yong *et al.* has reported the employment of Tungsten phosphide nanowires as electrocatalyst for NO_3RR.[295] Specifically, the authors combined the NO_3RR with a hydrazine oxidation reaction (HzOR) instead of the combined oxygen evolution reaction (OER) or urea oxidation reaction (UOR), achieving an impressively low potential of 0.24 V for generating a current density of 10 mA cm^{-2} in the overall NO_3RR-HzOR, compared with those required for NO_3RR-OER (1.53 V) and NO_3RR-UOR (1.31 V). Finally, a single perovskite cell was used to form an unassisted NO_3RR-HzOR PV-EC system, while two where required for the NO_3RR-OER, producing a current density of around 23 mA cm^{-2}, and leading to a NH_3 production rate of 1.44 mg cm^{-2} h^{-1}.

Interestingly, in the two previous studies, NO_3^- was used as the nitrogen source for PV-electrocatalytic ammonia production. The reasons behind, are that nitrates present unique advantages as nitrogen sources for electrocatalytic NH_3 production. First, nitrate is widely present in the nature, being a habitual pollutant of water resources, accumulating over time due to agriculture and industrial activity.[296,297] Then, producing ammonia from nitrates, is both a renewable energy source and a pollution mitigation strategy. And secondly, the bond energy of N=O (204 kJ mol^{-1}) is around 4 times weaker than the triple N≡N bond, making this bond easily activated at lower energies.[298]

5.3.3. (Photo)electrochemical reactor engineering. Since Van Tamelen *et al.*[299] demonstrated the electrochemical

Table 3 Recent high performing catalysts (mmol range) for photothermocatalytic ammonia production

Photothermal catalyst	T (°C)	Light source	Reagents	NH_3 production rate[a] (mmol h^{-1} g^{-1})	STA	AQE,[b] ξ[c]	Year	Ref.
Ru–Cs/ZrO_2	350	300 W Xe lamp (1 Sun)	N_2, H_2	5.1	—	39%[b]	2023	306
Ru–Cs/MgO	333	Blue LED light	N_2, H_2	4.5	—	—	2019	307
Ru/C	380	Concentrated sunlight	N_2, H_2	3.5 (0.1 MPa)	—	—	2023	308
CsRu@$SrTiO_3$	360	300 W Xe lamp	N_2, H_2	3.5	—	—	2022	305
Fe–MoS_2	270	70 W tungsten lamp	N_2, H_2O	2.1–17[d] (6 bar)	0.24–0.18% (solar furnace)	37.1%[b] (432 nm)	2021	309
Pt-Ptn-TiN	280	Xe lamp (6 Sun)	N_2, H_2	0.5	—	0.03%[b] (465 nm)	2023	310
Ni/TiO_2	400	300 W Xe lamp	N_2, H_2	0.2	—	—	2021	311
K/Ru/$TiO_{2-x}H_x$	360	300 W Xe lamp	N_2, H_2	0.1	—	—	2018	312
$TiO_{2-x}H_y$/Fe	495	Xe lamp (102 Sun)	N_2, H_2	—	3.9×10^{-4}	—	2019	39

[a] Photocatalytic activity determined from experimental data from each reference. [b] Apparent quantum efficiency. [c] Photonic efficiency. [d] Value obtained under 6 bar pressure.

synthesis of NH_3 in a single-compartment reactor in 1968, several reaction systems, electrolytes and reaction parameters have been investigated to implement the (photo)electrochemical synthesis of NH_3 under mild conditions. A traditional configuration for PEC-NRR consists on a photocathode (catalyst), an anode or photoanode (tandem cell) acting as counter electrode, an electrolyte, and a nitrogen gas feeding. The cathodic chamber is filled with water vapor-saturated nitrogen to eliminate the kinetic limitations imposed by the low N_2 solubility and its low diffusion rate in aqueous solutions. Typically, (photo)electrochemical cells can be divided into single-chamber (Fig. 13d) and dual-chamber cells (H-type cell) (Fig. 13e and f). The first reported electrochemical reactors used single-chamber cells together with solid electrolytes (*e.g.* solid oxides with good proton or ion conductivity) under H_2 atmosphere, and operated at high temperature and ambient pressure.[300]

In non-solid single-PEC cell systems, both oxidation and reduction reactions take place in the same cell. As a result, re-oxidation of NH_3 products on the anode is likely to be detrimental to the NH_3 performance. Therefore, as in other PEC reactions, separating the cathode and anode into two divided chambers is an effective way to correct these deficiencies and increase the NRR performance. This type of reactor is known as double-chamber cell or H-cell in the literature. Generally, H-cells are in the form of consist on an H-shaped apparatus separated by a proton exchange membrane (PEM) or an anion exchange membrane (AEM). During the electrochemical reaction, the protons or hydroxide ions produced at the anode move through the membrane to the cathode to participate in the NRR under mild catalytic conditions. On the other hand, most of the NH_3 produced (NH_4^+ in aqueous solutions) cannot cross these membranes, thus avoiding the re-oxidation and the loss of efficiency of single-chamber cells. That is why it is essential to select suitable membranes that minimize the NH_3/NH_4^+ crossover, allowing the total concentration of NH_3 in both chambers' electrolytes, as a portion of the products can be still transferred through the membrane to the anodic chamber. Furthermore, this anti-crossing effect allows the use of two different electrolytes. This additional degree of freedom can lead to even more optimized reaction conditions by electrolytes combinations. For instance, Kim *et al.*[301] reported a bio-electrolyte system using LiCl/ethylenediamine (EDA) as catholyte and H_2SO_4 solution as anolyte. Regarding membranes, they have a fundamental role in the performance of such cells. The most commonly used cation exchange membrane (CEM) so far in H-cell testing is Nafion 212, which leads to a significant NH_4^+ crossover, limiting its suitability. Alternative membranes have been examined, including AEM and porous polypropylene (PP) membranes; the AEMs showed minimal NH_4^+ crossing, while the PP porous membrane exhibited high NH_4^+ crossing. The AEM PiperION-A80 is particularly promising as it shows negligible NH_4^+ crossover in acidic and neutral electrolytes, making it suitable for experiments with H-cell electrolyzers, generating NH_3 under these conditions. However, it is permeable to NH_3 in basic electrolytes (pH 13), thus restricting its selective suitability depending on the electrolyte environment.[302]

5.4. Photothermocatalytic-NRR

The photothermal NRR route is based on the synergistic combination of the photo- and thermo-chemical contributions of sunlight (*i.e.* light and heat). This approach allows for a more effective harvesting of the solar spectrum through the potential absorption of photons in the UV-visible-infrared range.[303,304] Light absorption at catalytic active sites (*i.e.* absorber) causes an increase of the local temperature at the nanoscale, which has the potential to render higher reaction rates. The local heating of the absorber can be maximized by using supports with low thermal conductivity (*e.g.* strontium titanate, silicon, *etc.*), due to their slower heat dissipation losses.[305] This section summarizes the most relevant advances on the photothermocatalytic N_2 reduction to ammonia (Table 3), covering active catalysts and reactor configurations.

5.4.1. Active materials and surface reactivity. In 2018, Zhang and co-workers[312] reported the synthesis of solar ammonia from N_2 and H_2 using a K/Ru/$TiO_{2-x}H_x$ catalyst, using sunlight as the only energy input and without the need of external heating (a 300 W Xe lamp was adjusted to maintain the reactor at 360 °C). The catalyst consisted on a disordered $TiO_{2-x}H_x$ electron-rich support with abundant OVs, modified with K-promoted Ru nanocrystals with localized surface plasmon resonance (LSPR) effect. This system was able to absorb

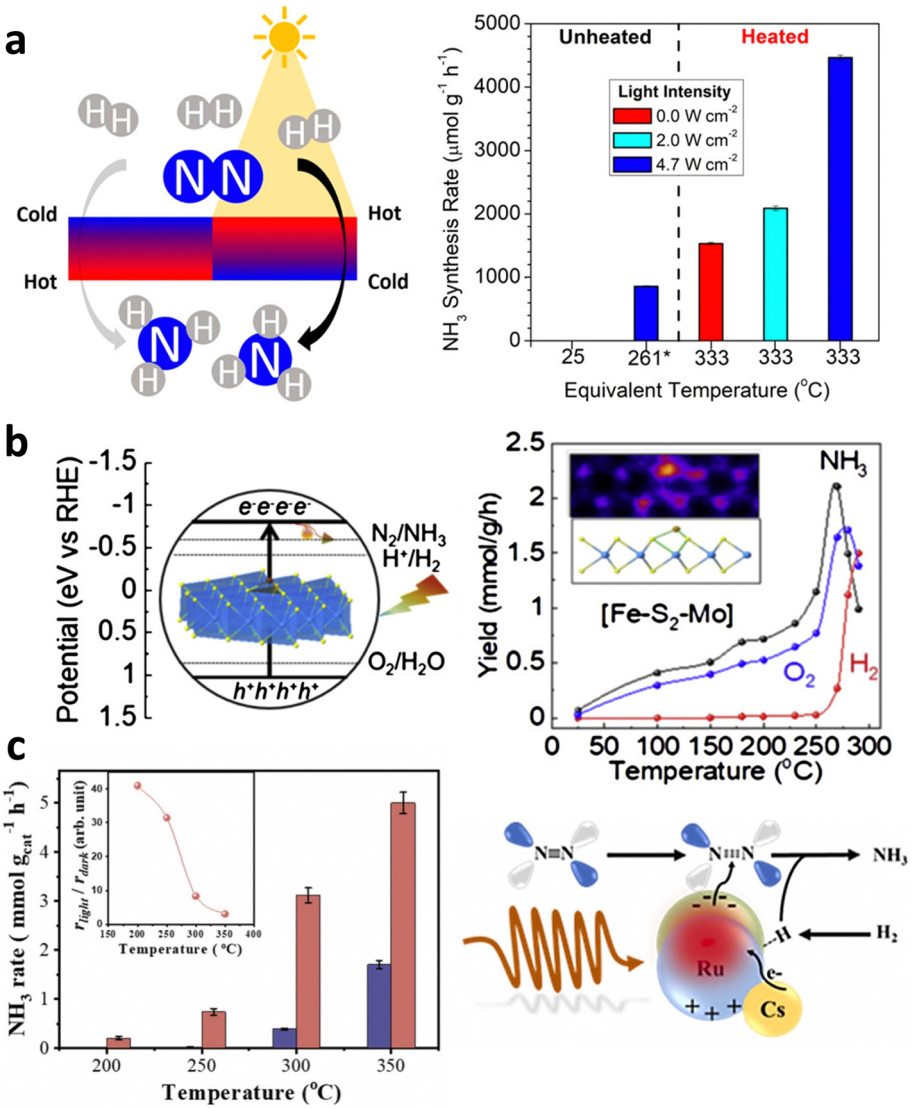

Fig. 14 (a) Thermal gradients created and controlled by photothermal heating of Ru–Cs/MgO catalyst, and associated plasmonic photothermal NH_3 production rates under dark and illuminated conditions (blue LED). Reprinted from ref. 307 Copyright 2019 ACS. (b) Schematic energy diagram of Fe–MoS_2, and production rates of NH_3, H_2, and O_2 as a function of temperature. Dark experiments are shown as empty symbols. Reprinted from ref. 309 Copyright 2021 Elsevier. (c) Temperature dependence of NH_3 production rates with CsRu@ZrO_2 under dark (blue) and light illumination (red). Inset: Performance enhancement under illumination. Reprinted from ref. 306 Copyright 2023 Elsevier.

UV-vis-NIR radiation and generate local hot spots (~190 °C) on Ru. As a result, K/Ru/$TiO_{2-x}H_x$ delivered a NH_3 generation rate of 112.6 μmol h^{-1} g^{-1} under atmospheric pressure, which was about twice than that obtained in thermal catalysis at the same temperature without solar light irradiation. Interestingly, the activity of K/Ru/$TiO_{2-x}H_x$ lasted longer under photothermal conditions than under thermal catalysis (*ca.* around 7 and 4 h, respectively), and it could be recovered by switching off the light after 7 h, in contrast to thermal catalysis in which deactivation did not revert. The authors explained the high reactivity of K/Ru/$TiO_{2-x}H_x$ in terms of a more efficient N_2 activation by Ru NPs mediated by the electron-rich $TiO_{2-x}H_x$ support. In brief, the interfacial $TiO_{2-x}H_x$ donates electrons to Ru NPs and accepts H atoms from Ru, avoiding H_2 poisoning on the metal. Then, N_2 activation proceeds due to the electron donation of $TiO_{2-x}H_x$ to activated N_2, forming Ti–NH_x (x = 1–3) species even at room temperature.

In 2019, Li *et al.*[307] reported a photothermal plasmonic system based on a cesium-promoted ruthenium NPs supported on magnesium oxide (Ru–Cs/MgO). The authors found that the creation of light-induced controlled thermal gradients in an illuminated packed catalyst bed, by photothermal effect, improved NH_3 reaction rates without external heating and working under atmospheric pressure. They demonstrated that photothermal heating created a negative thermal gradient in the catalyst bed, in which a hot top region accelerated nitrogen cleavage, while generated NH_3 was moved to the cold bottom region of the catalyst bed due to thermophoretic forces, thus

preventing NH_3 decomposition (Fig. 14a). The authors defined an equivalent catalyst temperature assuming the formation of a linear temperature gradient from the top to the bottom of the isothermal catalyst bed. They obtained a NH_3 reaction rate of 858 μmol h^{-1} g^{-1} under concentrated blue LED illumination (455 nm, 4.7 W cm^{-2}) as sole energy source at an equivalent catalyst temperature of 261 °C. They obtained a NH_3 production of 1.5 mmol h^{-1} g^{-1} under dark thermal conditions (333 °C by supplying external heating), while the production rate increased up to 4.5 mmol h^{-1} g^{-1} by combining LED illumination and external heating, due to the creation of a strong negative thermal gradient. Mao *et al.*[39] also explored a dual-temperature-zone ammonia synthesis, using $TiO_{2-x}H_y$/Fe nanocomposites upon solar illumination (10.2 W cm^{-2}). The authors spatially separated a local hot zone (Fe) to dissociate N_2 *via* photogenerated hot electrons, and a local cold zone ($TiO_{2-x}H_y$) for hydrogenation of spilled-over N from Fe. The plasmonic local heating effect of Fe raised the catalyst surface temperature up to 495 °C, with a local temperature gradient of 137 °C between hot and cold zones. Under these conditions, the authors reported η_{STA} values of 3.9×10^{-4}% and 9.2×10^{-3}% at 1 atm and 10 atm, respectively.

Zheng *et al.*[309] prepared a Fe–MoS_2 catalyst mimicking the FeMoCo structure by locating Fe on a single molecular layer of MoS_2. These authors achieved an ammonia production rate of 2.1 mmol h^{-1} g^{-1} with water and UV illumination (70 W tungsten lamp), reaching a remarkable STA of 0.24% at 270 °C. They observed an increase in ammonia selectivity at 180 °C, whereas it dramatically decreased at temperatures over 250 °C due to the competition with the HER. Further, Fe–MoS_2 was tested in a solar furnace to mimic the solar illumination, reaching reaction rates of 17 mmol h^{-1} g^{-1} at 6 bar (Fig. 14b).

In 2022, Wang *et al.*[311] reported the photothermal hydrogenation of N_2 over Ni/TiO_2 catalysts, achieving a NH_3 production rate of 0.2 mmol h^{-1} g^{-1} at 400 °C and under illumination with a 300 W solar simulator. The authors found that the oxygen vacancies on TiO_2 photocatalytically activated N_2 and trapped photoelectrons, while Ni atoms thermocatalytically dissociated H_2 and hosted the holes, finally resulting in the photothermal N_2 hydrogenation to ammonia. Recently, Peng *et al.*[305] reported the hydrogenation of N_2 to NH_3 under visible-NIR illumination using Cs-decorated strontium titanate-supported Ru nanoparticles. They achieved 3345 μmol h^{-1} g^{-1} at 350 °C and near 1 Sun power illumination, with a slight decay of activity during a continuous 120 h reaction. They found that NIR illumination was more efficient than visible-light wavelengths to activate N_2, due to a greater generation of hot electrons and local heating at Ru NPs. In contrast, UV light did not contribute to NH_3 production. Besides, they inferred that the partially reduced Cs promoter transferred electrons to Ru sites, contributing to the formation of oxy-azide-related species that were sequentially hydrogenated to NH_3. Very recently, these authors reported a N_2 hydrogenation catalyst based on highly dispersed Cs-decorated Ru sub-nanometric clusters (ratio Ru/Cs = 6) supported on ZrO_2 NPs (Fig. 14c).[306] This material achieved 1.6 $mmol_{NH_3}$ h^{-1} g^{-1} in the dark (350 °C, 0.1 MPa), which increased up to 5.1 mmol h^{-1} g^{-1} under 1 sun power illumination with a remarkable extended stability for 100 h irradiation under continuous flow. They found the role of Cs species in increasing the basicity of the ZrO_2 support, and donating electron density to the adjacent Ru sites that favored a pre-activation of the adsorbed N_2. Also in the last year, Bian *et al.*[308] published a strategy for determining the actual reaction temperature in photothermal catalysts, identifying and independently quantifying the contributions of hot electrons and local heating effects on photothermal catalysis on the basis of Le Chatelier's principle. They studied the photothermal ammonia synthesis over a carbon-supported Ru catalyst, in which they found that hot electrons generated by Ru reduced the activation energy of N_2 fixation with respect to thermal catalysis (54.9 *vs.* 126.0 kJ mol^{-1}), and simultaneously protected the carbon support from methanation. This effect provided the catalyst with high stability during an operation time of 1000 h, while under thermal conditions the material deactivated before 150 h on stream. They estimated a hot electron contribution of 73.6% under their experimental conditions (350 °C, 5.3 W cm^{-2}).

5.4.2. Reactor engineering. In general, photothermocatalytic NRR tests are conducted in gas-phase reactors, frequently fixed bed reactors, which may operate either continuously or in batch mode. The most common configurations are reactors equipped with quartz windows for illumination,[223] fixed-bed tubular reactors,[311] solar furnaces without any electrical heating system,[309] or other specific configurations for the creation of thermal gradients inside the catalyst bed.[307] The catalyst is usually immobilized on fixed supports (*e.g.* quartz or glass fibre filters), or it can be loaded into the catalyst bed as powder, pellets or spheres. The temperature of the catalyst is usually monitored with thermocouples or thermometers.[310,312] Experiments are conducted under a constant gas flow, with molar or volumetric $H_2:N_2$ ratio of 70%:30% or a mixture of N_2 and H_2O, at a mildly elevated temperature (<450 °C).

In photothermal reactors, heat can be generated *via* (i) light irradiation, (ii) external heating or (iii) coupling both illumination and external heating. (i) In the absence of external heating, thermal energy is generated by the conversion of incident photons to heat (phonons) over the catalyst surface. In this case, heat generated from light can completely replace the external heating source or reduce the temperature required for the reaction.[304] In general, the heating effect provided by a light source may vary from 110–160 °C depending on different factors, such as the type of light source, light intensity, or distance to the catalyst surface.[313] (ii) In contrast, heat can be supplied externally by using electrical furnaces, heating ribbons and heating plates. External heating is usually employed either when the catalyst cannot generate enough heat by light absorption, or to provide a constant heating for the progression of the chemical reaction. However, in this case, NRR reaction may proceed mostly *via* thermal catalysis and therefore, the process should be referred as "photo-assisted".[313] Lastly, the outlet product stream is generally directed to acid traps (*e.g.*

0.05 M H_2SO_4, 0.1 M HCl) for subsequent analysis by colorimetry or ionic chromatography.

6. NRR analysis

6.1. Detection methods

Ammonia is a small, polar molecule with basic character (*i.e.* it accepts protons from water) and a high solubility in aqueous phase (482 g L^{-1} at 24 °C),[22,314] compared to the gases that can be found in the reaction media (*e.g.* N_2, O_2 and H_2), which are less soluble (specially H_2) and easily determined by gas chromatography (GC).[22] In contrast, ammonia quantification is usually performed in aqueous solution by different techniques. In liquid phase, ammonia can exist as ammonium ion (NH_4^+) or un-ionized ammonia (NH_3) depending on the pH and the temperature of the reaction media. In general, the fraction of NH_3 increases as the pH or temperature of the solution increases, and the equilibrium fully shifts to gas-phase ammonia for pH higher than 11 (eqn (2), Section 2).[22,37] Therefore, alkaline aqueous solutions may contain gaseous ammonia both in the head space and in the liquid phase as dissolved gas. This complicates the storage of the samples for quantitative analysis, which is preferred to be done immediately after sampling.[37] The current methods for the detection and quantification of ammonia include colorimetric assays, ion chromatography (IC), fluorescence, ion-selective electrodes, ^{15}N-labeled N_2, ^{1}H nuclear magnetic resonance (^{1}H NMR) spectroscopy, and Fourier-transform infrared spectroscopy.[30,315]

At a glance, colorimetric assays are the most commonly employed methods due to their low cost and easy application.[30] However, the method should be carefully chosen depending on the particular reaction conditions. For instance, Nessler's reagent method works well in both alkaline and acidic solutions, the indophenol blue method is suitable in alkaline media, whereas IC works best with acidic solutions. Besides, certain sacrificial agents are not compatible with the cation chromatography columns, which can limit the application of IC.[31] Experimental data also reveal that Nessler's reagent method and IC are preferred for aqueous ammonia quantification over a wide concentration range (0–8 mg L^{-1}), whereas the indophenol blue method may overestimate the ammonia concentrations above 500 μg L^{-1}.[316] Further details for each method are given in the following subsections.

6.1.1. Spectrophotometric methods

6.1.1.1. Nessler's reagent method. Nessler's reagent consists of mercury(II) iodide and potassium iodide (K_2HgI_4) and an alkaline solution of sodium hydroxide (NaOH) or potassium hydroxide (KOH). Iodide and mercury ions react with ammonia under alkaline conditions to produce a reddish-brown complex, which exhibits strong absorbance at 420 nm (eqn (8)).

$$2[HgI_4]^{2-} + NH_3 + 3OH^- \rightarrow Hg_2ONH_2I\downarrow + 7I^- + 2H_2O \quad (8)$$

This absorbance is directly proportional to the NH_4^+ concentration in the absence of interferants, such as metal cations (except sodium and potassium), hydrazine, carbonyl compounds, *etc.*[31,316] The high alkalinity of the Nessler's reagent can cause the precipitation of metal hydroxides, creating turbidity that interferes with colorimetric analyses. Zinc sulfate and sodium hydroxide solutions can be added to clarify turbid samples.[22] Besides, Rochelle salt ($KNaC_4H_4O_6 \times 4H_2O$) is often added during the analysis to minimize possible interferences from other ions (Fe^{3+}, Co^{2+}, Ni^{2+}, Cr^{3+}, Ag^+, S^{2-}, *etc.*) in solution and to prevent the formation of cloudy samples.[31,316] Ammonia is quantified colorimetrically at wavelengths between 380 and 550 nm.

It should be noted that mercury ions in Nessler's reagent are toxic and thus the reagent should be handled and disposed carefully; Nessler's reagent solution must be prepared using ultrapure water; the lifetime of Nessler's reagent is relatively short (around three weeks); the quantification of NH_3 should be performed with a reaction time from 10 to 30 min to avoid degradation and erroneous results.[316]

6.1.1.2. Indophenol blue method. The indophenol blue method is based on the Berthelot reaction (eqn (13)), and involves the reaction of ammonia with phenol and hypochlorite under alkaline conditions to generate a blue-colored indophenol product. Blue colored indophenol is formed from the reaction of ammonia with hypochlorite and phenol in an alkaline medium, following consecutive steps. First, ammonia and hypochlorite react at pH 9.7–11.5 to give monochloramine, which then reacts with phenol to give quinone chloramine that further reacts with phenol to form yellow indophenol. Then, the indophenol dissociates in an alkaline medium to give the blue color (eqn (9)). Sodium nitroprusside is used as a catalyst to intensify the color change in indophenol reaction, and citrate buffer is used to stabilize the pH of the reaction solution and avoid interferences with magnesium and calcium precipitates. Indophenol can be quantitatively determined by colorimetry between 630 and 650 nm.[22,31,316]

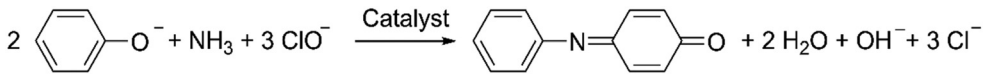

(9)

This method is suitable for the detection of low-concentration ammonia ranging from 0–0.6 mg NH_3–N L^{-1}, and slightly interfered by other species such as organic nitrogen compounds, nitrites or nitrates. Its major drawback is the time-consuming sample preparation.[22,37,317]

6.1.1.3. Salicylate method. This is a modification of the indophenol blue method in which phenol is substituted for sodium salicylate to prevent the formation of *o*-chlorophenol. Therefore, this method is much safer and more stable than the

indophenol blue method. However, it is less sensitive, needing much higher concentration of salicylate for ammonia detection, and reagents are more expensive. In this method ammonia and hypochlorite react to give monochloramine, which forms 5-aminosalicylate with salicylate (eqn (10)). This method gives colors changing from light yellow (excess reagent) to green and then to blue with increasing ammonia concentration. Colorimetric quantification is performed at 640 nm.[22] Some metal ions (*e.g.* Cu^{2+}) can interfere with the analysis, although it can be solved using masking agents.[116]

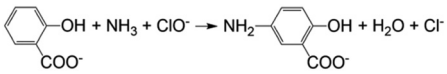

(10)

6.1.2. Ion chromatography. An ion chromatograph (IC) separates ions and polar molecules (mobile phase) based on their affinity to the ion exchanger (stationary phase). Then, ions are detected by a conductivity detector at concentrations ranging from 100 ppb to 80 ppm.[22,318] This method is timing saving, and offers good reproducibility and high sensitivity for NH_4^+ detection covering a wide detection range (0.02–40 mg NH_3–N L^{-1}). Besides, it possesses multiply detector choices (simultaneous detection of multiple components and cations/anions), although it is expensive and requires complex instrumentation. Columns and eluents need to be carefully selected to avoid possible interferences, such as the overlapping of NH_4^+ and Na^+ peaks. Besides, reaction solutions with a strongly acidic/basic character or containing certain organic solvents may be incompatible with the ion exchange columns.[31,116,316,317]

6.1.3. Ion-selective electrodes. An ion-selective electrode (ISE) is a sensor that converts the activity of a specific ion dissolved in solution into an electrical potential.[116] Dissolved ammonia in aqueous solutions ($NH_{3(aq)}$) can be determined using two types of ISE: ammonia gas-sensing electrodes and ammonium ion-selective electrodes. The ammonia gas-sensing electrode consists on a hydrophobic gas-permeable membrane, an internal reference electrode (*e.g.* aqueous solution of ammonium chloride), and a pH-sensing electrode. For the analysis, the pH of the sample is raised to above 11 with a strong base to convert ammonium ions to dissolved ammonia gas. Then, NH_3 diffuses through the membrane changing the pH of the internal solution, which is monitored by the pH electrode and correlated with the concentration of ammonia in the sample solution.[22,116] This method may not be accurate and stable enough for low ammonia concentrations, and sometimes requires to concentrate the solution sample. In contrast, ammonium ion-selective electrodes have a poly(vinyl chloride) (PVC) membrane with an ammonium ion carrier. For the analysis, NH_3 is converted to NH_4^+ through acidification. Then, the electrode potential created across the membrane is measured against an internal reference electrode, and correlated with the concentration of free NH_4^+ in the solution.[22] Ammonium ion-selective electrodes are a rapid method for the detection of ammonia ranging from 0.03–1400 mg NH_3–N L^{-1}, but it has a limited accuracy for concentrations lower than 0.5 mg NH_3–N L^{-1}.[317] In both cases, measurements errors can occur in the presence of high concentration of dissolved ions, especially K^+ for ammonium ion-selective electrodes.[22,116]

6.1.4. Other methods. ^1H nuclear magnetic resonance (^1H NMR) spectroscopy, ^{15}N-labeled N_2, fluorescence, and Fourier-transform infrared spectroscopy (FTIR) have also been used to detect ammonia. Catalytic tests using ^{15}N-labeled N_2 as feedstock followed by ^1H NMR analysis can provide a direct evidence of the real origin of ammonia. When using $^{15}N_2$ as the feeding gas, generated ammonia can only be identified as $^{15}NH_4^+$. ^1H NMR spectra can further confirm the formation of $^{15}NH_4^+$ based on the different chemical shift of triplet coupling of ^{14}N and doublet coupling of ^{15}N.[116] However, it is important to note that $^{15}N_2$ is commonly produced from ^{15}N-labeled ammonia, and therefore it can contain impurities from the manufacturer. To eliminate this interference, N_2 gas should pass through reactive scrubbing solutions before use. ^1H NMR allows for faster sample preparation, but also requires expensive spectrometers to get enough sensitivity levels. Adding 1 mM paramagnetic Gd^{3+} relaxation agent to the NMR solution can reduce by an order of magnitude the analysis time required for quantification, although concentrations above 17 μM NH_4^+ should be reached for an accurate quantitative analysis.[319]

Ammonia can also be detected by fluorescence. This method is based on the reaction of NH_3 with *o*-phthaldialdehyde and sulfite, which produces a strongly fluorescent compound that exhibits maximum excitation and emission wavelengths at 362.5 and 423.0 nm, respectively. This fluorescence is then correlated to the concentration of ammonia in sample solutions, reaching a detection limit up to 1 nmol L^{-1}. Measurement interferences can arise from amines and amino acids in the sample solution.[22] On the other hand, *in situ FTIR* provides useful information about changes in the IR bands during the NRR, such as –H–N–H bending, $-NH_2$ wagging and N–N stretching of adsorbed N_2H_y species.[22,116]

Apart from ammonia, we also note that the product distribution in N_2 fixation can include oxidation products such as NO_x, most frequently nitrates, or partial hydrogenated intermediates such as diazene (N_2H_2) and hydrazine (N_2H_4). Diazene is a highly reactive molecule that has never been spectroscopically detected in solution due to its rapid conversion to N_2H_4 or disproportionation to N_2.[22] In contrast, hydrazine is a common by-product that can be determined by the method invented by Watt and Chrisp.[320] Briefly, a mixture of *para*-(dimethylamino)benzaldehyde, dilute hydrochloric acid and ethanol is used as colour reagent in solutions containing hydrazine, which can be spectrophotometrically detected at 455 nm.

In the case of the analysis of oxidation products, NO_x (NO_2^- and NO_3^-) can be determined by gas or ionic chromatography, although they are rarely reported as by-products in N_2 fixation.[30,321,322] Additional NO_x detection methods include the reduction of nitrate by the cadmium reduction method, which is based on the heterogeneous reduction of NO_3^- with a copperized cadmium column followed by the

spectrophotometric detection of NO_2^- formed.[323] Besides, the formation of nitrites can be analyzed by the Griess assay[324] in which nitrite reacts with sufanilic acid to produce a red–violet colored azo dye ($\lambda_{max} \approx 540$ nm). This is a simple and effective technique for the detection of nitrites in several matrices for concentrations in the range of 0.02 and 2 μM.[325] An additionally recent spectrophotometric method for nitrite detection is based on the reduction of nitrates with UV lamps, which avoids the use of cadmium.[326]

6.2. Performance evaluation

The activity of NRR catalysts can be determined by means of: (i) production rate; (ii) catalyst stability; and (iii) performance metrics (*e.g.* apparent quantum yield (AQY), faradaic efficiency, solar to ammonia yield).

The ammonia production rate represents the amount of ammonia (mol of NH_3 or NH_4^+) produced per unit mass/area of catalyst per unit time, and it is intended to monitor the effectiveness of the catalysts. It can be expressed as μmol h^{-1} g^{-1} for gas- and liquid-phase reactions, μM h^{-1} for liquid-phase reactions, and μmol h^{-1} cm^{-2} for (photo)electrochemical cells.

The apparent quantum yield (AQY) or apparent quantum efficiency (AQE) represents the ratio between the number of electrons participating in the NRR to the total number of incident photons (eqn (11)).

$$\begin{aligned}\text{AQY or AQE}\ (\%) &= \frac{\text{number of reacted electrons}}{\text{number of incident photons}} \times 100 \\ &= \frac{\text{generated ammonia molecules} \times n}{\text{number of incident photons (mol)}} \times 100\end{aligned} \tag{11}$$

where n refers to reacted electrons to form NH_3 and NH_4^+ (*i.e.* $n = 3$ and 6, respectively).

The AQY/AQE should be adopted as a generalized reported parameter to allow the comparison of data acquired under different experimental conditions, such as light source, catalyst loading, reaction time, and illumination area. In general, most materials present low photons to ammonia conversion efficiencies, showing AQY lower than 2.5%,[12] except for a KOH-treated carbon nitride with an outstanding AQE of 21.5%.[225]

The faradaic efficiency (η_F, %) measures the selectivity of the (photo)electrochemical NH_3 production, and refers to the ratio of the current used for N_2 reduction to the total current passed through the circuit (eqn (12)).

$$\eta_F\ (\%) = (xF \times n \times V)/(M \times Q) \tag{12}$$

where x is the number of electrons needed for the formation of NH_3 ($x = 3$); F is the Faraday constant ($F = 96\,485$ C mol^{-1}); n is the measured concentration of NH_3 or NH_4^+ (μg mL^{-1}); V is the volume of the electrolyte (mL); M is the relative molecular mass of NH_3 ($M = 17$ g mol^{-1}); and Q is the total charge passed through the electrodes.[22,327]

The solar-to-ammonia (STA) conversion efficiency is calculated from eqn (13):

$$\text{STA}\ (\%) = \frac{\Delta G_{NH_3}\ (\text{J mol}^{-1}) \times \text{NH}_3\ \text{formed (mol)}}{\text{total incident energy}\ (W) \times \text{reaction time (s)}} \times 100 \tag{13}$$

where ΔG_{NH_3} is the reaction free energy for NH_3 formation ($\Delta G_{NH_3} = 339$ kJ mol^{-1}); the total incident energy is calculated from the overall irradiance (W m^{-2}) and the irradiation area (m^2).

STA efficiencies higher than 0.1% have been reported for graphitic carbon nitride catalysts[328] and ZnCuInS–BiOI heterojunctions[232] without the use of sacrificial agents, while higher STA of 0.24% has been achieved using a photothermal catalyst (Fe–MoS_2) working at 270 °C.[309] Substantial room for improvement exists in order to progress in NRR, which efficiencies are still one order of magnitude lower than that of the photocatalytic water splitting.[12] In this regard, estimations foresee that STA higher than 0.1% need to be reached to compete with Haber–Bosch process for the production of ammonia as a nitrogen fertilizer, whereas STA higher than 20% would be needed for its potential application as a fuel.[30]

The STA efficiency of the (photo)electrochemical processes is not directly measured but can be estimated based on the electrical energy conversion efficiency[329] (eqn (14)):

$$\text{EEC}\ (\%) = \frac{\Delta G_{NH_3} \times \Delta \eta_F}{U_{app} \times F \times n_e} \times 100 \tag{14}$$

where η_F is the faradaic efficiency, U_{app} is the applied voltage, F is Faraday's constant, and n_e is the number of electrons in the reaction.

6.3. Control experiments and interferences

For the evaluation of the NRR performance, one should bear in mind that previous quantification methods are prone to interferences and false-positives at low ammonia yields, which is the case of most reported photoactivities (ranging from nano- to micromolar concentrations). On the one hand, colorimetric methods provide in theory reliable results for simple solutions of ammonia in water.[316] However, certain reaction conditions (*e.g.* changes in solution pH) or the presence of interferants (*e.g.* scavengers, N-containing electrolytes and surface capping agents, solvents, impurity of water, N-ligands) may overestimate the concentration of ammonia due to the formation of colored complexes in the spectrophotometric assays.[30,316] In particular, Nessler's reagent method may lead to false-positives in aqueous solutions containing organic scavengers (*e.g.* methanol, ethanol, isopropanol, triethanolamine, *etc.*) due to the formation of oxidized carbonyl compounds (formaldehyde, acetaldehyde, and acetone) that severely affect the color development. The presence of some metal ions (Fe^{2+}, Ni^{2+}, Ru^{3+}, In^{3+}) in acidic solutions can also interfere with ammonia detection due to the formation of colored complexes. Additional interferences may arise from nanoparticulated precipitates formed in old Nessler solutions.

Further inconsistencies may arise when using certain capping agents (*e.g.* oleyl amine, thioacetamide, hexamethylenetetramine) because they easily decompose into ammonia and other products under light irradiation. Nafion, frequently used in N_2 (photo)electroreduction experiments (as separating membrane or electrolyte), may accumulate and release NH_4^+ through ion exchange with acid groups. N-containing photo(electro)catalysts are also susceptible to decomposition or contain potential ammonia or amine surface groups (*e.g.* NH_x species on the surface of g-C_3N_4) that may lead to inaccurate ammonia yields. Accordingly, a thorough washing step with ultrapure water is critical to guarantee the removal of ammonia or amine groups adsorbed on the catalyst surface.[31] In this regard, control experiments using isotope-labelled $^{15}N_2$ are essential for N-containing materials, in order to verify that ammonia yields originate from gaseous N_2.[31,330] However, we should note that isotope-labelled $^{15}N_2$ gas usually contains ammonia and $^{15}NO_x$ impurities that may lead to experimental artefacts at low ammonia yields.[315] These impurities are generated as by-products during the fabrication of $^{15}N_2$ *via* the CuO-catalyzed oxidation of $^{15}NH_3$, and can reach $^{15}NO_x$ concentrations as high as 0.1 mol% with respect to $^{15}N_2$.[331] Andersen *et al.*[330] estimated that bubbling $^{15}N_2$ gas with a purity of 99.13% for 28 h at a rate of 10 mL min^{-1} would potentially generate 3600 μg h^{-1} of N-containing impurities, thus overestimating the final ammonia yield. This adventitious contamination in the gas stream can be trapped using acidic aqueous solutions or appropriate adsorbents (see good practices in Section 6.3.1).[315] Additional interferences may arise during the sample preparation and handling due to the ubiquitous character of ammonia. Indeed, NH_3 is highly soluble in water and easily adsorbs on a wide range of surfaces, including common laboratory materials (*e.g.* glassware).[314] This can potentially overestimate the quantification and compromise a reproducible analysis. Another source of contamination may come from ambient air, which contains a non-negligible amount of ammonia (ranging from 0.05–250 ppm), which can affect unclosed reaction systems.[315] In fact, gaseous ammonia has a short ambient lifetime of 12 h to 5 days because of its rapid deposition on surfaces, whereas aerosolized ammonium can last in the atmosphere up to 5–10 days. Therefore, gaseous ammonia always provides a background level of contamination either from gas phase dissolution in open reaction systems or solid surface desorption.[314] An additional contamination may originate from the electrolytes in (photo)electrochemical experiments. Commercial electrolytes such as lithium salts (*e.g.* Li_2CO_3, Li_2SO_4, $LiClO_4$) generally contain trace amounts of NO_3^- and NO_2^- that can lead to false positives.[38] As a general rule, inorganic salts should be subjected to a high-temperature annealing (*e.g.* 800 °C for 4 h under Ar atmosphere[332]) before use to eliminate possible NO_x impurities.

6.3.1. Good practices in NRR experiments. The wide range of possible interferants in NRR experiments highlights the need to verify the formation of ammonia with a double-checked quantification, control tests, and thorough lab practices. Before starting the experiments, the feed-gas should be purified to eliminate any possible N-contamination (*e.g.* ubiquitous NO_x, N_2O and NH_3). This can be done by using (i) commercial gas purifiers, (ii) appropriate adsorbents (*e.g.* reduced copper catalyst and a freeze trap), or (iii) reactive scrubbing solutions.[103,315] Acidic solutions (*e.g.* 0.05 M H_2SO_4) are effective for ammonia removal in the inlet gases, before entering the reactor, but do not trap NO_x species. In contrast, alkaline $KMnO_4$ solutions can also eliminate NO_x in the gas streams, and are thus a more effective scrubber option.[333] Then, the purity of the feeding gas (Ar, $^{14}N_2$, $^{15}N_2$) should be quantitatively checked by gas chromatography or NO_x analyzers, equipped with a gas separation column to avoid interferences in the NO_x signals by the presence of hydrocarbons.[331] At the outlet of gas-phase reaction systems, acid traps can be used to absorb ammonia (as NH_4^+) even at low concentrations. However, we note that the use of strong acid solutions could lead to the degradation of the Nessler reagent during colorimetric analysis.

On the other hand, N-impurities on the catalyst surface (NO_x, NH_4^+) can be removed by pre-reduction of the materials before experiments.[103] The reaction system should be cleaned between uses by boiling in ultra-pure water and subsequent drying in oven.[103] The use of catalysts precursors that contain nitrogen (*e.g.* urea, amino compounds or nitrate/nitrite salts) usually lead to residual N contents that can lead to the formation of ammonia under illumination or reductive conditions.[334] Some active catalysts, especially those based in amino and nitride groups, present nitrogen in its composition, making necessary to determine the nitrogen balance, by comparing the N produced in reaction and the N content from the catalyst (*e.g.* by elemental analysis). A especial care should be taken with some synthesis methods that can promote the incorporation of N species on the catalyst surface,[335] and which can react giving false positives.

Then, catalytic experiments should start with background measurements of NH_3/NH_4^+ and NO_x in control tests. For instance, experiments under inert atmosphere (*e.g.* Argon/Helium) should be carried out under the same experimental conditions as the NRR tests, in order to quantify any possible amounts of adventitious ammonia or NO_x coming from the catalyst surface or the reaction system. Photoelectrocatalytic experiments would require control tests under argon, with and without potential applied, and control tests under N_2 at open circuit potential over the same duration. In all cases, ammonia yields should be considered reliable if substantially exceed those obtained in control tests.[315,330,331]

Detection of N-contamination should be addressed with improved gas-scrubbing or through appropriate catalyst pre-treatment. Ammonia production should be confirmed by more than one quantification technique, always including precise detection methods such as IC or ^1H NMR. In this regard, a recent comparative study[315] on ammonia quantification methodologies found that almost all testing methods showed poor reproducible results for ammonia concentrations below 0.2 ppm. Indeed, they found detection errors of 20.5% with Nessler's reagent method and 71.2% with IC for the analysis of

a standard NH_3 solution (0.1 ppm), thus raising strong concerns about the reliable quantification of low ammonia concentrations. Therefore, the use of ^{15}N isotopically labeled control experiments is highly recommended to verify the origin of products and exclude false-positives. The amount of $^{15}NH_3$ produced in the experiments should agree with the amount of $^{14}NH_3$ produced in the control tests with $^{14}N_2$ under equivalent conditions, keeping a 1 : 1 ratio.[330] Moreover, the formation of $^{15}NH_3$ can be further cross-checked by using a combination of $^{15}N_2$ and ^1H NMR experiments. However, we note that this approach requires a complete protonation of ammonia in order to observe a clear ammonium triplet for $^{14}N_2$ and doublet for $^{15}N_2$, which is not always well controlled. Besides, one should bear in mind that ammonium protons rapidly exchange in reaction solution, and consequently, ^1H NMR measurements can suffer from interferences if the deuterated solvent contains any labile deuterium, thus leading to uncontrolled levels of hydrogen/deuterium exchange. For that reason, the use of more stable solvents such as DMSO-d6 and $CDCl_3$ is preferred.[331]

6.4. Proposed standardization of experimental devices and parameters

NRR field is growing rapidly, as reflected by the increasing number of publications of the different NRR technologies every year (Fig. 1). However, reported ammonia productions are strongly affected by false positives and experimental artifacts that overestimate the catalyst performance. The reason behind these issues is the lack of standards for benchmarking performance. A general agreement on standardized protocols and performance metrics would greatly facilitate the comparison of reported data, essential to progress on the development of this technology. In fact, the creation of a global network of research institutions sharing NRR testing could facilitate the development of meaningful techno-economic life cycle analysis (LCA) and socio-economic studies, which are crucial for profitability analyses. Besides, considering the growing rate of this research field, the prompt adoption of a common set of operating conditions would avoid to reach a high volume of overestimated and non-comparable data, as happened before for CO_2 reduction reaction.[336] Reference NRR experiments could be performed using the agreed set of operation conditions and commercial catalysts for a reliable global comparison. These experiments also call for benchmark reactors, due to the common use of home-made lab-scale reactors that limit a rapid and accurate comparison of experimental results. Finally, reported data should always include efficiency metrics (such as AQY, STA efficiency and/or faradaic efficiency) to guarantee reproducibility and to pursue good practices for a real development of the technology. Standardization of experimental procedures and performance metrics could be in line with the successful qualification test protocols for photovoltaics pioneered at the National Renewable Energy Laboratory (NREL). This would clearly impact on a high data reliability for technology transfer, hopefully paving the way to the development of NRR demonstrators, pilot plants and ultimately solar ammonia refineries. Fig. 15 depicts a flow chart protocol with the abovementioned suggested experimental practices.

7. Uses of ammonia and future opportunities

7.1. Versatile properties of ammonia for wide-range applications

Ammonia is a colourless gas with a sharp and penetrating odour. The NH_3 molecule has a trigonal pyramidal shape with three hydrogen atoms and an unshared pair of electrons attached to the nitrogen atom. It is a polar molecule with strong intermolecular hydrogen bonding. Its boiling point is 239.8 K, its freezing point 195.5 K and its density 0.73 kg m^{-3}. Ammonia has an auto-ignition temperature of 930 K (compared to methane, 859 K) under atmospheric conditions, an octane number of $\sim$130 and a high heat of vaporization (1371 kJ kg^{-1} compared to $\sim$271 kJ kg^{-1} of gasoline). The combustion of ammonia is challenging due to its low reactivity, although it can release energy yielding only water and nitrogen as by-products ($4NH_3 + 3O_2 \rightarrow 2N_2 + 6H_2O$ + heat), with a stoichiometric air fuel ratio (AFR) of 6.06 by weight.[18] Due to its low reactivity, the hazards derived from accidental combustion or explosions are low compared to other fuels. In this regard, anhydrous ammonia is non-flammable while ammonia vapour in air is flammable and may explode when ignited. In the event of leaks, ammonia is very soluble in water and may be corrosive due to a rapid increase in pH to 11.6. Besides, ammonia spills generally form a dense aerosol cloud after evaporation, which rapidly dilutes since it is lighter than air. Dry, warm and windy weather diffuses ammonia to the atmosphere faster than humid, cold and low wind conditions.[18] For that reason, guidelines recommend to include a refuge point upwind from the point of storage/use of ammonia in large scale facilities.[18]

Regarding health hazards, ammonia is toxic for humans and most invertebrates. The degree of toxicity mainly depends on the concentration and the time of exposure. However, it is not carcinogenic and can be easily detected by odour at very low concentrations (5–25 ppm). At low concentrations in air (50 ppm to 100 ppm), ammonia may irritate tissue surfaces such as eyes, respiratory system and skin, while the inhalation of higher concentrations rapidly produces suffocation and may cause respiratory burn injuries or even death. Human exposure limits range between 25 and 50 ppm, with severe health consequences for concentrations above 300 ppm.[18,337] Main properties are summarized below in Table 4.

7.2. Current and potential end-uses of renewable ammonia

Nowadays, around 85% of the overall ammonia production is destined to the fertilizer industry (*i.e.* urea, ammonium nitrate, ammonium sulphate, diammonium phosphate (DAP) or dry ammonia). Around 15% production is used as synthesis platform of multitude of everyday products (chemicals, plastics, textiles, pharmaceuticals, refrigerants, abatement of nitrogen oxides (NO_x), *etc.*). For instance, the textile industry uses

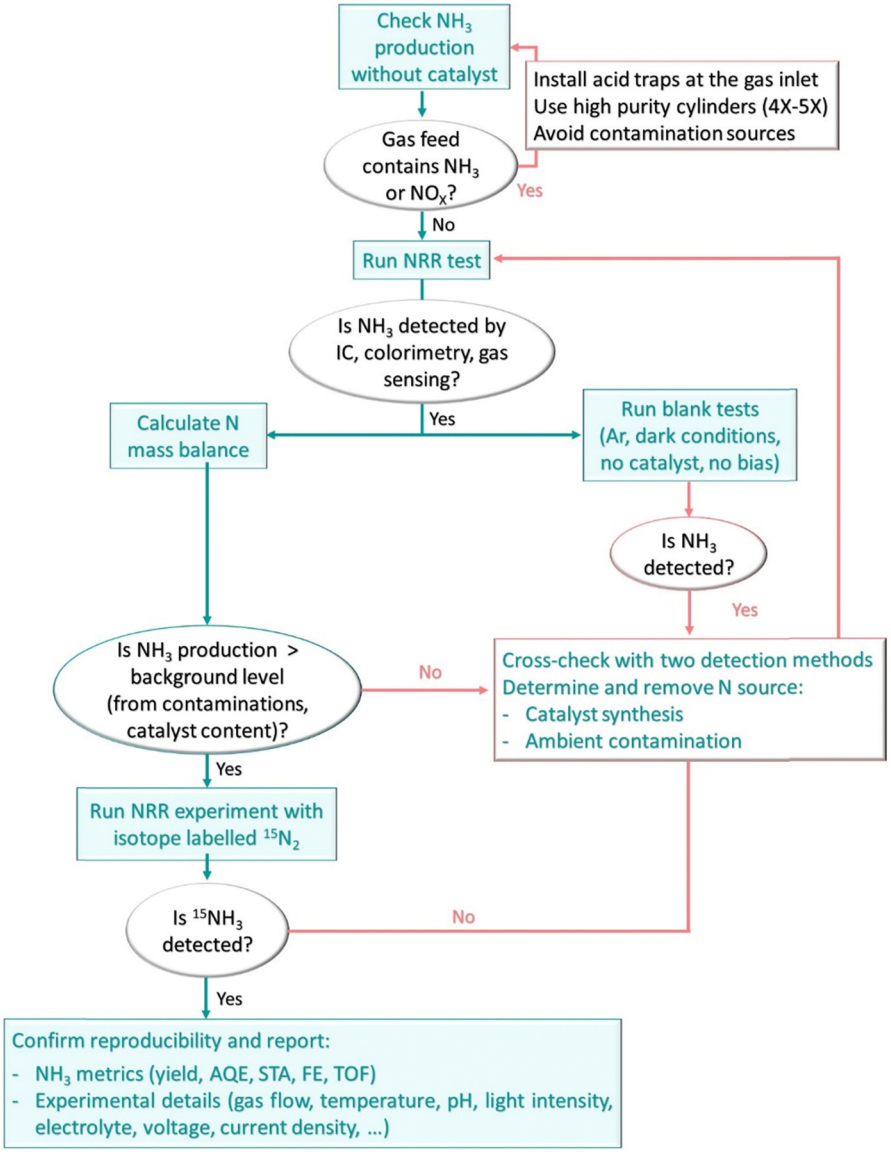

Fig. 15 Suggested protocol for benchmarking light-driven NRR experiments.

ammonia for softening cotton and for the production of synthetic fibers (such as nylon and rayon). Ammonia is also used for the production of explosives, such as ammonium nitrate (NH_4NO_3) or antibacterial drugs.[339] Its unique properties and wide application (Fig. 16) explain why it is considered one of the seven basic chemicals, alongside ethylene, propylene, methanol and BTX aromatics (benzene, toluene and xylene).[27] More recently, ammonia produced from renewables (<1%) has risen attention as an attractive candidate to replace fossil fuels in relevant sectors such as electric power generation and maritime transport, as well as for the storage and delivery of hydrogen in the move towards a low-carbon economy. The key advantage of NH_3 is that it contains 40% more hydrogen (17.75 wt%) than methanol (12.6 wt%), and can be produced from renewable hydrogen and nitrogen from air, without any carbon-species for the synthesis.[340] Thus, ammonia has the potential to be a major contributor to the clean energy transition in the context of "Power-to-X" technologies, in which sustainable fuels are synthesized from excess power. For instance, in countries with excess power from non-intermittent low-carbon energy sources (*e.g.* nuclear), ammonia could provide stable exports of energy to other markets; while in countries with intermittent energy resources (*e.g.* renewables), ammonia could store the excess generation, dealing with the seasonal variability and balancing the energy system.[339] Besides, ammonia could offer decentralized sources of green energy to remote locations with difficult access to energy supply. Below are listed the most promising applications of this carbon-free energy vector.

7.2.1. Ammonia for energy storage. Seasonal fluctuations in energy demand peaks are important in many countries and usually addressed through conventional energy storage in fossil

Table 4 General properties of ammonia (data collected from ref. 337,338)

CAS number	7664-41-7
Physical state	Liquid
Color	Colorless
Odor threshold	5–25 ppm
Molar weight	17.03 g mol^{-1}
pK_a	9.25
Molecular structure	Symmetrical pyramid, N at apex
	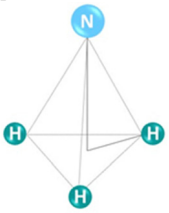
H–N–H bond angle	106.67°
N–H length	1.1024 Å
Dipole moment	1.47 debye
Boiling point	239.8 K
Melting point	195 K
Freezing point	195.5 K
Critical temperature	406.4 K
Auto-ignition temperature	930 K[a]
Density	0.73 kg m^{-3}
Vapor pressure	10 atm (at 298.7 K)
Thermal conductivity (gas)	2.45×10^{-4} J cm^{-1} s^{-1} K^{-1} (at 299.7 K)
Refractive index (liq)	1.325 (at 289.5 K)
Dielectric constant (liq)	16.9 (at 298 K)
Octane number	~130
Heat of vaporization (at 1 bar)	1.37 MJ kg[b]
Latent heat of evaporation	1.37 kJ g^{-1}
Dielectric constant	22 (at 239.2 K)[c]
Ionization potential	10.2 eV
Energy content	18.8 MJ kg^{-1} (LHV)[d]
Ideal gas properties (298 K, 1 atm)	
Specific heat (C_p)	35.65 J K^{-1} mol^{-1}
Standard entropy	192.77 J K^{-1} mol^{-1}
Standard enthalpy of formation	−45.89 kJ mol^{-1}
Free energy of formation	−16.37 kJ mol^{-1}
Equilibrium constant (log K_f)	2.87
Standard enthalpy of formation (gas at 298 K)	−46.22 kJ mol^{-1}
Standard entropy of evaporation	87.75 J K^{-1} mol^{-1}
Standard entropy of fusion	28.93 J K^{-1} mol^{-1}
Latent heat of fusion	0.33 kJ g^{-1}
Heat of solution in water	2.18 kJ $g_{NH_3(gas)}^{-1}$
Solubility in water	51–53 $g_{NH_3(gas)}$/100 mL
Flammability limits of ammonia in air	16–25%
Flammability limits of ammonia in oxygen	15–79%
Auto ignition temperature	924 K
Hazard statements	H221-Flammable gas H280-Contains gas under pressure; may explode if heated H314-Causes severe skin burns H318-Serious eye damage irritation H331-Toxic if inhaled H400, H411-Very toxic to the aquatic environment with long lasting effects

[a] Compared to 859 K for methane under atmospheric conditions. [b] Compared to ~271 kJ kg^{-1} for gasoline. [c] Compared to 81 for water at 298.2 K. [d] Compared to 120 MJ kg^{-1} for hydrogen.

fuels (*e.g.* natural gas).[339] A long-term large-scale energy storage enables the distribution of excess energy, mitigating both seasonal variability and unpredictable disturbances.[341] This is particularly crucial in renewable-based energy systems, in which peak demand does not always coincide with peak renewable generation and therefore, a significant excess capacity is needed to meet peak demand. Besides, clean energy resources may not be necessarily close to demand centres, and power interconnections over long distances are often expensive and technically difficult. In this context, power generation and consumption could potentially be connected through zero-carbon energy storage, which includes hydrogen or carbon-neutral hydrogen derivatives (*e.g.* ammonia). This approach could be achieved in high power superconductors (storage over extremely short periods of time, *i.e.* seconds), batteries (minutes-days), pumped hydroelectricity (days-months) or

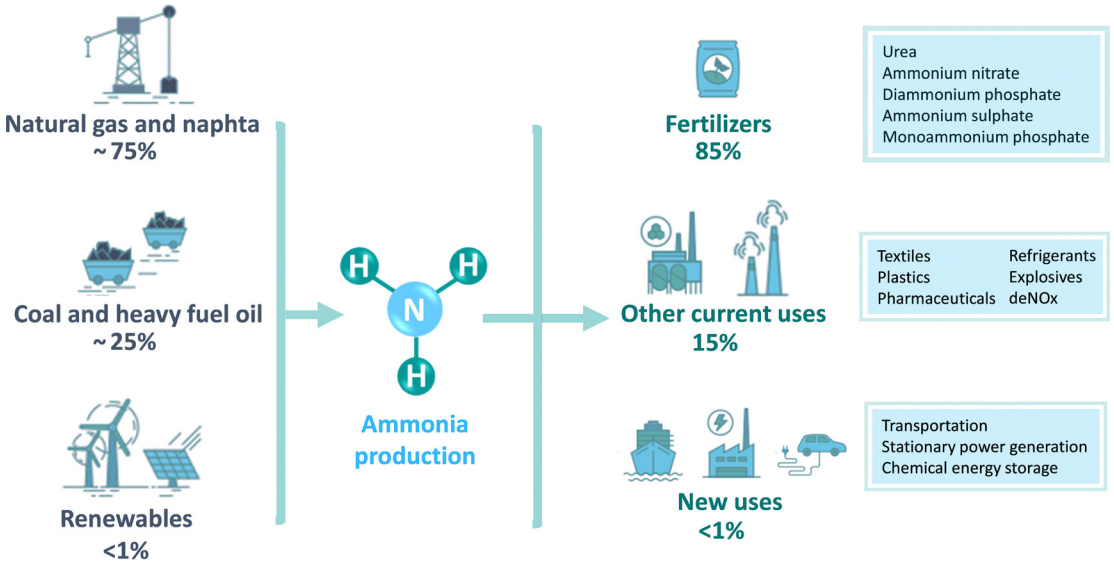

Fig. 16 Current and potential uses of ammonia. Adapted from ref. 27.

chemicals (over months) (Table 5). Among them, zero-carbon chemical storage is the most flexible approach for the storage of large quantities of energy over long time periods at any location, in many cases even using the existing infrastructure.[18,24,339] In contrast, other applications suffer from important limitations such as the geological constraints of the pumped hydro or the insufficient capacity of lithium batteries for grid-scale energy storage.[18] Even more, the cost of chemical storage per kW h is significantly lower than that of the most long-lasting batteries, even despite their gradually decreasing production cost (see technoeconomic comparison in Section 8).[339] In this context, ammonia is today viewed as the most advantageous option to address the challenge of long-term large-scale energy storage, providing a practical and clean alternative to fossil fuels. To store in bulk, ammonia requires liquefaction either by compression to 10 bar or chilling to −33 °C, while hydrogen in comparison needs to be compressed to around 350 to 700 bar, or cryogenically cooled to −253 °C for large-scale storage.[24] Under these conditions, ammonia has a high volumetric (121 kg_{H_2} m^{-3} at 10 bar) and gravimetric (17.8 wt%) hydrogen densities, and an overall energy density of about 3 kW h L^{-1}, which is comparable to some fossil fuels.[24,342] Besides, it can be stored in cheap plastic tanks and distributed using the conventional infrastructure such as the current liquefied petroleum gas (LPG) network or the existing shipping infrastructure.[24]

7.2.2. Ammonia for transportation. Ammonia produced from renewables has the potential to be a viable liquid fuel replacement for many daily applications of fossil fuels, such as shipping bunker fuel, diesel substitute in transportation, and even as a potential jet fuel. As a great advantage, ammonia can be distributed similarly to fossil fuels using the existing and well-developed shipping and pipeline transfer infrastructure. Using NH_3 as a dual fuel in marine engines could lower total greenhouse gas emissions up to 33.5% per ton kilometre.[341]

The current technology for maritime propulsion consists on the two-stroke engine, which could be adapted to use ammonia as a fuel, with an energy efficiency of *ca.* 45–50% on a lower heating value (LHV) basis.[27] MAN Energy Solutions (Research Center Copenhagen) is currently thoroughly testing a two-stroke engine for large-scale container ships, operating on 100% ammonia fuel by 2025.[343] Moreover, the technology group Wärtsilä is leading a powerful consortium of shipping stakeholders to develop demonstrators for two-stroke and 10 MW four-stroke marine engines running on ammonia fuel.[344] Four-stroke engines for marine applications are believed to be able to reach energy efficiencies around 50% on LHV basis.[27] Further developments for maritime propulsion are also focused on ammonia-fed solid oxide fuel cells (SOFC) with potentially higher energy efficiency (*ca.* 55–60% on LHV basis).[27] A few examples of ammonia-fuelled vehicles have been achieved so far, such as the implementation of an ammonia-fed engine in the Toyota GT86-R Marangoni sports car led by Bigas International;[345] or the development of an ammonia-gasoline dual fuel prototype vehicle in the South Korean Institute for Energy Research (KIER), which uses a fuel ratio of 70% ammonia to 30% gasoline to power a spark ignition engine.[345] The application of ammonia in internal combustion engines greatly benefits from the absence of SO_x or particulate emissions, and their limited N_2O/NO_x emissions in comparison to heavy oils.

7.2.3. Ammonia for stationary power generation. Once ammonia has been produced, stored and distributed, it can be directly used for power generation or heat release with zero-carbon footprint at its point of use. The International Renewable Energy Agency (IRENA) estimates that ammonia will largely contribute to electricity generation by around 2030, by 50–60% co-firing with natural gas in gas turbines and with coal in coal-fired power plants.[27] This approach represents a potential early option to reduce CO_2 emissions in existing coal-fired power plants.[346] As an example, successful 20%

Table 5 Current available energy storage solutions. Adapted from ref. 339

	Technology	Energy density (W h L^{-1})	Maximum storage capacity (GW h)	Maximum storage duration	Advantages	Disadvantages
Electrical	Supercapacitors	2–10	0.0001	Seconds–minutes	Easy storage and distribution high round-trip efficiency (90–94%)	Low energy density Low storage capacity High costs per installed density
Electrochemical	Li-ion batteries	200–350	0.5 (for stationary module systems)	Hours–days	Medium energy density high efficiency (95%) long lifetime transportable	High cost Complex management systems
Mechanical	Pumped hydro	0.3–1.5	3 (potentially 14)	Days–months	Long storage time Medium efficiency (75–82%)	Low energy density Limited storage (constrained by geography) and distribution large-scale units for economically feasible applications
Chemical	Natural gas	10.1 6200 (LNG)	1260 (underground caverns)	Weeks–months	High energy density	Expensive electrolysers
	Hydrogen	2400 (liquid)	0.13 (tanks) 124–167 (underground caverns)		Large storage capacity Long storage time	Low efficiency Natural gas (30–35%)
	Ammonia Steam reforming (liquid)	3194–4325	0.25 (cooling tanks) 300 (underground caverns)		Low energy installation costs	Hydrogen (30–60%) Ammonia-steam reforming (20–25%) Ammonia-electrolysis (40–72%) High power installation costs

ammonia co-firing tests were achieved by JERA in a 1 GW coal-fired power plant in 2021.[347] Further, IRENA has even foreseen 100% ammonia firing by 2040 in both baseload and peaker plants, using gas turbines, furnaces, engines and fuel cells; and also replace diesel in off-grid applications using fuel cells.[27] Proton-conducting fuel cells (PCFCs), alkaline- (AFC) and solid oxide- (SOFC) fuel cells can be used for power generation from ammonia, with relatively low cost and less flammability risk than other fuels.[341] The high operating temperature of SOFC (above 200 °C) enables the direct use of ammonia without any pre-treatment opposite to low temperature fuel cells, such as proton-exchange membrane- (PEMFC) and phosphoric acid- (PAFC) fuel cells, which have poor tolerance to ammonia (<0.1 ppm) due to the acidic nature of the electrolyte.[340] The main advantage of the direct utilization of ammonia is the increased efficiency, since it does not require decomposition into hydrogen and subsequent purification.[348] Ammonia can also replace carbon-based fuels (natural gas, gasoline, diesel) in internal combustion engines and gas turbines, although it needs engine modifications to improve ammonia combustion due to its poor ignition quality, low burning velocity and narrow flammability limits (15–25% air).[348] These limitations can be minimized by blending ammonia with a more reactive fuel (*e.g.* hydrogen, methanol, *etc.*) to improve ignition quality and flame stability. The presence of unburnt NH_3 in the exhaust gases is a hazard, and can be prevented by either using a reburn zone or a selective catalytic reduction to combine NH_3 and NO_x into N_2 and H_2O. The NO_x emissions produced during the ammonia combustion can be mitigated by operating at slightly oxygen lean conditions.[348]

7.3. Decarbonization scenarios

Fossil-based ammonia production routes emit around 2.0 t_{CO_2} $t_{NH_3}^{-1}$ on average. About two-third of the CO_2 emissions come from the generation of hydrogen through hydrocarbon reforming, while a third originates from fuel combustion for ammonia synthesis (about 7.2–9.0 GJ $t_{NH_3}^{-1}$).[23] The significant carbon footprint of conventional routes has triggered researchers to look for an urgent decarbonization of the process, based on three key criteria: energy efficiency, scalability/modularity, and CO_2-free emissions.[314] As a result, three possible scenarios with five overlapping technology generations have emerged, in which synthetic ammonia is classified by colors depending on the production route as: brown, grey, blue, turquoise or green ammonia (Fig. 17).

Ammonia produced from fossil fuels is labelled as brown when hydrogen supply comes from coal gasification, or grey when it comes from natural gas reforming. Both categories correspond to conventional synthetic routes and emit between 2.5–3.8 t_{CO_2} $t_{NH_3}^{-1}$ and 1.6 t_{CO_2} $t_{NH_3}^{-1}$ for brown and grey ammonia, respectively.[24,207,349,350] Blue ammonia uses the same feedstock as brown and grey ammonia, but includes CO_2 sequestration, while turquoise ammonia uses pyrolysis to convert methane into pure carbon and hydrogen, which is reacted with nitrogen to make NH_3. This first approach, also known as Generation 1 (Gen 1) scenario, would avoid more

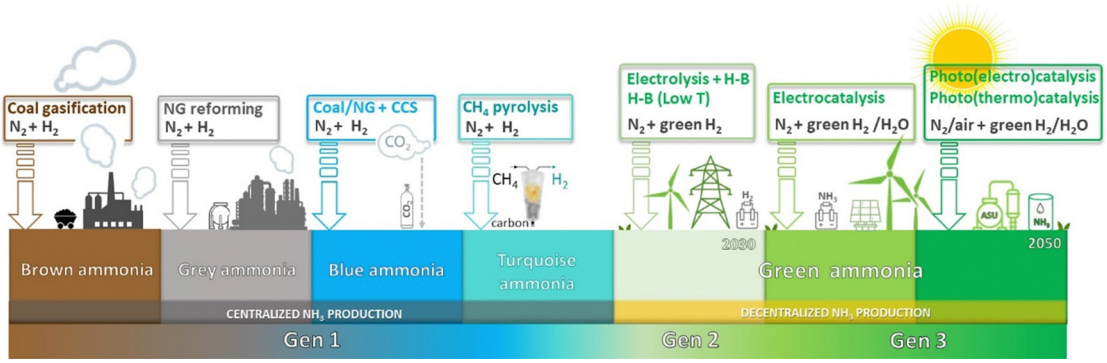

Fig. 17 Classification of synthetic ammonia scenarios based on the energy source and production technology.

than 90% CO_2 emissions generated by conventional routes, and would even bring the net carbon impact of the ammonia production to zero by supplying green hydrogen to the H–B process. Generation 2 (Gen 2) refers to ammonia produced in a modified small-scale H–B process using renewable sourced hydrogen from water electrolysis; and finally, Generation 3 (Gen 3) refers to the production of green ammonia by alternative synthetic routes using renewable electricity (electrochemical) or sunlight (photochemical), without the participation of the H–B process.[350,351] The term "green" implies that the hydrogen is generated from water electrolysis without releasing carbon emissions on combustion and the nitrogen is extracted from air through an air separation unit, using renewable electricity (*e.g.* biomass, solar, wind, hydro, geothermal), meanwhile the reaction is driven at ambient temperature and pressure.[24,207,349,350]

Synthetic ammonia based on the previous approaches is currently going from pure academic research to pilot-scale plants. Some of the most relevant advances include: shipments of blue ammonia (40 tonnes) for power generation from Saudi Arabia to Japan in 2020, where ammonia imports for power generation are expected to reach 0.5–1 Mt year^{-1} in 2025, 3–5 Mt year^{-1} in 2030 and 30 Mt year^{-1} in 2050;[27] industrial developments to produce green ammonia *via* water electrolysis (Proton Ventures, Morris, Hy2gen, ACME group, NFUEL®, Fertiberia, Stamicarbon, Topsoe, Yara, BASF, Kapsom, Casale, Thyssenkrupp, Siemens, *etc.*);[26,27] Pilot plant testing of ammonia fueled SOFCs (1 kW class power) by IHI cooperation;[207] A feasibility study on a 900 MW hydro-based renewable power plant (Sarawak, Malaysia) conducted by South Korea's Samsung Engineering for the production of green hydrogen (7000 t year^{-1}) and green/blue ammonia (> 600 000 t year^{-1}), amongst others, expected to end before 2027;[352] another pre-feasibility study of a hydrogen project for blue ammonia production (1 million t year^{-1}) in the Northern Territory (Australia), completed in 2022;[353] as well as near future blue/green ammonia plants, which include a 20 million m^3-per-day blue hydrogen and ammonia production plant in Louisiana (operations expected to start in 2026),[354] and a green ammonia production facility (100 000–200 000 t year^{-1}) in Jordan, which will include a 530 MW solar farm, an energy storage facility, electrolyzers of unspecified capacity, and a water desalination plant.[355]

All these initiatives highlight the unique opportunities offered by ammonia to achieve a global zero carbon transition, within the concept of Power-to-X (P2X) technologies, based on long-term renewable energy storage into carbon-neutral synthetic fuels, which can then be used in other sectors or stored until needed.

7.4. Recent advances towards a solar ammonia refinery

Current decarbonization plans are putting the focus on the development of green ammonia production technologies at sufficient industrial-scale for the new green economic model. The possibility of producing ammonia from just N_2/air, H_2O and sunlight is a great challenge for our solar fuels' community. On this pathway towards a solar ammonia refinery, there are currently two main lines of thinking: (i) the one that supports the storage of renewable electricity as chemical energy only when there is an excess of electricity that otherwise would be wasted; and (ii) the one that believes on a future solar-to-

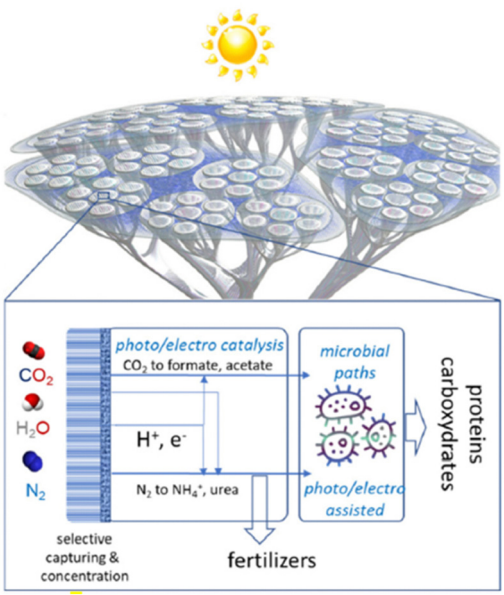

Fig. 18 Schematic representation of an artificial-tree for the local generation of solar fuels and chemicals. Reproduced with permission from Centi *et al.*[356]

chemicals (S2C) industry, even if it entails long-term research and developments.[16] In the second approach, Centi and Perathoner recently suggested the possibility of fabricating artificial tree-like devices to produce fuels and chemicals from N_2, CO_2 and H_2O at the consumer level, which would act as small solar fuels industries (Fig. 18).[356]

These artificial trees would consist on the combination of "leaves", representing photoelectrocatalytic devices, along with the "branches and trunk" that would act as distribution/collection elements. This *in situ* solar-based chemical industries would have greater adaptability to different applications, increased resilience, very low carbon footprint, lower time-to-market, and reduced economic costs and environmental impact, mainly associated with avoided transportation. In a nearer-term scenario, technological developments are working on turning the solar ammonia refinery in a real concept. At present, great efforts are directed at replacing or re-configuring H–B plants with CO_2 capture as a short-term solution, while mid-to-long-term scenarios foresee a large-scale green ammonia production from water, air and solar energy, which could be extended to the production of fertilizer derivatives. The latter option is still constrained by the cost of electricity/energy and the current low ammonia yields (mmol h^{-1} g^{-1} range).[357] Both factors impose limitations for the industrial scale up of the technology, which needs for a breakthrough in the areas of materials science, reactor/cell engineering, and the use of artificial intelligence and robotization. Following this concept, over 20 renewable and low-carbon ammonia European projects have been announced to start in 2030, gathering partnerships between different ammonia and fertilizer manufacturers and hydrogen suppliers, such as Yara, Fertiberia, Iberdrola, Hyperion, Siemens, Orsted, *etc.*[358] The world's first green ammonia plant was developed by Kapsom, a global leader in sustainable energy solutions, in 2020. The facility is located in Northeastern India and uses solar power to produce more than 1500 t $year^{-1}$ of green ammonia.[359] The same year, the Australian Renewable Energy Agency (ARENA) supported a feasibility study for the installation of a solar refinery in the Pilbara region of Western Australia.[360] The so-called Yuri Renewable Hydrogen to Ammonia Project is led by Yara Pilbara Fertilisers Pty Ltd (Yara), an important wide word fertilizer company, and ENGIE, a global leader in low-carbon energy and services. The project started in 2022 with the support of ARENA, ENGINE and Mitsui & Co. Ltd (Mitsui), and is expected to finish in 2028. This would be one of the world's first industrial-scale green ammonia plants using off-grid intermittent renewable H_2 *via* electrolysis. In particular, this project will develop a 10 MW electrolyzer powered by 18 MW of solar PV, and will be supported by an 8 MW battery energy storage system. In 2022, the Spanish fertilizer producer Fertiberia inaugurated the first green ammonia plant in Spain (Puertollano), within the Green H2F project,[361] in partnership with Iberdrola and

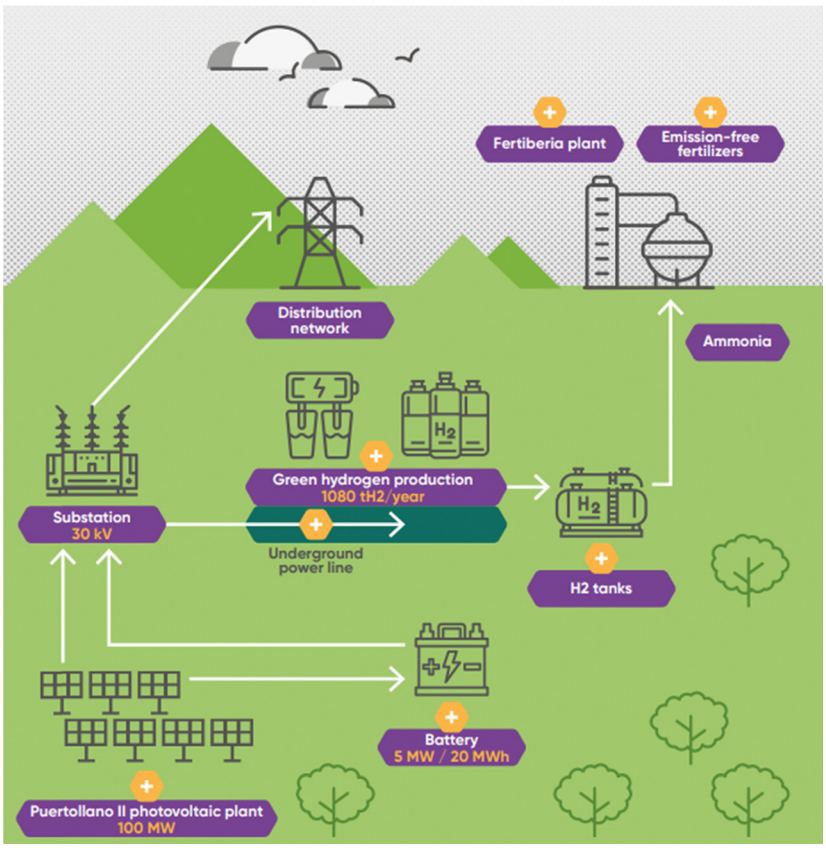

Fig. 19 Schematics of Puertollano ammonia plant. Source: Iberdrola.

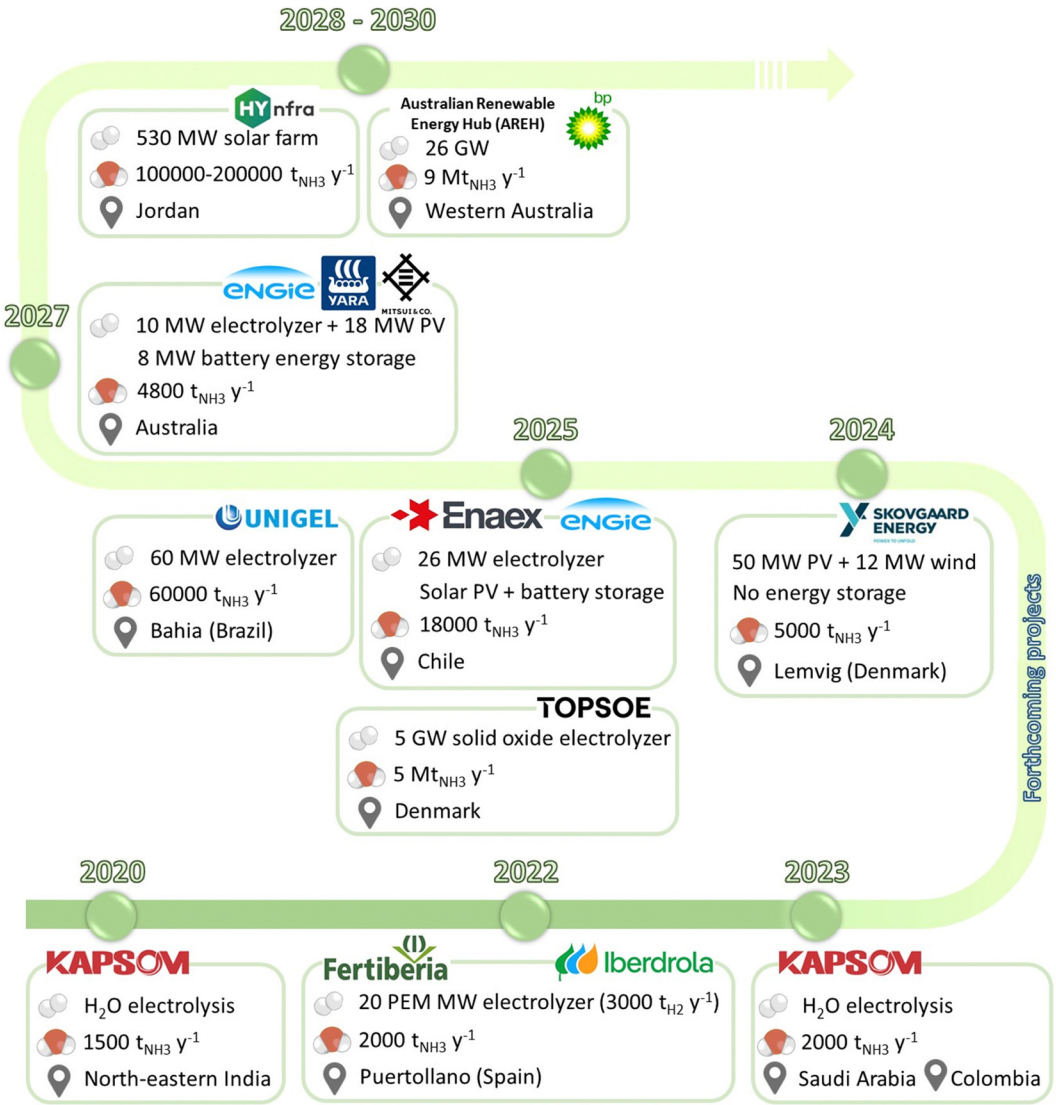

Fig. 20 Timeline of operational and forthcoming green ammonia projects worldwide.

with the technical support of Spain's National Hydrogen Center. This plant (Fig. 19) includes a 100 MW PV facility that powers a 20 PEM MW electrolyzer with a capacity of 3000 t_{H_2} $year^{-1}$ (*i.e.* 360 kg_{H_2} h^{-1}). The solar intermittency is addressed by battery electrochemical storage (5 MW/20 MW h lithium-ion battery) and hydrogen storage (6000 kg capacity), which is enough to feed the H–B plant during low solar irradiation hours. The surplus of electricity generation is used to refill the storage systems or is exported to the grid.[358] Moreover, a second phase with up to 800 MW of additional capacity is already under development through 2027.[361]

Very recently, Fertiberia has joined Cepsa as a strategic partner to develop a 1-GW electrolysis project in Palos de la Frontera (Spain), as part of the Andalusian green hydrogen valley.[362] Green hydrogen production will start in 2026, and it will be consumed by Cepsa and Fertiberia for the manufacture of advanced biofuels, ammonia, AdBlue and sustainable crop nutrition solutions. Another very recent project (2023) is the first green ammonia plant developed by Kapsom in Colombia.[363] This project has an annual NH_3 output of 2000 t $year^{-1}$, and will significantly reduce CO_2 emissions during the production process if compared to the traditional coal-based or natural gas-based ammonia synthesis (6400 t_{CO_2} and 3600 t_{CO_2}, respectively). Additional forthcoming projects for green ammonia production are summarized in Fig. 20.

8 Techno-economic comparison of ammonia production technologies

8.1. Ammonia production in conventional Haber–Bosch plants

The earth's population growth increases at a constant ratio, demanding for a continuous production of fertilizers alongside an increasing energy and electricity consumption (Fig. 21a). About 80% of the total ammonia production *via* Haber–Bosch

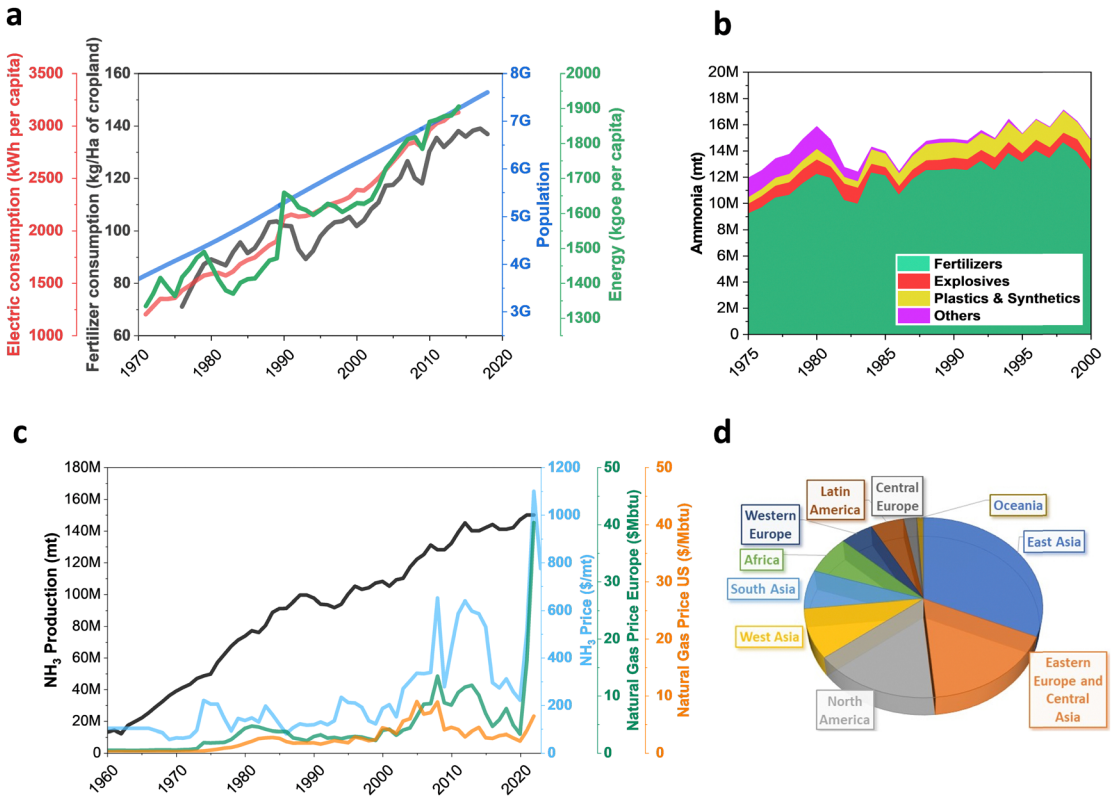

Fig. 21 (a) Temporal evolution of world population (blue line), fertilizer consumption (grey) and electricity/energy consumption (red/green) in the period 1970–2020 (data extracted from the World Bank[366]); (b) end uses of ammonia (USGS);[367] (c) evolution of the global ammonia production (USGS[368,369]), and price evolution of ammonia (USGS) and natural gas in USA and Europe (World Bank[370]); (d) distribution of the global fertilizer production capacity in 2021 by region.[371]

(H–B) process is converted into nitrogen-rich fertilizers (Fig. 21b). Among them, ammonium nitrate is mainly used in the European Union, urea is more frequently used in China and Bharat (India), while USA commonly injects ammonia directly into soil (10–20 cm below surface to prevent losses by volatilization).[103,162,364,365]

The energy-intensive H–B process has experienced significant technological improvements over the past 20th century, reducing the energy consumption from 40–100 GJ $t_{NH_3}^{-1}$ to 28–32 GJ $t_{NH_3}^{-1}$ in actual single-train ammonia plants[207,211] with the best available techniques implemented. Today, H–B technology consumes around 1% of the world energy production[372] to reach ammonia generation capacities of more than 3000 t d^{-1}. The highest energy consumption in current ammonia production plants comes from natural gas reformers and CO_2 removal systems. However, steam methane reforming (SMR) (72%) is nowadays considered the best available technique (BAT) for ammonia synthesis, given its higher energy efficiency and lower carbon emissions compared to others such as coal gasification (22%, 56–64 GJ $t_{NH_3}^{-1}$), naphta (1%) or partial oxidation of heavy oil (4%). Coal gasification and heavy oil partial oxidation consumes much more energy (1.3 and 1.7 times more energy, respectively)[19] and release more CO_2 (*ca.* 6 t_{CO_2} $t_{NH_3}^{-1}$) than methane reforming (*ca.* 1.6 t_{CO_2} $t_{NH_3}^{-1}$).[208,373,374] As a result, the ammonia production industry emits 500 Mt $year^{-1}$, which represents 1% of the global CO_2 emissions.[372] Coupling H–B plants with carbon capture technologies (CCS) can considerably reduce the amount of CO_2 emissions to 0.2–0.4 t of CO_2 per t of NH_3.[375,376] Additional recent improvements include the development of energy recovery systems with more efficient designs, new catalysts, adsorbent/absorbent enhanced H–B processes, new converter designs, and electrochemical H–B process.[377]

Regarding costs, the global ammonia production has been historically influenced by the evolution of the natural gas price (Fig. 21c), suffering important fluctuations during economic/energy crisis periods, especially in importing regions such as the European Union. In particular, the recent disruptions in the global economy as a consequence of the 2020–2021 pandemic, and the rise in natural gas prices as a consequence of the Russia–Ukraine conflict led to a circumstantial increase in ammonia prices, which varied from less than \$\$300 $t_{NH_3}^{-1}$ to more than \$1600 $t_{NH_3}^{-1}$ in 2022.[378] This price rising was worsened by the increase in transportation costs, among other factors, which disrupted the supply chains. The fertilizer prices have fallen 71% in 2023 due to a decrease in the natural gas prices and the adaptation of markets to the new geopolitical scenario.[379] Despite that, ammonia prices are still high compared to historical standards, and the risk of appreciation remains constant following the same instability previously

observed during the oil (1973) and financial (2008) crisis. Today, ammonia production is one of the most important markets worldwide, accounting for $80 billion per year.[29] The current production system is based on a centralized generation mainly ruled by the biggest fertilizer manufacturers (China, India, Russia and USA) (Fig. 21d). These countries produce cheaper ammonia due to the lower costs in natural gas, achieving ammonia production costs around ~$160 $t_{NH_3}^{-1}$ in large H–B plants (>2000 t_{NH_3} d^{-1}), although costs can be doubled small plants (<100 t_{NH_3} d^{-1}).[380,381] In contrast, ammonia producers in other countries are unable to produce at less than $500 t_{NH_3}.[382] We note that the production costs of ammonia in large H–B plants may further increase due to storage and transportation, eventually reaching market prices around $600 $t_{NH_3}^{-1}$.[383] However, the long-distance transportation of ammonia by pipeline is more efficient than that of H_2 and natural gas, making the transportation and storage of ammonia much more economic.[384] Transportation of anhydrous ammonia by pipeline is economically viable for connecting ammonia plants with fertilizer production facilities located in market areas. In contrast, shipping is adequate for large volumes and exportations with good terminal costs and infrastructure. Transport by rail is suitable for moderate ammonia productions, while transport by truck is relatively expensive although flexible to reach isolated areas at short distances.[385] In general, the main factor determining the selection of the transportation media is the distance to the agricultural land. For instance, the costs of transportation reported for a specific case varied from $0.0153, $0.0161, $0.0215 to $0.0365 t^{-1} km^{-1} for pipelines, ships, rail tankers and trucks, respectively.[329] Additional costs may arise from the storage of pressurized/refrigerated anhydrous ammonia for its stational selling (75%) during the planting season.[386] Besides, the total ammonia cost may considerably increase considering the social costs as externality.[380]

8.2. Green ammonia with H–B synthesis loop

The traditional H–B synthesis loop could enable the production of green ammonia by (i) fully electrifying the process with renewable energy, (ii) decoupling H_2 production by methane steam reforming, or (iii) using renewable hydrogen as feedstock.[164] In this regard, H_2 can be obtained from other fossil-free sources, for instance, through biomass gasification (syngas), biomass reforming (biogas from anaerobic digestion), or renewable water electrolysis.[387] Indeed, early ammonia production plants in 1920's already integrated H_2 produced by electrolysis in regions with hydroelectric power generation. Afterwards, the lower cost of natural gas made methane reforming more competitive, thus outcompeting other H_2 production processes.[15] Nowadays, decarbonization scenarios estimate that green hydrogen will contribute to more than half of the total ammonia production in 2050 (>550 Mt $year^{-1}$).[27,388] In particular, Saygin *et al.*[374] estimate an increase in 1100 GW electrolyzer capacity and 2300 GW of renewable generation capacity to supply 5500 TW h $year^{-1}$ of electricity (from the actual 29 000[389]–30 000 TW h[390]).

8.2.1. Hydrogen from biomass. Today, biomass conversion (pyrolysis, gasification, anaerobic digestion) in industrialized countries contributes to 9–13% to the total energy supplies.[391] However, H_2 production from biomass feedstock is a thermodynamically ineffective process, which is still not competitive with conventional fossil technologies (*e.g.* 5–50% efficiency of H_2 production by biomass gasification compared to 69–85% of steam reforming[392]). Regarding costs, H_2 prices may vary between $1.28 kg^{-1} (for SMR) to $7.05 kg^{-1} for renewable-based technologies, in which the performance is still 7–8 times lower.[375,393–395] However, the latter may compete with centralized methane reforming when the prices of natural gas are high. For instance, H_2 production from biomass gasification could contribute to reach average ammonia production costs of 386–$2300 $t_{NH_3}^{-1}$ depending on the production scale.[396] In fact, ammonia plants with production scales over 1000 t_{NH_3} d^{-1} are considered competitive, with production costs close to $500 $t_{NH_3}^{-1}$ and CO_2 emissions (0.3–0.84 t_{CO_2} $t_{NH_3}^{-1}$) below those generated in conventional plants (2.0 t_{CO_2} $t_{NH_3}^{-1}$).[396]

Table 6 collects relevant data from reported technoeconomic studies on ammonia production using H_2 from biomass conversion.

8.2.2. Hydrogen from electrolysis (E/H–B). Other hybrid process for ammonia synthesis consists on integrating green H_2 production from water electrolysis into the H–B loop, thus replacing SMR. This technology requires renewable energy supply, land accessibility, water accessibility (9 tons of water are necessary for the production of 1 ton of hydrogen[20]), water desalination units, water electrolysis units, ammonia synthesis reactors, and ammonia storage and transport infrastructure.[349]

Large-scale green ammonia production with electrolysis requires around 30–36 GJ t^{-1} of electricity,[207,401] although the potential to reduce these values is still high.[164] Around 80–90% of this energy consumption is used for H_2 production

Table 6 Technoeconomic studies on green ammonia synthesis using biomass as H_2 source

H_2 source	Plant capacity (tpd or t $year^{-1}$*)	CO_2 emissions (kg_{CO_2} $kg_{NH_3}^{-1}$)	NH_3 cost** ($ t^{-1})	Ref.
Biomass pyrolysis and gasification	14–384 (pyrolysis) 10–1022 (gasification)	—	570–1369 (pyrolysis) 488–1519 (gasification)	384
Biomass gasification	1200	0.5–0.88	386	397
Biomass, biogas, wind	2000–28 000*	—	680–2300	398
Biomass gasification	700	—	750–1200	399
Biomass gasification	1187	0.3	968	400
Biomass gasification	65–200	0.59–0.84	1153 (65 t) 740 (1200 t)	396

(50–55 kW h kgH_2^{-1}), while the remaining energy is used for air separation, gas compression and synthesis loop.[374] Cryogenic air separation at large scale (> 600 t_{N_2} day^{-1}) also accounts for approximately 25% total cost of a whole H–B plant, ranging between \$0.03–0.05 $kg_{N_2}^{-1}$.[250] The CO_2 emissions derived from E/H–B are very low, between 0.12 to 1.3 t_{CO_2} tNH_3^{-1}, which is far below other technologies such as SMR or coal gasification.[164] Life cycle analyses of conventional and renewable ammonia production routes showed that obtaining N_2 from cryogenic distillation and H_2 from electrolysis reduce GHG emissions by 91% compared to conventional SMR plants.[402] However, the most challenging drawbacks of this approach are the current cost and the intermittency of renewable electricity, which requires the dynamic operation of electrolyzers and H–B loops.[375] For instance, power-to-ammonia plants in North Europe become competitive at gas prices of €70 MW h^{-1} and CO_2 emissions prices of €200 $t_{CO_2}^{-1}$.[403] Thus, a decrease in the costs of renewable electricity would substantially make green ammonia synthesis more economically feasible.[404] At present, H_2O electrolyzers are commercially available at a scale larger than 100 MW power per stack.[17,349,405,406] Among several electrolyzer's designs, proton exchange membrane (PEM) electrolyzers are the most competitive with H_2 production costs at \$5–23 kg^{-1}. However, the average costs for SMR are around \$1.28 kg^{-1}.[375,393,407] The costs associated to the electrolysis unit remains expensive (\$1 M per MW), but foreseen technological improvements would reduce costs by half in the mid-term.[408,409] These technological improvements will also need to address current engineering limitations related to the durability of high-temperature electrolyzers (700–900 °C), powered by renewable energy and thus working in intermittent conditions.[15] Other costs associated with the nitrogen separation unit (membranes, Pressure Swing Adsorption, or distillation) should be addressed depending on the production capacity and the required purity.[410]

Further, it should be noted that ammonia production *via* E/H–B strongly depends on the levelized cost of electricity (LCOE) (0.04–0.19 € per kW h[411,412]). In this regard, economic analyses showed the advantage of using Ru-based catalysts in small scale ammonia plants (< 100 t_{NH_3} d^{-1}), where the cost associated with reactors and heat exchangers are dominant compared to the catalyst's cost.[413,414]

Table 7 shows that average green ammonia prices double or triple those of grey ammonia,[375,415] due to the large capital costs of renewable power (LCOE) and electrolyzers.[17,349] In this regard, Salmon and Bañares-Alcántara[349] estimated that 50% reduction in the electrolyzer's capital costs could reduce ammonia costs to \$400 t^{-1}, and this could be achieved by combining wind and solar energy as the power supply.

In the current geopolitical context, high gas prices and low capital costs of electrolyzers could improve the competitiveness of green ammonia.[374] In the meantime, blue ammonia is foreseen as a viable near-future option to replace conventional ammonia production under present-day conditions (*i.e.* 2024), as long as natural gas leakage rates are maintained low. However, this transition scenario will need to face some other important aspects such as the cost of H_2 storage solutions (*e.g.* underground storage), the energy losses in the DC/AC/DC electricity conversions and other processes involved, safety of H_2 transportation and related costs, use of feedstock buffers (*i.e.* oversized electrolyzers for H_2 storage), *etc.*[17,431]

Table 7 Technoeconomic studies on green ammonia synthesis with E/H–B loop

H_2 source	Plant capacity (tpd or t year[a])	CO_2 emissions (kg_{CO_2} kg_{NH3}^{-1})	NH_3 cost[b] (\$ t^{-1})	Ref.
Wind/solar	7–490 (solar) 5–263 (wind)	—	660–2342 (wind) 830–5951 (solar)	384
Wind	48	—	655–720	416
Wind	1202.55	0.97	742	417
Offshore wind	300	—	1566	418
Solar/wind, biogas, anaerobic digestion	0.219	0–3.82	—	387
Wind	109.6	—	526–861 (2023) 431–931 (2030)	419
N.A.	—	—	713–1457	420
Offshore wind	300	0.09–0.478	583–1224	421
Wind	1000	—	273	404
Wind/solar PV	300	—	1350–1380 € t^{-1}	422
Wind/solar PV/hydro	—	—	431–528 € t^{-1}	403
Hydroelectric	200	—	335–380 € t^{-1}	423
Wind/solar	83 220[a]		588 £ (2025–2030)	424
Wind	0.18	—	—	425
Wind, solar	35 000[a]	—	< 500	401
Renewable	20 000[a]	—	798	426
Solar	1840	—	450–718	427
Renewable (2040)	91–2000	—	515–613	380
Wind/solar PV	0.3–2.33	—	391–644	428
Wind (floating offshore ammonia)	300	—	1574–1724	418
Steam turbine	50 000[a]	—	374–670	415
Renewable	11.6		754–815 € t^{-1}	429
Wind, solar	1320–1728	—	842 € t^{-1}	430

[a] t_{NH_3} $year^{-1}$. [b] If not specified (\$ $t_{NH_3}^{-1}$).

The technoeconomic study of Mayer *et al.*[432] concluded that the implementation of green ammonia would require further developments to become an efficient alternative, needing to achieve higher efficiencies for electrolyzers and PV panels (80% and 70%, respectively). In contrast, Cesaro *et al.*[412] made an optimistic estimate of green ammonia price, ranging from \$771 t^{-1} in 2020 to less than \$400 t^{-1} in 2040. Nayak-Luke and Bañares-Alcántara[17] studied the viability of producing islanded green ammonia in 534 locations in 70 countries. The study found that the current islanded ammonia production with renewable energies (wind and solar) is not competitive with conventional fossil fuel plants, founding the production of H_2 (electrolyzer CAPEX and OPEX) as the most significant cost components. However, predictions by 2030 foresee an achievable islanded green levelized cost of ammonia (LCOA) below \$350 t^{-1} in the most favorable locations. We note that the LCOA depends on the cost of air separation, the capital cost per unit area of reactor (\$ m^{-2}), and the STA conversion efficiency.[250] Sagel *et al.*[433] concluded that combined wind and ammonia energy storage system could be competitive with fossil-based alternatives coupled to carbon capture and storage (CCS) in some locations, such as small island developing states (SIDS), although ammonia imports are still the most feasible option at market prices above \$500 $t_{NH_3}^{-1}$.[434] In good agreement with previous works, Fasihi *et al.*[435] estimated the cost of green ammonia with hybrid wind/PV energy production at the most favorable sites of the world, which varied between 440–630 € t^{-1} in 2020, and were predicted to decrease to 345–420, 300–330 and 260–290 € t^{-1} in 2030, 2040 and 2050, respectively. The limitation of this hybrid technology, based on solar panels and wind turbines, is their intermittency and the intense land occupation, which could be solved with off-shore energy generation.[436]

The TRL of electric H–B varies depends on the type of technology, with examples being alkaline (8–9), PEM (6–9) or solid oxide (3–6) electrolysis.[164,437] Several projects have been started and announced during the last years with ammonia production capacities ranging from 1 to 1200 000 t $year^{-1}$. Some companies are developing or announcing green ammonia projects[349,438] like Yara, First Ammonia, BASF, Siemens Energy, Fertiberia, Proton Ventures, Morris, Hy2gen, ACME group, NFUEL®,[439] Stamicarbon, Yara, Kapsom, Casale, Thyssenkrupp, Hygenco, Ammpower, SIP, Haldor Topsoe, CF Industries, Engie & Enaex, AREH, Origin Energy, Origin Energy, NEOM, ACME, Ökowind, EE GmbH, Starfire Energy, ReMo Energy, Greenfield Nitrogen, North Ammonia or nium.

8.3. Green ammonia produced by electrocatalysis

The electrocatalytic production of ammonia is considered the next step towards a low carbon economy transition. Briefly, this technology generates H_2 from water electrolysis, and produces ammonia *via* electrocatalytic N_2 reduction. Three systems have been proposed already: (i) one-step direct electrosynthesis of NH_3 in water,[440] (ii) two-steps electrosynthesis of H_2 and NH_3,[375,440] and (iii) Li-mediated synthesis of NH_3 by Li nitridation.[441] Depending on the reaction temperature, the electrocatalytic ammonia production can be conducted in high temperature solid state reactors (400–750 °C), molten salts and composite membrane reactors (100–500 °C), composite membranes and liquid electrolytes, and solid state electrolyte reactors (ambient-100 °C).[376,442] In general, solid-state synthesis at high temperatures increases the ammonia production rates, although it is restricted by the thermodynamic equilibrium of ammonia formation and the degradation of the materials. On the other hand, the synthesis of ammonia using molten salts usually reaches faradaic efficiencies (FE) below 10% and ammonia formation rates of 10^{-8} mol s^{-1} cm^{-1}.[443] Liquid electrolyte reactors, which use water as the proton source, usually reach FE below 1% and similar ammonia production rates. In contrast, FE as high as 50–60% can be obtained at low temperatures with ammonia formation rates in the order of 10^{-9} mol s^{-1} cm^{-1}.[444–448] Advised values for a potential commercialization of electrocatalytic ammonia are FE of at least 50%, and NH_3 yield higher than 10^{-6} mol s^{-1} cm^{-2}.[449] Regarding the economic viability, a substantial decrease in costs is foreseen when plants are operated at low electricity prices. However, it should be considered that LCOA for electrochemical ammonia synthesis plants is more sensitive to variations in operation factors (LCOE, FE and the current density) than capital costs (electrochemical reactors and electrodes).[440,450]

Hochman *et al.*[380] affirmed that direct electrochemical nitrogen reduction plants could achieve more competitive costs

Table 8 Technoeconomic studies on green ammonia synthesis *via* electrochemical N_2 reduction

H_2 source	Plant capacity (tpd or t $year^{-1}$*)	NH_3 cost** (\$ t^{-1})	Ref.
Wind and solar (2040)	91–2000	423 (2040)	380
Renewable	140	951–969	451
Renewable	0.03	520 (H_2 + N_2) 960 (H_2O + N_2)	440
Renewable	2000	430 (H_2 + N_2) 480 (H_2O + N_2)	440

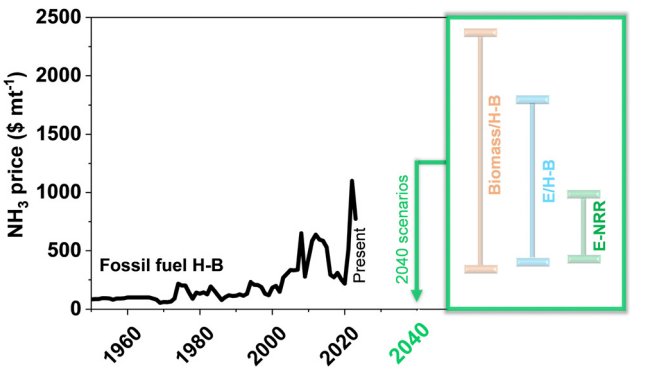

Fig. 22 Historical evolution of ammonia H–B market prices in US (black line),[367–369] and estimation of costs intervals for green ammonia production in three different 2040 scenarios: biomass H–B, electrified H–B (E/H–B), and electrocatalytic NRR (E-NRR). Estimations by 2040 are based on data from ref. 380,412,435

than E/HB technology, with higher FE and overpotential, reaching production costs between \$400–500 t^{-1} by 2040. Other studies even predict that electrocatalytic NH_3 synthesis could be feasible in a fully decentralized ammonia production system at low production scales (<10 t d^{-1}), in locations where natural gas H–B plants or E/H–B plants are not competitive.[380,440] In such locations, a production of 0.03 t_{NH_3} d^{-1} (10 950 kg $year^{-1}$), in a 100 ha farm that requires 100 kg_N ha^{-1} $year^{-1}$ (10 000 kg $year^{-1}$), could be obtained at prices below \$600 t^{-1} under certain predictions (particular LCOE values, FE and current densities).[329,440] Data collected in Table 8 show that electrocatalytic ammonia synthesis could be competitive for low productions in isolate locations, or if the energy input is reduced to 6 MW h $t_{NH_3}{}^{-1}$ with electricity prices below \$0.025 kW^{-1}.[1]

The TRL of direct electrocatalytic ammonia synthesis ranges between 1–5, depending on the operational conditions.[164,452] Some examples of companies currently developing direct electrocatalytic ammonia production are Nitricity, Jupiter ionics, Nitrofix solutions, Liquium, Plasmaleap, Nitrocapt, Atmonia or Nitrofix.

Fig. 22 depicts the historic prices trend for ammonia produced from fossil fuels in the US during the last 60 years, spiking during the periods of crisis, especially during 2020–2023 when prices reached more than \$1100 t^{-1}. The graphic also introduces the production cost ranges for E/H–B, biomass/H–B and electrosynthesis of green ammonia estimated in all the articles reviewed previously. Nowadays these technologies can compete with traditional H–B when the prices of fossil fuels rise. The estimations for 2040 predicted in recent works are in the range of \$300–600 t^{-1} for electric H–B and electrosynthesis.[380,412,435]

8.4. Green ammonia produced *via* photo(electro)catalysis

There is a lack of technoeconomic studies centered on photo(electro)catalytic ammonia synthesis. However, some works highlight the potential of combining photo(electro) catalytic H_2 production with PEC-based electrocatalytic NRR.[450,453] At present, a solar to fuel efficiency of 18% can be obtained using the best solar cells available in the market.[454] Exergoeconomic analyses in large-scale plants calculate hydrogen and ammonia costs of \$3.24 kg^{-1} and \$0.84 kg^{-1}, respectively.[450]

8.5. Green ammonia produced by direct solar photo(thermal)catalysis

One of the main drawbacks of grid-connected technologies for ammonia synthesis is their strong dependency on the LCOE. An interesting alternative to avoid this vulnerability is the direct synthesis of green ammonia by solar photocatalysis. This technology, developed in aqueous or gas-phase, offers the opportunity to completely decentralize the production of fertilizers in remote locations, reducing the dependency on grid-based electricity. Besides, this approach reduces the vulnerability to energy crisis events and brings economic savings, since ammonia can be produced locally at the consumer point avoiding transportation costs. This would also imply more efficient fertilization processes in terms of time, effort and energy consumption. Moreover, aqueous-phase photocatalytic NRR can also reuse side-products from agricultural and industrial activities as sacrificial agents (*e.g.* bioethanol or glycerol), valorizing wasted compounds in the same process, reducing the total organic carbon from aqueous effluents, reducing the management cost of residues, and promoting a more rational use of nitrogen following the precision farming concept.[455]

A recent noteworthy approach is the so-called ''aerobic'' photocatalytic nitrogen fixation, in which NRR is conducted in aqueous phase using air as the N_2 source. This alternative technology avoids the need for air separation (indispensable for H–B, electrocatalytic NRR, or gas-phase photo(thermo)catalytic NRR using H_2:N_2) considerably reducing the operation costs, which usually represent around 70% of the total expenses. However, it should be noted that the presence of oxygen may corrode the catalyst surface, limit the solubility of N_2, or react with surface NH species, negatively impacting on the catalyst performance.[121,250] The use of metals with limited oxygen adsorption (*e.g.* Co, Mo or V) may help to overcome this drawback.[456]

From a practical point of view, the key parameter for the application of direct solar ammonia synthesis relies on the amount of ammonia that can be produced per unit area, since it directly affects to the land requirements. Likewise, the occupied area by photoreactors strongly depends on the performance of the catalysts. Best performing NRR photocatalysts have reached ammonia production rates close to 30 mmol h^{-1} g^{-1},[214] and solar to ammonia efficiencies of 0.3%.[232] However, most photocatalysts usually deliver STA below 0.1%, which is the reference value required for practical application.[333,457] This target value imposes serious limitations to photocatalytic NRR to compete with H–B process for centralized ammonia production. However, this may become a competitive technology for off-grid distributed production of solar fertilizers.[329] As a reference, the current nitrogen requirements of crop fields vary between 20–200 kg_N ha^{-1} $year^{-1}$,[458–461] even reaching values as high as 400 kg_N ha^{-1} $year^{-1}$ in some countries (*e.g.* China).[462] Such variations depend on the type of crop, soil, or geography.[463] Considering average fertilizer demands of 50–200 kg_N ha^{-1} $year^{-1}$, some works in literature estimate area requirements for solar capture lower than 10% in regions with high solar flux and using photocatalysts with STA of 0.1%.[329] Comer *et al.*[329] estimated 1% arable land area for solar capture, corresponding to 100 m^2 ha^{-1} (equivalent to 6 typical solar panels per hectare), assuming 50 kg_N ha^{-1} $year^{-1}$. Other estimations foresee farmland requirements of 66 m^2 g^{-1} for photothermal yields of 2.1 mmol h^{-1} g^{-1}.[309]

Regarding costs, technoeconomic analyses[464] indicate the viability of ammonia production, especially *via* aerobic NRR, at competitive costs using different photoreactor configurations, such as slurry (\$5 m^{-2}), fixed panel array (\$20 m^{-2}) and solar concentrator array (\$100 m^{-2}) reactors, and predict achievable production costs under \$600 $t_{NH_3}{}^{-1}$ assuming STA efficiencies of 1% in slurry reactors (see Table 9). On-going and future

Table 9 Estimation of ammonia costs ($ $t_{NH_3}^{-1}$) with different photoreactor configurations, assuming a small size ammonia production plant and solar to ammonia (STA) efficiencies from 1% to 10%. Data extracted from ref. 250

N_2 supply	Reactor	Plant capacity (tpd)	NH_3 cost ($ t^{-1})
Air (no separation)	Slurry	<1 t d^{-1}	30 (STA 10%) 600 (STA 1%)
	Panel		120 (STA 10%) 600 (STA 2.5%)
	Concentrated array		580 (STA 10%)
N_2 (separation by membrane)	Slurry	<1 t d^{-1}	110 (STA 10%)
	Panel		200 (STA 10%)
	Concentrated array		660 (STA 10%)

research on highly active photocatalysts, with high STA efficiencies and enough tolerance to the presence of dissolved oxygen, could facilitate the implementation of aerobic photocatalytic NRR for green ammonia production.

8.6. Implementation challenges and policies for green ammonia technologies

The technoeconomic studies summarized in this section have shown the potential role of green ammonia in the transition to a sustainable circular economy in the chemical industry, transport and energy-related sectors. Estimations based on the existing degree of technological readiness of ammonia production (Table 10) agree on its key role for a decarbonized future scenario, in which public perception will be determinant for a successful transition.

However, there is a lack of technoeconomic studies and life cycle analyses of electrocatalytic and photo(electro)catalytic NRR technologies for green ammonia production, which should be developed in the next years to push the real development and implementation of these sustainable technologies. In the meantime, the International Renewable Energy Agency (IRENA) recommends that the initial target application for green ammonia should be the chemical and fertilizer industries,[27] specially to gain leverage in the retrofitting of existing ammonia plants. To do so, the implementation of renewable ammonia should be accompanied by an adequate regulatory framework, policies and incentives. Indeed, policy uncertainties are associated with high weighted average capital costs (WACC) and thus high levelized costs, which could be decreased through technology demonstrations. Policies should be also oriented to induce demand, and to overcome the main existing barriers for green ammonia development:[27]

Implementation of appropriate taxation policies. Policies may ensure an equitable tax treatment and a long-term guaranteed price for green ammonia. IRENA recommends that those taxes should be based on energy content rather than volume (*e.g.* USD per kilowatt-hour [kW h] instead of USD per litre).

Near-term efforts should focus on green ammonia production *via* retrofitted existing technologies (*e.g.* E/H–B or combinations of technologies) rather than emerging routes. In this regard, light-driven technologies (*i.e.* photo(electro)catalytic, PV-electrocatalytic or photothermal NRR) may find a future niche market in remote locations with high electricity or transportation costs, where these alternative technologies could provide both decentralized production and energy independency. However, the short-term implementation plan of these technologies is still unclear because its dependency on different key issues, such as the volatile price of electricity, the implementation cost of new advanced technologies, their energy requirements, the associated land occupancy (*e.g.* 0.4 ha t^{-1} for average 1 t_{NH_3} d^{-1} production in E/H–B plants[465]), transport limitations and geopolitical aspects.

Implementation of regulations on CO_2 emissions. CO_2 penalties could help to decarbonize ammonia production using the current infrastructure, which would aid to bridge the gap between fossil-based ammonia with unmitigated emissions and green ammonia production.

De-risking early investment projects. Governments may de-risk part of the CAPEX side of the investment of green ammonia plants through grants, loans, and loan guarantees. The OPEX side of the investments may be de-risked with contracts for difference, procurement contracts, off-take guarantees, *etc.* While the CAPEX for green ammonia is higher than fossil-based ammonia plants, its OPEX can be substantially lower (low operating expenses), making green ammonia competitive in the market as a commodity chemical and a renewable fuel.

Table 10 Comparison of the technology readiness level (TRL) of different ammonia production technologies analyzed in this work. Adapted from ref. 24

Ammonia production method	TRL
E/H–B	5–9
Modified E/H–B (R&D: lower temperature catalysts)	1–4
Modified E/H–B (R&D: lower pressure operation)	1–5
Chemical looping	1–4
Electrochemical production	1–3
Light-driven catalytic production	1

9. Summary and outlook

Light-driven green ammonia production has been intensively studied over the past 10 years, as a potential solution to contribute to the decarbonization of the energy system and the fertilizer industry, as well as other pressing sectors such as transportation or chemical industry. This approach also allows for a long-term energy storage that would enable the distribution of excess energy, mitigating both seasonal variability and unpredictable vulnerabilities of the actual centralized production model (*e.g.* price rising during crisis periods). Besides, they

can contribute to reach a total decentralized production of solar fertilizers in next-generation farms. Despite the great potential of NRR technologies to achieve a decentralized ammonia production, they are still at an early stage of development at laboratory scale. At present, best reported light-driven ammonia production rates are close to 30 mmol h^{-1} g^{-1}, with STA efficiencies of 0.3%. However, most photo-(electro)catalysts usually deliver STA lower than 0.1%, which is below the reference values required for practical applications (*i.e.* STA > 0.1% or STA > 20% for its potential application as a fertilizer or fuel, respectively). Thus, the main technological challenge consists on developing stable and high-performing catalysts, which are able to operate with the lowest energy consumption. Catalyst engineering and processes development should also focus their efforts on improving cost competitiveness (*e.g.* avoiding precious metals or complex installations, or using air instead of pure N_2 to avoid separation costs). Besides, the production of ammonia *via* light-driven NRR technologies confronts other challenges different from the technological ones, such as the land use requirements for solar capture, the intermittency of solar irradiation, the access to water reservoirs for H_2 production, or the fluctuation of electricity prices. On this basis, on-going research efforts can make possible to find efficient catalysts and cost-effective technological solutions to push the real implementation of light-driven NRR systems. Besides, the development of technoeconomic studies and life cycle analyses would help to evaluate the technological feasibility and economic viability of these processes, reinforcing the future of green ammonia production technologies for a net-zero carbon society.

Conflicts of interest

There are no conflicts to declare.

Acknowledgements

This work has received funding from the National Projects ARMONIA (PID2020-119125RJ-I00), NovaCO2 (PID2020- 118593RB-C22), 2D-Photo2Change (TED2021-129999A- C33), SOLARCHEM5.0 (TED2021-130173B-C41), SOL-Future (PLEC2021- 0079069), and SolarCPP-Bat (CNS2022-135380), funded by both MCIN/AEI/10.13039/501100011033 and NextGenerationEU/PRTR. Additional funding has been received from FET Proactive program project Hysolchem, and ERC-PoC2022 Demonia (Ref. 101069268). This work received also support from "La Caixa" foundation fellowship (ID 100010434, fellowship code LCF/BQ/PR23/11980046).

References

1 M. Nazemi and M. A. El-Sayed, *Acc. Chem. Res.*, 2021, **54**, 4294–4304.
2 J. H. Kim, D. Hansora, P. Sharma, J. W. Jang and J. S. Lee, *Chem. Soc. Rev.*, 2019, **48**, 1908–1971.
3 J. Su and L. Vayssieres, *ACS Energy Lett.*, 2016, **1**, 121–135.
4 N. S. Lewis, G. Crabtree, A. J. Nozik, M. R. Wasielewski and P. Alivisatos, *Basic Energy Sci. Work. Sol. Energy Util.*, 2005, 1–260.
5 D. L. C. Chandler, 2011.
6 Global Primary Energy.
7 M. Ravi and J. W. Makepeace, *Chem. Sci.*, 2022, **13**, 890–908.
8 J. Chen, W. Zhang, H. Li, W. Li and D. Zhao, *SusMat*, 2021, **1**, 174–193.
9 B. K. Burgess and D. J. Lowe, *Chem. Rev.*, 1996, **96**, 2983–3011.
10 S. L. Meng, X. B. Li, C. H. Tung and L. Z. Wu, *Chemistry*, 2021, **7**, 1431–1450.
11 H. Wang, L. Wang, Q. Wang, S. Ye, W. Sun, Y. Shao, Z. Jiang, Q. Qiao, Y. Zhu, P. Song, D. Li, L. He, X. Zhang, J. Yuan, T. Wu and G. A. Ozin, *Angew. Chem., Int. Ed.*, 2018, **57**, 12360–12364.
12 D. Ziegenbalg, J. Zander and R. Marschall, *ChemPhotoChem*, 2021, **5**, 792–807.
13 X. Chen, N. Li, Z. Kong, W. J. Ong and X. Zhao, *Mater. Horizons*, 2018, **5**, 9–27.
14 A. Braun, D. K. Bora, L. Lauterbach, E. Lettau, H. Wang, S. P. Cramer, F. Yang and J. Guo, *Catal. Today*, 2022, **387**, 186–196.
15 K. H. R. Rouwenhorst, A. S. Travis and L. Lefferts, *Sustainable Chem.*, 2022, **3**, 149–171.
16 L. Wang, M. Xia, H. Wang, K. Huang, C. Qian, C. T. Maravelias and G. A. Ozin, *Joule*, 2018, **2**, 1055–1074.
17 R. M. Nayak-Luke and R. Bañares-Alcántara, *Energy Environ. Sci.*, 2020, **13**, 2957–2966.
18 A. Valera-Medina, H. Xiao, M. Owen-Jones, W. I. F. David and P. J. Bowen, *Prog. Energy Combust. Sci.*, 2018, **69**, 63–102.
19 A. E. Yüzbaşıoğlu, C. Avşar and A. O. Gezerman, *Curr. Res. Green Sustainable Chem.*, 2022, **5**, 100307.
20 S. Ghavam, M. Vahdati, I. A. G. Wilson and P. Styring, *Front. Energy Res.*, 2021, **9**, 1–19.
21 Z. Yan, M. Ji, J. Xia and H. Zhu, *Adv. Energy Mater.*, 2020, **10**, 1–35.
22 G. Qing, R. Ghazfar, S. T. Jackowski, F. Habibzadeh, M. M. Ashtiani, C. P. Chen, M. R. Smith and T. W. Hamann, *Chem. Rev.*, 2020, **120**, 5437–5516.
23 K. H. R. Rouwenhorst, P. M. Krzywda, N. E. Benes, G. Mul and L. Lefferts, *Techno-Economic Challenges of Green Ammonia as an Energy Vector*, Elsevier Inc., 2021, pp. 41–83.
24 The Royal Society, Ammonia: zero-carbon fertiliser, fuel and energy store. Policy Briefing, 2020.
25 International Energy Agency (IEA), *Ammonia Technology Roadmap*, 2021.
26 L. Collado, A. Herrero and V. A. de la Peña O'Shea, *Powerfuels – Status & Prospects*, Springer, 2024, p. Under editing (edition ID 447710).
27 IRENA (International Renewable Energy Agency), Innovation Outlook: Renewable Ammonia, 2022.
28 H. Ali, M. Masar, A. C. Guler, M. Urbanek, M. Machovsky and I. Kuritka, *Nanoscale Adv.*, 2021, **3**, 6358–6372.

29 R. Daiyan, I. Macgill and R. Amal, *ACS Energy Lett.*, 2020, **5**, 3843–3847.
30 Y. Zhao, Y. Miao, C. Zhou and T. Zhang, *Mol. Catal.*, 2022, **518**, 112107.
31 S. Zhang, Y. Zhao, R. Shi, G. I. N. Waterhouse and T. Zhang, *EnergyChem*, 2019, **1**, 100013.
32 X. Hui, L. Wang, Z. Yao, L. Hao and Z. Sun, *Front. Chem.*, 2022, **10**, 1–26.
33 H. P. Jia and E. A. Quadrelli, *Chem. Soc. Rev.*, 2014, **43**, 547–564.
34 Y. Q. Le, J. Gu and W. Q. Tian, *Chem. Commun.*, 2014, **50**, 13319–13322.
35 S. Singh, A. K. Mohammed, A. A. AlHammadi, D. Shetty and K. Polychronopoulou, *Int. J. Hydrogen Energy*, 2023, **48**, 34700–34739.
36 J. John, D. K. Lee and U. Sim, *Nano Convergence*, 2019, **6**, 1–16.
37 R. Zaffaroni, D. Ripepi, J. Middelkoop and F. M. Mulder, *ACS Energy Lett.*, 2020, **5**, 3773–3777.
38 Y. Ren, C. Yu, X. Tan, H. Huang, Q. Wei and J. Qiu, *Energy Environ. Sci.*, 2021, **14**, 1176–1193.
39 C. Mao, H. Li, H. Gu, J. Wang, Y. Zou, G. Qi, J. Xu, F. Deng, W. Shen, J. Li, S. Liu, J. Zhao and L. Zhang, *Chemistry*, 2019, **5**, 2702–2717.
40 H. Kisch, *Eur. J. Inorg. Chem.*, 2020, 1376–1382.
41 N. Gruber and J. N. Galloway, *Nature*, 2008, **451**, 293–296.
42 R. Shi, X. Zhang, G. I. N. Waterhouse, Y. Zhao and T. Zhang, *Adv. Energy Mater.*, 2020, **10**, 1–10.
43 D. Fowler, M. Coyle, U. Skiba, M. A. Sutton, J. N. Cape, S. Reis, L. J. Sheppard, A. Jenkins, B. Grizzetti, J. N. Galloway, P. Vitousek, A. Leach, A. F. Bouwman, K. Butterbach-Bahl, F. Dentener, D. Stevenson, M. Amann and M. Voss, *Philos. Trans. R. Soc. B Biol. Sci.*, 2013, **368**, 20130164.
44 L. C. Seefeldt, B. M. Hoffman and D. R. Dean, *Annu. Rev. Biochem.*, 2009, **78**, 701–722.
45 B. M. Hoffman, D. Lukoyanov, Z. Y. Yang, D. R. Dean and L. C. Seefeldt, *Chem. Rev.*, 2014, **114**, 4041–4062.
46 D. Mallamace, G. Papanikolaou, S. Perathoner, G. Centi and P. Lanzafame, *Int. J. Mol. Sci.*, 2021, **22**, 1–18.
47 R. R. Eady, *Chem. Rev.*, 1996, **96**, 3013–3030.
48 G. E. D. Oldroyd and R. Dixon, *Curr. Opin. Biotechnol*, 2014, **26**, 19–24.
49 D. R. MacFarlane, P. V. Cherepanov, J. Choi, B. H. R. Suryanto, R. Y. Hodgetts, J. M. Bakker, F. M. Ferrero Vallana and A. N. Simonov, *Joule*, 2020, **4**, 1186–1205.
50 H. R. Rucker and B. Kaçar, *Trends Microbiol.*, 2023, 1–11.
51 D. E. Canfield, A. N. Glazer and P. G. Falkowski, *Science*, 2010, **330**, 192–196.
52 J. Norskov and J. Chen, *Sustainable Ammonia Synthesis. Exploring the scientific challenges associated with discovering alternative, sustainable processes for ammonia production*, 2016.
53 M. A. Shipman and M. D. Symes, *Catal. Today*, 2017, **286**, 57–68.
54 H. Wan, A. Bagger and J. Rossmeisl, *J. Phys. Chem. Lett.*, 2022, **13**, 8928–8934.
55 G. Centi, S. Perathoner, C. Genovese and R. Arrigo, *Chem. Commun.*, 2023, **59**, 3005–3023.
56 J. N. Galloway, *Environ. Pollut.*, 1998, **102**, 15–24.
57 NAE Grand Challenges for Engineering. National Academy of Engineering., www.engineeringchallenges.org/challenges.aspx.
58 J. Baltrusaitis, *ACS Sustainable Chem. Eng.*, 2017, **5**, 9527.
59 Y. Feng, Z. zhao, T. Wang, J. Li, M. Xu, H. Jiao, C. Wang, H. Li and M. Feng, *Ceram. Int.*, 2022, **48**, 20062–20069.
60 Z. Ding, M. Sun, W. Liu, W. Sun, X. Meng and Y. Zheng, *Sep. Purif. Technol.*, 2021, **276**, 119287.
61 H. Maimaitizi, A. Abulizi, T. Zhang, K. Okitsu and J. Jie Zhu, *Ultrason. Sonochem.*, 2020, **63**, 104956.
62 X. Ning, D. Jia, S. Li, M. F. Khan and A. Hao, *Ceram. Int.*, 2023, **49**, 21658–21666.
63 L. Chen, J. Wang, X. Li, J. Zhang, C. Zhao, X. Hu, H. Lin, L. Zhao, Y. Wu and Y. He, *Green Energy Environ.*, 2023, **8**, 1630–1643.
64 J. Feng, P. Ning, K. Li, X. Sun, C. Wang, L. Jia and M. Fan, *ACS Sustainable Chem. Eng.*, 2023, **11**, 804–814.
65 I. Muzammil, Y.-N. Kim, H. Kang, D. K. Dinh, S. Choi, C. Jung, Y.-H. Song, E. Kim, J. M. Kim and D. H. Lee, *ACS Energy Lett.*, 2021, **6**, 3004–3010.
66 X. Li, Y. Jiao, Y. Cui, C. Dai, P. Ren, C. Song and X. Ma, *ACS Appl. Mater. Interfaces*, 2021, **13**, 52498–52507.
67 W. Li, S. Zhang, J. Ding, J. Liu, Z. Wang, H. Zhang, J. Ding, L. Chen and C. Liang, *ACS Sustainable Chem. Eng.*, 2023, **11**, 1168–1177.
68 Y. Cui, H. Yang, C. Dai, P. Ren, C. Song and X. Ma, *Ind. Eng. Chem. Res.*, 2022, **61**, 4816–4823.
69 R. K. Sharma, H. Patel, U. Mushtaq, V. Kyriakou, G. Zafeiropoulos, F. Peeters, S. Welzel, M. C. M. van de Sanden and M. N. Tsampas, *ACS Energy Lett.*, 2021, **6**, 313–319.
70 J. Sun, D. Alam, R. Daiyan, H. Masood, T. Zhang, R. Zhou, P. J. Cullen, E. C. Lovell, A. (Rouhollah) Jalili and R. Amal, *Energy Environ. Sci.*, 2021, **14**, 865–872.
71 P. Lamichhane, B. Chandra Adhikari, L. N. Nguyen, R. Paneru, B. Ghimire, S. Mumtaz, J. Sup Lim, Y. June and E. Ha Choi, DOI: **10.1088/1361**.
72 D. Zhou, R. Zhou, R. Zhou, B. Liu, T. Zhang, Y. Xian, P. J. Cullen, X. Lu and K. (Ken) Ostrikov, *Chem. Eng. J.*, 2021, **421**, 129544.
73 J. A. DeWitt, E. V. Phillips, K. L. Hebisch, A. W. Tricker and C. Sievers, *Faraday Discuss.*, 2023, **243**, 65–76.
74 A. W. Tricker, K. L. Hebisch, M. Buchmann, Y.-H. Liu, M. Rose, E. Stavitski, A. J. Medford, M. C. Hatzell and C. Sievers, *ACS Energy Lett.*, 2020, **5**, 3362–3367.
75 D. F. Swearer, N. R. Knowles, H. O. Everitt and N. J. Halas, *ACS Energy Lett.*, 2019, **4**, 1505–1512.
76 E. M. Gaffney, M. Grattieri, K. Beaver, J. Pham, C. McCartney and S. D. Minteer, *Electrochim. Acta*, 2013, **337**, 135731.
77 M. Grattieri, K. Beaver, E. M. Gaffney, F. Dong and S. D. Minteer, *Chem. Commun.*, 2020, **56**, 8553–8568.
78 R. Yadav, P. Chiranjeevi, S. Yadav, R. Singh and S. A. Patil, *J. CO2 Util.*, 2022, **60**, 101997.

79 X. Xue, R. Chen, C. Yan, P. Zhao, Y. Hu, W. Zhang, S. Yang and Z. Jin, *Nano Res.*, 2019, **12**, 1229–1249.
80 B. Puértolas, M. Comesaña-Hermo, L. V. Besteiro, M. Vázquez-González and M. A. Correa-Duarte, *Adv. Energy Mater.*, 2022, **12**, 2103909.
81 L. Li, C. Tang, H. Jin, K. Davey and S. Z. Qiao, *Chemistry*, 2021, **7**, 3232–3255.
82 A. Biswas, S. Bhardwaj, T. Boruah and R. S. Dey, *Mater. Adv.*, 2022, **3**, 5207–5233.
83 H. Xu, K. Ithisuphalap, Y. Li, S. Mukherjee, J. Lattimer, G. Soloveichik and G. Wu, *Nano Energy*, 2020, **69**, 104469.
84 Q. Qin and M. Oschatz, *ChemElectroChem*, 2020, **7**, 878–889.
85 X. Yan, D. Liu, H. Cao, F. Hou, J. Liang and S. X. Dou, *Small Methods*, 2019, **3**, 1800501.
86 Z. Qiao, D. Johnson and A. Djire, *Cell Rep. Phys. Sci.*, 2021, **2**, 100438.
87 C. Ling, Y. Zhang, Q. Li, X. Bai, L. Shi and J. Wang, *J. Am. Chem. Soc.*, 2019, **141**, 18264–18270.
88 H. Shen, C. Choi, J. Masa, X. Li, J. Qiu, Y. Jung and Z. Sun, *Chemistry*, 2021, **7**, 1708–1754.
89 T. Hou, Y. Xiao, P. Cui, Y. Huang, X. Tan, X. Zheng, Y. Zou, C. Liu, W. Zhu, S. Liang and L. Wang, *Adv. Energy Mater.*, 2019, **9**, 1–8.
90 J. Timoshenko and B. R. Cuenya, *Chem. Rev.*, 2021, **121**, 882–961.
91 Q. Wang, Y. Xiao, S. Yang, Y. Zhang, L. Wu, H. Pan, D. Rao, T. Chen, Z. Sun, G. Wang, J. Zhu, J. Zeng, S. Wei and X. Zheng, *Nano Lett.*, 2022, **22**, 10216–10223.
92 H. Shen, M. Yang, L. Hao, J. Wang, J. Strunk and Z. Sun, *Nano Res.*, 2022, **15**, 2773–2809.
93 X. Zhang, Y. Lyu, H. Zhou, J. Zheng, A. Huang, J. Ding, C. Xie, R. De Marco, N. Tsud, V. Kalinovych, S. P. Jiang, L. Dai and S. Wang, *Adv. Mater.*, 2023, **35**, 1–9.
94 T. Zeng, Y. Hu, Z. Yuan, H. He, X. Zhao, X. Zhao, X. Jian, H. Zhang and X. Gao, *J. Alloys Compd.*, 2023, **975**, 172851.
95 X. Cheng, R. Guan, Z. Wu, Y. Sun, W. Che and Q. Shang, *InfoMat*, 2024, **6**, 1–15.
96 S. Zhang, Y. Zhao, R. Shi, C. Zhou, G. I. N. Waterhouse, L. Z. Wu, C. H. Tung and T. Zhang, *Adv. Energy Mater.*, 2020, **10**, 1–10.
97 Y. Fang, Y. Cao, B. Tan and Q. Chen, *ACS Appl. Mater. Interfaces*, 2021, **13**, 42624–42634.
98 Y. Wang, Z. Li, H. Zhu, X. Xu, Z. Zeng, X. Liu, H. Wang, M. Gong, X. Liu and Y. Wang, *Chem. Eng. J.*, 2024, **484**, 149583.
99 S. Ajmal, A. Rasheed, N. Q. Tran, X. Shao, Y. Hwang, V. Q. Bui, Y. D. Kim, J. Kim and H. Lee, *Appl. Catal., B*, 2023, **321**, 122070.
100 S. Li, Z. Yao, J. Zheng, M. Fu, J. Cen, S. Hwang, H. Jin, A. Orlov, L. Gu, S. Wang, Z. Chen and D. Su, *Angew. Chem., Int. Ed.*, 2020, **59**, 22092–22099.
101 S. Kondo, T. Mitsuma, N. Shibata and Y. Ikuhara, *Sci. Adv.*, 2016, **2**, 1–8.
102 O. Kwon, Y. I. Kim, K. Kim, J. C. Kim, J. H. Lee, S. S. Park, J. W. Han, Y. M. Kim, G. Kim and H. Y. Jeong, *Nano Lett.*, 2020, **20**, 8353–8359.
103 H. Iriawan, S. Z. Andersen, X. Zhang, B. M. Comer, J. Barrio, P. Chen, A. J. Medford, I. E. L. Stephens, I. Chorkendorff and Y. Shao-Horn, *Nat. Rev. Methods Prim.*, 2021, **1**, 56.
104 Z. W. She, J. Kibsgaard, C. F. Dickens, I. Chorkendorff, J. K. Nørskov and T. F. Jaramillo, *Science*, 2017, **355**, eaad4998.
105 S. L. Foster, S. I. P. Bakovic, R. D. Duda, S. Maheshwari, R. D. Milton, S. D. Minteer, M. J. Janik, J. N. Renner and L. F. Greenlee, *Nat. Catal.*, 2018, **1**, 490–500.
106 A. R. Singh, B. A. Rohr, J. A. Schwalbe, M. Cargnello, K. Chan, T. F. Jaramillo, I. Chorkendorff and J. K. Nørskov, *ACS Catal.*, 2017, **7**, 706–709.
107 Y. Cheng, X. Xu, M. Wang, C. Deng, Y. Sun, C. Yan and T. Qian, *Adv. Funct. Mater.*, 2023, **33**, 20232302332.
108 J. Jacquemin, M. F. Costa Gomes, P. Husson and V. Majer, *J. Chem. Thermodyn.*, 2006, **38**, 490–502.
109 D. Almantariotis, S. Stevanovic, O. Fandiño, A. S. Pensado, A. A. H. Padua, J.-Y. Coxam and M. F. C. Gomes, *J. Phys. Chem. B*, 2012, **116**, 7728–7738.
110 C. S. M. Kang, X. Zhang and D. R. MacFarlane, *J. Phys. Chem. C*, 2018, **122**, 24550–24558.
111 T. A. Bu, Y. C. Hao, W. Y. Gao, X. Su, L. W. Chen, N. Zhang and A. X. Yin, *Nanoscale*, 2019, **11**, 10072–10079.
112 C. Guo, J. Ran, A. Vasileff and S. Z. Qiao, *Energy Environ. Sci.*, 2018, **11**, 45–56.
113 D. L. J. Broere and P. L. Holland, *Science*, 2018, **359**, 871.
114 R. Shi, Y. Zhao, G. I. N. Waterhouse, S. Zhang and T. Zhang, *ACS Catal.*, 2019, **9**, 9739–9750.
115 M. Yang, J. Liu, H. Xu, Y. Pei, C. Jiang, D. He and X. Xiao, *ChemPhysMater*, 2022, **1**, 155–182.
116 D. Yan, H. Li, C. Chen, Y. Zou and S. Wang, *Small Methods*, 2019, **3**, 1800331.
117 Y. Zhao, Y. Zhao, G. I. N. Waterhouse, L. Zheng, X. Cao, F. Teng, L. Z. Wu, C. H. Tung, D. O'Hare and T. Zhang, *Adv. Mater.*, 2017, **29**, 1–10.
118 M. Guan, C. Xiao, J. Zhang, S. Fan, R. An, Q. Cheng, J. Xie, M. Zhou, B. Ye and Y. Xie, *J. Am. Chem. Soc.*, 2013, **135**, 10411–10417.
119 W. Zhou and H. Fu, *Inorg. Chem. Front.*, 2018, **5**, 1240–1254.
120 Z. Zafar, S. Yi, J. Li, C. Li, Y. Zhu, A. Zada, W. Yao, Z. Liu and X. Yue, *Energy Environ. Mater.*, 2022, **5**, 68–114.
121 H. Hirakawa, M. Hashimoto, Y. Shiraishi and T. Hirai, *J. Am. Chem. Soc.*, 2017, **139**, 10929–10936.
122 Y. Zhao, Y. Zhao, R. Shi, B. Wang, G. I. N. Waterhouse, L. Z. Wu, C. H. Tung and T. Zhang, *Adv. Mater.*, 2019, **31**, 1–9.
123 H. Li, J. Zhang, X. Deng, Y. Wang, G. Meng, R. Liu, J. Huang, M. Tu, C. Xu, Y. Peng, B. Wang and Y. Hou, *Angew. Chem., Int. Ed.*, 2024, **63**, 1–11.
124 J. Yang, Y. Guo, R. Jiang, F. Qin, H. Zhang, W. Lu, J. Wang and J. C. Yu, *J. Am. Chem. Soc.*, 2018, **140**, 8497–8508.
125 B. Sun, Z. Liang, Y. Qian, X. Xu, Y. Han and J. Tian, *ACS Appl. Mater. Interfaces*, 2020, **12**, 7257–7269.

126 Y. Guo, J. Yang, D. Wu, H. Bai, Z. Yang, J. Wang and B. Yang, *J. Mater. Chem. A*, 2020, **8**, 16218–16231.
127 C. Liang, H. Y. Niu, H. Guo, C. G. Niu, D. W. Huang, Y. Y. Yang, H. Y. Liu, B. Bin Shao and H. P. Feng, *Chem. Eng. J.*, 2020, **396**, 125395.
128 W. Ding, X. Li, S. Su, Z. Liu, Y. Cao, L. Meng, S. Yuan, W. Wei and M. Luo, *Nanoscale*, 2023, **15**, 4014–4021.
129 M. Arif, M. Babar, U. Azhar, M. Sagir, M. Bilal Tahir, M. Asim Mushtaq, G. Yasin, M. Mubashir, J. Wei Roy Chong, K. Shiong Khoo and P. Loke Show, *Chem. Eng. J.*, 2023, **451**, 138320.
130 N. Zhang, A. Jalil, D. Wu, S. Chen, Y. Liu, C. Gao, W. Ye, Z. Qi, H. Ju, C. Wang, X. Wu, L. Song, J. Zhu and Y. Xiong, *J. Am. Chem. Soc.*, 2018, **140**, 9434–9443.
131 K. Li, W. Cai, Z. Zhang, H. Xie, Q. Zhong and H. Qu, *Chem. Eng. J.*, 2022, **435**, 135017.
132 P. Huang, W. Liu, Z. He, C. Xiao, T. Yao, Y. Zou, C. Wang, Z. Qi, W. Tong, B. Pan, S. Wei and Y. Xie, *Sci. China: Chem.*, 2018, **61**, 1187–1196.
133 Y. Bo, H. Wang, Y. Lin, T. Yang, R. Ye, Y. Li, C. Hu, P. Du, Y. Hu, Z. Liu, R. Long, C. Gao, B. Ye, L. Song, X. Wu and Y. Xiong, *Angew. Chem.*, 2021, **133**, 16221–16228.
134 H. Li, G. Wang, Q. Deng, W. Hu and W. Hou, *Appl. Catal., B*, 2024, **344**, 123652.
135 C. Yang, Y. Zhang, F. Yue, R. Du, T. Ma, Y. Bian, R. Li, L. Guo, D. Wang and F. Fu, *Appl. Catal., B*, 2023, **338**, 123057.
136 L. Wang, Y. Xia and J. Yu, *Chemistry*, 2021, **7**, 1983–1985.
137 K. T. Ranjit, T. K. Varadarajan and B. Viswanathan, *J. Photochem. Photobiol., A*, 1996, **96**, 181–185.
138 P. Qiu, C. Huang, G. Dong, F. Chen, F. Zhao, Y. Yu, X. Liu, Z. Li and Y. Wang, *J. Mater. Chem. A*, 2021, **9**, 14459–14465.
139 Y. Liu, Z. Yu, S. Guo, L. Yao, R. Sun, X. Huang and W. Zhao, *New J. Chem.*, 2020, **44**, 19924–19932.
140 A. Ray, S. Sultana, S. P. Tripathy and K. Parida, *ACS Sustainable Chem. Eng.*, 2021, **9**, 6305–6317.
141 Y. Liao, J. Qian, G. Xie, Q. Han, W. Dang, Y. Wang, L. Lv, S. Zhao, L. Luo, W. Zhang, H. Y. Jiang and J. Tang, *Appl. Catal., B*, 2020, **273**, 119054.
142 Z. K. Shen, Y. J. Yuan, P. Wang, W. Bai, L. Pei, S. Wu, Z. T. Yu and Z. Zou, *ACS Appl. Mater. Interfaces*, 2020, **12**, 17343–17352.
143 J. H. Montoya, C. Tsai, A. Vojvodic and J. K. Nørskov, *ChemSusChem*, 2015, **8**, 2180–2186.
144 S. Bian, M. Wen, J. Wang, N. Yang, P. K. Chu and X. F. Yu, *J. Phys. Chem. Lett.*, 2020, **11**, 1052–1058.
145 D. Cui, S. Wang, X. Yang, L. Xu and F. Li, *Small*, 2024, **20**, 2306229.
146 Y. Xue, X. Kong, Y. Guo, Z. Liang, H. Cui and J. Tian, *J. Mater.*, 2020, **6**, 128–137.
147 L. Li, Y. Wang, S. Vanka, X. Mu, Z. Mi and C.-J. Li, *Angew. Chem., Int. Ed.*, 2017, **56**, 8701–8705.
148 S. Sun, Q. An, W. Wang, L. Zhang and J. Liu, *J. Mater. Chem. A*, 2017, **5**, 201–209.
149 C. Liang, H. Y. Niu, H. Guo, C. G. Niu, Y. Y. Yang, H. Y. Liu, W. W. Tang and H. P. Feng, *Chem. Eng. J.*, 2021, **406**, 126868.
150 S. M. Stratton, S. Zhang and M. M. Montemore, *Surf. Sci. Rep.*, 2023, **78**, 100597.
151 S. Dutta and S. K. Pati, *Catal. Today*, 2023, **424**, 113804.
152 X. Lv, W. Wei, F. Li, B. Huang and Y. Dai, *Nano Lett.*, 2019, **19**, 6391–6399.
153 X. W. Guo, S. M. Chen, H. J. Wang, Z. M. Zhang, H. Lin, L. Song and T. B. Lu, *J. Mater. Chem. A*, 2019, **7**, 19831–19837.
154 X. Liu, Y. Luo, C. Ling, Y. Shi, G. Zhan, H. Li, H. Gu, K. Wei, F. Guo, Z. Ai and L. Zhang, *Appl. Catal., B*, 2022, **301**, 120766.
155 J. Li, P. Liu, Y. Tang, H. Huang, H. Cui, D. Mei and C. Zhong, *ACS Catal.*, 2020, **10**, 2431–2442.
156 L. Chen and X. Feng, *Chem. Sci.*, 2020, **11**, 3124–3131.
157 J. Zheng, Y. Lyu, M. Qiao, R. Wang, Y. Zhou, H. Li, C. Chen, Y. Li, H. Zhou, S. P. Jiang and S. Wang, *Chemistry*, 2019, **5**, 617–633.
158 C. Lee, H. Kim and Y. J. Jang, *ACS Appl. Energy Mater.*, 2022, **5**, 11018–11024.
159 X. Wang, X. Shi, S. Yin, P. She, J. Zheng, Y. Song and H. Sun, *J. Mater. Chem. A*, 2023, **11**, 9976–9988.
160 Z. Lu, S. E. Saji, J. Langley, Y. Lin, Z. Xie, K. Yang, L. Bao, Y. Sun, S. Zhang, Y. H. Ng, L. Song, N. Cox and Z. Yin, *Appl. Catal., B*, 2021, **294**, 120240.
161 S. Vaclav, *Nature*, 1999, **400**, 415.
162 V. Smil, 2000.
163 Y. Liu, S. Zhou, J. Li, Y. Wang, G. Jiang, Z. Zhao, B. Liu, X. Gong, A. Duan, J. Liu, Y. Wei and L. Zhang, *Appl. Catal., B*, 2015, **168–169**, 125–131.
164 C. Smith, A. K. Hill and L. Torrente-Murciano, *Energy Environ. Sci.*, 2020, **13**, 331–344.
165 R. Michalsky, B. J. Parman, V. Amanor-Boadu and P. H. Pfromm, *Energy*, 2012, **42**, 251–260.
166 C. J. H. Jacobsen, S. Dahl, B. S. Clausen, S. Bahn, A. Logadottir and J. K. Nørskov, *J. Am. Chem. Soc.*, 2001, **123**, 8404–8405.
167 G. Ertl, M. Weiss and S. B. Lee, *Chem. Phys. Lett.*, 2013, **589**, 18–20.
168 A. Ozaki, *Acc. Chem. Res.*, 1981, **14**, 16–21.
169 F. Rosowski, A. Hornung, O. Hinrichsen, D. Herein, M. Muhler and G. Ertl, *Appl. Catal., A*, 1997, **151**, 443–460.
170 K. Aika, H. Hori and A. Ozaki, *J. Catal.*, 1972, **27**, 424–431.
171 M. Appl, *Ammonia: Principles and Industrial Practice*, Wiley Online Books, 1999, pp. 65–176.
172 N. Saadatjou, A. Jafari and S. Sahebdelfar, *Chem. Eng. Commun.*, 2015, **202**, 420–448.
173 J. Humphreys, R. Lan and S. Tao, *Adv. Energy Sustainable Res.*, 2021, **2**, 2000043.
174 Z. Yang, W. Guo, J. Lin and D. Liao, *Chin. J. Catal.*, 2006, **27**, 378–380.
175 M. Kitano, Y. Inoue, Y. Yamazaki, F. Hayashi, S. Kanbara, S. Matsuishi, T. Yokoyama, S. W. Kim, M. Hara and H. Hosono, *Nat. Chem.*, 2012, **4**, 934–940.
176 M. Hara, M. Kitano and H. Hosono, *ACS Catal.*, 2017, **7**, 2313–2324.

177 M. Kitano, S. Kanbara, Y. Inoue, N. Kuganathan, P. V. Sushko, T. Yokoyama, M. Hara and H. Hosono, *Nat. Commun.*, 2015, **6**, 1–9.
178 M. Kitano, Y. Inoue, H. Ishikawa, K. Yamagata, T. Nakao, T. Tada, S. Matsuishi, T. Yokoyama, M. Hara and H. Hosono, *Chem. Sci.*, 2016, **7**, 4036–4043.
179 J. Li, J. Wu, H. Wang, Y. Lu, T. Ye, M. Sasase, X. Wu, M. Kitano, T. Inoshita and H. Hosono, *Chem. Sci.*, 2019, **10**, 5712–5718.
180 M. Hattori, T. Mori, T. Arai, Y. Inoue, M. Sasase, T. Tada, M. Kitano, T. Yokoyama, M. Hara and H. Hosono, *ACS Catal.*, 2018, **8**, 10977–10984.
181 J. Wu, Y. Gong, T. Inoshita, D. C. Fredrickson, J. Wang, Y. Lu, M. Kitano and H. Hosono, *Adv. Mater.*, 2017, **29**, 1700924.
182 P. Wang, F. Chang, W. Gao, J. Guo, G. Wu, T. He and P. Chen, *Nat. Chem.*, 2017, **9**, 64–70.
183 W. Gao, S. Feng, H. Yan, Q. Wang, H. Xie, L. Jiang, W. Zhang, Y. Guan, H. Wu, H. Cao, J. Guo and P. Chen, *Chem. Commun.*, 2021, **57**, 8576–8579.
184 Y. Cao, A. Saito, Y. Kobayashi, H. Ubukata, Y. Tang and H. Kageyama, *ChemCatChem*, 2021, **13**, 191–195.
185 W. Gao, P. Wang, J. Guo, F. Chang, T. He, Q. Wang, G. Wu and P. Chen, *ACS Catal.*, 2017, **7**, 3654–3661.
186 Y. Kobayashi, Y. Tang, T. Kageyama, H. Yamashita, N. Masuda, S. Hosokawa and H. Kageyama, *J. Am. Chem. Soc.*, 2017, **139**, 18240–18246.
187 L. Li, T. Zhang, J. Cai, H. Cai, J. Ni, B. Lin, J. Lin, X. Wang, L. Zheng, C.-T. Au and L. Jiang, *J. Catal.*, 2020, **389**, 218–228.
188 Q. Wang, J. Pan, J. Guo, H. Anton Hansen, H. Xie, L. Jiang, L. Hua, H. Li, Y. Guan, P. Wang, W. Gao, L. Liu, H. Cao, Z. Xiong, T. Vegge and P. Chen, *Ternary ruthenium complex hydrides for ammonia synthesis Hydrogen content*.
189 F. Chang, Y. Guan, X. Chang, J. Guo, P. Wang, W. Gao, G. Wu, J. Zheng, X. Li and P. Chen, *J. Am. Chem. Soc.*, 2018, **140**, 14799–14806.
190 Y. Guan, W. Zhang, Q. Wang, C. Weidenthaler, A. Wu, W. Gao, Q. Pei, H. Yan, J. Cui, H. Wu, S. Feng, R. Wang, H. Cao, X. Ju, L. Liu, T. He, J. Guo and P. Chen, *Chem. Catal.*, 2021, **1**, 1042–1054.
191 Y. Tang, Y. Kobayashi, N. Masuda, Y. Uchida, H. Okamoto, T. Kageyama, S. Hosokawa, F. Loyer, K. Mitsuhara, K. Yamanaka, Y. Tamenori, C. Tassel, T. Yamamoto, T. Tanaka and H. Kageyama, *Adv. Energy Mater.*, 2018, **8**, 1801772.
192 M. Kitano, J. Kujirai, K. Ogasawara, S. Matsuishi, T. Tada, H. Abe, Y. Niwa and H. Hosono, *J. Am. Chem. Soc.*, 2019, **141**, 20344–20353.
193 H. Yamashita, T. Broux, Y. Kobayashi, F. Takeiri, H. Ubukata, T. Zhu, M. A. Hayward, K. Fujii, M. Yashima, K. Shitara, A. Kuwabara, T. Murakami and H. Kageyama, *J. Am. Chem. Soc.*, 2018, **140**, 11170–11173.
194 K. Ooya, J. Li, K. Fukui, S. Iimura, T. Nakao, K. Ogasawara, M. Sasase, H. Abe, Y. Niwa, M. Kitano and H. Hosono, *Adv. Energy Mater.*, 2021, **11**, 2003723.
195 H. Mizoguchi, M. Okunaka, M. Kitano, S. Matsuishi, T. Yokoyama and H. Hosono, *Inorg. Chem.*, 2016, **55**, 8833–8838.
196 M. Hattori, S. Iijima, T. Nakao, H. Hosono and M. Hara, *Nat. Commun.*, 2020, **11**, 1–8.
197 H. Michikazu, H. Masashi, O. Natsuo and K. Hiyori, *Nat. Portf*, 2022, 1–15.
198 Y. Ogura, K. Sato, S. Miyahara, Y. Kawano, T. Toriyama, T. Yamamoto, S. Matsumura, S. Hosokawa and K. Nagaoka, *Chem. Sci.*, 2018, **9**, 2230–2237.
199 Y. Ogura, K. Tsujimaru, K. Sato, S. Miyahara, T. Toriyama, T. Yamamoto, S. Matsumura and K. Nagaoka, *ACS Sustainable Chem. Eng.*, 2018, **6**, 17258–17266.
200 K. Sato, S. Miyahara, Y. Ogura, K. Tsujimaru, Y. Wada, T. Toriyama, T. Yamamoto, S. Matsumura and K. Nagaoka, *ACS Sustainable Chem. Eng.*, 2020, **8**, 2726–2734.
201 Y. Inoue, M. Kitano, K. Kishida, H. Abe, Y. Niwa, M. Sasase, Y. Fujita, H. Ishikawa, T. Yokoyama, M. Hara and H. Hosono, *ACS Catal.*, 2016, **6**, 7577–7584.
202 M. Kitano, Y. Inoue, M. Sasase, K. Kishida, Y. Kobayashi, K. Nishiyama, T. Tada, S. Kawamura, T. Yokoyama, M. Hara and H. Hosono, *Angew. Chem., Int. Ed.*, 2018, **57**, 2648–2652.
203 H. Yamamoto, H. Miyaoka, S. Hino, H. Nakanishi, T. Ichikawa and Y. Kojima, *Int. J. Hydrogen Energy*, 2009, **34**, 9760–9764.
204 P. Chen, Z. Xiong, J. Luo, J. Lin and K. L. Tan, *Nature*, 2002, **420**, 302–304.
205 Y. Kojima, Y. Kawai and N. Ohba, *J. Power Sources*, 2006, **159**, 81–87.
206 W. Gao, J. Guo, P. Wang, Q. Wang, F. Chang, Q. Pei, W. Zhang, L. Liu and P. Chen, *Nat. Energy*, 2018, **3**, 1067–1075.
207 K. H. R. Rouwenhorst, A. G. J. Van der Ham, G. Mul and S. R. A. Kersten, *Renew. Sustainable Energy Rev.*, 2019, **114**, 109339.
208 A. S. Travis, *Casale: The first 100 years*, Casale S.A., 2022.
209 A. S. Travis, *Nitrogen Capture: The Growth of an International Industry (1900–1940)*, Springer International Publishing, Cham (Switzerland), 2018, pp. 93–127.
210 A. S. Travis, *Nitrogen Capture: The Growth of an International Industry (1900–1940)*, Springer International Publishing, Cham (Switzerland), 2018, pp. 347–360.
211 V. Pattabathula and J. Richardson, *Chem. Eng. Prog.*, 2016, **112**, 69–75.
212 G. N. Schrauzer and T. D. Guth, *J. Am. Chem. Soc.*, 1977, **99**, 7189–7193.
213 G. N. Schrauzer, in *Energy Efficiency and Renewable Energy Through Nanotechnology*, ed. L. Zang, Springer London, London, 2011, pp. 601–623.
214 Y. Liu, Y. Xue, L. Hui, H. Yu, Y. Fang, F. He and Y. Li, *Nano Energy*, 2021, **89**, 106333.
215 G. Liu, Z. Tang, X. Gu, N. Li, H. Lv, Y. Huang, Y. Zeng, M. Yuan, Q. Meng, Y. Zhou and C. Wang, *Appl. Catal., B*, 2022, **317**, 121752.
216 S. Zhang, X. Rong, T. Sun, P. Gao, J. Liu, X. Qiu, X. Zhou and Z. Wu, *Diam. Relat. Mater.*, 2023, **138**, 110167.

217 P. Li, Z. Zhou, Q. Wang, M. Guo, S. Chen, J. Low, R. Long, W. Liu, P. Ding, Y. Wu and Y. Xiong, *J. Am. Chem. Soc.*, 2020, **142**, 12430–12439.
218 A. R. S. C. Lazuli, R. Thapa and B. Neppolian, *Catal. Today*, 2023, **420**, 114034.
219 X. Rong, Y. Mao, J. Xu, X. Zhang, L. Zhang, X. Zhou, F. Qiu and Z. Wu, *Catal. Commun.*, 2018, **116**, 16–19.
220 S. Cao, B. Fan, Y. Feng, H. Chen, F. Jiang and X. Wang, *Chem. Eng. J.*, 2018, **353**, 147–156.
221 S. Sultana, S. Mansingh and K. M. Parida, *J. Mater. Chem. A*, 2019, **7**, 9145–9153.
222 R. Bariki, S. K. Pradhan, S. Panda, S. K. Nayak, A. R. Pati and B. G. Mishra, *Langmuir*, 2023, **39**, 7707–7722.
223 H. Yin, Z. Chen, Y. Peng, S. Xiong, Y. Li, H. Yamashita and J. Li, *Angew. Chem., Int. Ed.*, 2022, **61**, e202114242.
224 J. Fan, M. Zuo, Z. Ding, Z. Zhao, J. Liu and B. Sun, *Chem. Eng. J.*, 2020, **396**, 125263.
225 X. Li, X. Sun, L. Zhang, S. Sun and W. Wang, *J. Mater. Chem. A*, 2018, **6**, 3005–3011.
226 M. H. Urgesa, G. S. Wolde and D.-H. Kuo, *Chem. Eng. J.*, 2023, **464**, 142717.
227 H. Zeng, S. Terazono and T. Tanuma, *Catal. Commun.*, 2015, **59**, 40–44.
228 X. Wang, B. Wang, S. Yin, M. Xu, L. Yang and H. Sun, *J. Cleaner Prod.*, 2022, **360**, 132162.
229 Z. Ding, S. Wang, X. Chang, D. H. Wang and T. Zhang, *RSC Adv.*, 2020, **10**, 26246–26255.
230 R. Tao, X. Li, X. Li, C. Shao and Y. Liu, *Nanoscale*, 2020, **12**, 8320–8329.
231 Y. Bai, L. Ye, T. Chen, L. Wang, X. Shi, X. Zhang and D. Chen, *ACS Appl. Mater. Interfaces*, 2016, **8**, 27661–27668.
232 D. Prusty, S. Mansingh and K. M. Parida, *Catal. Sci. Technol.*, 2023, **13**, 1311–1324.
233 Y. Xue, C. Ma, Q. Yang, X. Wang, S. An, X. Zhang and J. Tian, *Chem. Eng. J.*, 2023, **457**, 141146.
234 M. H. Urgesa, G. S. Wolde and D.-H. Kuo, *J. Alloys Compd.*, 2023, **947**, 169589.
235 S. Liu, M. Wang, H. Ji, L. Zhang, J. Ni, N. Li, T. Qian, C. Yan and J. Lu, *Adv. Mater.*, 2023, **35**, 2211730.
236 Y. Fang, Y. Xue, L. Hui, H. Yu and Y. Li, *Angew. Chem., Int. Ed.*, 2021, **60**, 3170–3174.
237 Y. Xue, Y. Guo, Z. Liang, H. Cui and J. Tian, *J. Colloid Interface Sci.*, 2019, **556**, 206–213.
238 B. Bagherpour and S. Dehghanpour, *J. Solid State Chem.*, 2023, **324**, 124079.
239 M. Lan, N. Zheng, X. Dong, H. Ma and X. Zhang, *Colloids Surf., A*, 2021, **623**, 126744.
240 J. Wang, Y. Fang, W. Zhang, X. Yu, L. Wang and Y. Zhang, *Appl. Surf. Sci.*, 2021, **567**, 150623.
241 L. Shi, Z. Li, L. Ju, A. Carrasco-Pena, N. Orlovskaya, H. Zhou and Y. Yang, *J. Mater. Chem. A*, 2020, **8**, 1059–1065.
242 S. Wang, X. Hai, X. Ding, K. Chang, Y. Xiang, X. Meng, Z. Yang, H. Chen and J. Ye, *Adv. Mater.*, 2017, **29**, 1–7.
243 Y. Hao, X. Dong, S. Zhai, H. Ma, X. Wang and X. Zhang, *Chem. – Eur. J.*, 2016, **22**, 18722–18728.
244 I. F. de Sá, P. H. P. R. Carvalho, H. A. Centurion, R. V. Gonçalves and J. D. Scholten, *ACS Sustainable Chem. Eng.*, 2021, **9**, 8721–8730.
245 X. Feng, H. Chen, F. Jiang and X. Wang, *Catal. Sci. Technol.*, 2019, **9**, 2849–2857.
246 H. Zhang, Y. Chen, L. Bao and Y. J. Yuan, *J. Catal.*, 2022, **412**, 1–9.
247 T.-A. Bu, Y.-C. Hao, W.-Y. Gao, X. Su, L.-W. Chen, N. Zhang and A.-X. Yin, *Nanoscale*, 2019, **11**, 10072–10079.
248 Q. Ding, X. Zou, J. Ke, Y. Dong, Y. Cui and H. Ma, *J. Colloid Interface Sci.*, 2023, **649**, 148–158.
249 N. Zhang, L. Li, Q. Shao, T. Zhu, X. Huang and X. Xiao, *ACS Appl. Energy Mater.*, 2019, **2**, 8394–8398.
250 Y. H. Liu, C. A. Fernández, S. A. Varanasi, N. N. Bui, L. Song and M. C. Hatzell, *ACS Energy Lett.*, 2022, **7**, 24–29.
251 Y. Shen, J. Shou, L. Chen, W. Han, L. Zhang, Y. Chen, X. Tu, S. Zhang, Q. Sun, Y. Chang and H. Zheng, *Appl. Catal., A*, 2022, **643**, 118739.
252 L. Chen, J. Shou, Y. Chen, W. Han, X. Tu, L. Zhang, Q. Sun, J. Cao, Y. Chang and H. Zheng, *Chem. Eng. J.*, 2023, **451**, 138592.
253 Y. Shen, L. Chen, L. Zhang, W. Han, M. Jiang and H. Zheng, *Mol. Catal.*, 2022, **518**, 112091.
254 Y. Shen, L. Chen, L. Zhang, W. Han, Y. Chang and H. Zheng, *Mol. Catal.*, 2022, **524**, 112338.
255 K. Pournemati, A. Habibi-Yangjeh and A. Khataee, *J. Colloid Interface Sci.*, 2023, **641**, 1000–1013.
256 W. Zhao, J. Qin, W. Teng, J. Mu, C. Chen, J. Ke, J. C. Huang, B. Liu and S. Wang, *Appl. Catal., B*, 2022, **305**, 121046.
257 S. Rostami, R. Tayebee and B. Mahdavi, *RSC Adv.*, 2023, **13**, 31303–31313.
258 T. Wang, J. Liu, P. Wu, C. Feng, D. Wang, H. Hu and G. Xue, *J. Mater. Chem. A*, 2020, **8**, 16590–16598.
259 D. R. MacFarlane, A. N. Simonov, T. M. Vu, S. Johnston and L. M. Azofra, *Faraday Discuss.*, 2023, **243**, 557–570.
260 A. J. Bard, *Science*, 1980, **207**, 139–144.
261 M. Bellardita, V. Loddo, F. Parrino and L. Palmisano, *ChemPhotoChem*, 2021, **5**, 767–791.
262 A. Fujishima and K. Honda, *Nature*, 1972, **238**, 37–38.
263 D. R. Strongin and G. A. Somorjai, Surface Science and Catalytic Study of the Effects of Aluminum Oxide and Potassium on the Ammonia Synthesis Over Iron Single-Crystal Surfaces, *Catalytic Ammonia Synthesis: Fundamentals and Practice*, Springer US, 1991, ch. 4, pp. 133–177.
264 J. Brillet, J. H. Yum, M. Cornuz, T. Hisatomi, R. Solarska, J. Augustynski, M. Graetzel and K. Sivula, *Nat. Photonics*, 2012, **6**, 824–828.
265 Y. Shi, T. Y. Hsieh, M. A. Hoque, W. Cambarau, S. Narbey, C. Gimbert-Surinãch, E. Palomares, M. Lanza and A. Llobet, *ACS Appl. Mater. Interfaces*, 2020, **12**, 55856–55864.
266 D. Cardenas-Morcoso, M. García-Tecedor, T. Merdzhanova, V. Smirnov, F. Finger, B. Kaiser, W. Jaegermann and S. Gimenez, *Mater. Adv.*, 2020, **1**, 1202–1211.
267 Y. J. Jang, A. E. Lindberg, M. A. Lumley and K. Choi, *ACS Energy Lett.*, 2020, **5**, 1834–1839.

268 Y. Jia, J. Gao, Z. Xiao, Z. Tian, Y. Xia and C. Wang, *ACS Appl. Mater. Interfaces*, 2023, **15**, 26111–26119.
269 Y. Pang, C. Su, G. Jia, L. Xu and Z. Shao, *Chem. Soc. Rev.*, 2021, **50**, 12744–12787.
270 Y. Zhao, Z. Niu, J. Zhao, L. Xue, X. Fu and J. Long, *Recent Advancements in Photoelectrochemical Water Splitting for Hydrogen Production*, Springer Nature Singapore, 2023, vol. 6.
271 W. Zhang, Z. Jin and Z. Chen, *Adv. Sci.*, 2022, **9**, 1–30.
272 A. Das, K. Panigrahi and P. Howli, *Catal. Today*, 2023, **423**, 113979.
273 Y. He, M. Wang, L. Zhang, Q. Cheng, S. Liu, X. Sun, Y. Jiang, T. Qian and C. Yan, *Adv. Funct. Mater.*, 2024, 2315548.
274 K. Chen, X. Xu, Q. Mei, J. Huang, G. Yang and Q. Wang, *Appl. Catal., B*, 2024, **341**, 123299.
275 S. Lin, J. B. Ma, J. J. Fu, L. Sun, H. Zhang, J. Cheng and J. F. Li, *J. Phys. Chem. C*, 2023, **127**, 1345–1354.
276 P. Gnanasekar, K. Peramaiah, H. Zhang, M. K. Eswaran, R. R. Pradhan, U. Schwingenschlögl, T. K. Ng, Q. Gan, J. Kulandaivel, K.-W. Huang and B. S. Ooi, *ACS Appl. Energy Mater.*, 2023, **6**, 10784–10793.
277 R. Karimi, F. Yousefi, M. Ghaedi, K. Dashtian and G. Yasin, *J. Environ. Chem. Eng.*, 2022, **10**, 108549.
278 W. Ye, C. He, M. A. Mushtaq, K. Lin and X. Xing, *Eur. J. Inorg. Chem.*, 2022, e202200325.
279 M. A. Mushtaq, A. Kumar, G. Yasin, M. Arif, M. Tabish, S. Ibraheem, X. Cai, W. Ye, X. Fang, A. Saad, J. Zhao, S. Ji and D. Yan, *Appl. Catal., B*, 2022, **317**, 121711.
280 N. Gao, H. Yang, D. Dong, D. Dou, Y. Liu, W. Zhou, F. Gao, C. Nan, Z. Liang and D. Yang, *J. Colloid Interface Sci.*, 2022, **611**, 294–305.
281 L. P. Camargo, P. R. C. da Silva, A. Batagin-Neto, V. Klobukoski, M. Vidotti and L. H. Dall'Antonia, *Appl. Mater. Today*, 2022, **28**, 101540.
282 Y. Bai, H. Bai, Z. Fang, X. Li, W. Fan and W. Shi, *Chem. Commun.*, 2021, **57**, 10568–10571.
283 Y. Bai, J. Lu, H. Bai, Z. Fang, F. Wang, Y. Liu, D. Sun, B. Luo, W. Fan and W. Shi, *Chem. Eng. J.*, 2021, **414**, 128773.
284 K. Bi, Y. Wang, D. M. Zhao, J. Z. Wang, D. Bao and M. M. Shi, *J. Mater. Chem. A*, 2021, **9**, 10497–10507.
285 J. Zheng, Y. Lyu, J. P. Veder, B. Johannessen, R. Wang, R. De Marco, A. Huang, S. P. Jiang and S. Wang, *J. Phys. Chem. C*, 2021, **125**, 23041–23049.
286 M. A. Mushtaq, M. Arif, X. Fang, G. Yasin, W. Ye, M. Basharat, B. Zhou, S. Yang, S. Ji and D. Yan, *J. Mater. Chem. A*, 2021, **9**, 2742–2753.
287 M.-H. Vu, C.-C. Nguyen and T.-O. Do, *ACS Sustainable Chem. Eng.*, 2020, **8**, 12321–12330.
288 D. Liu, J. Wang, S. Bian, Q. Liu, Y. Gao, X. Wang, P. K. Chu and X. F. Yu, *Adv. Funct. Mater.*, 2020, **30**, 1–7.
289 M. Li, Q. Lu, M. Liu, P. Yin, C. Wu, H. Li, Y. Zhang and S. Yao, *ACS Appl. Mater. Interfaces*, 2020, **12**, 38266–38274.
290 W. Ye, M. Arif, X. Fang, M. A. Mushtaq, X. Chen and D. Yan, *ACS Appl. Mater. Interfaces*, 2019, **11**, 28809–28817.
291 Y. Bai, H. Bai, K. Qu, F. Wang, P. Guan, D. Xu, W. Fan and W. Shi, *Chem. Eng. J.*, 2019, **362**, 349–356.
292 Y. Liu, H. Bai, Q. Zhang, Y. Bai, X. Pang, F. Wang, Y. Yang, J. Ding, W. Fan and W. Shi, *Chem. Eng. J.*, 2021, **413**, 127453.
293 E. Skúlason, T. Bligaard, S. Gudmundsdóttir, F. Studt, J. Rossmeisl, F. Abild-Pedersen, T. Vegge, H. Jónsson and J. K. Nørskov, *Phys. Chem. Chem. Phys.*, 2012, **14**, 1235–1245.
294 D. V. J. Li, Y. Zhang, C. Liu, L. Zheng, E. Petit, K. Qi, Y. Zhang, H. Wu, W. Wang, A. Tiberj, X. Wang, M. Chhowalla, L. Lajaunie and R. Yu, *Adv. Funct. Mater.*, 2021, **32**, 2108316.
295 K. Y. C. Lim, H. Roh, E. H. Kim, H. Kim, T. Park and D. Lee, *Small*, 2023, 2304274.
296 S. K. Singh, R. K. Rai and D. Tyagi, *Eur. J. Inorg. Chem.*, 2017, 2450–2456.
297 S. Xu, D. C. Ashley, H. Y. Kwon, G. R. Ware, C. H. Chen, Y. Losovyj, X. Gao, E. Jakubikova and J. M. Smith, *Chem. Sci.*, 2018, **9**, 4950–4958.
298 A. Stirling, I. Pápai, J. Mink and D. R. Salahub, *J. Chem. Phys.*, 1994, **100**, 2910–2923.
299 E. E. Van Tamelen and B. Akermark, *J. Am. Chem. Soc.*, 1968, **90**, 4492–4493.
300 G. Marnellos and M. Stoukides, *Science*, 1998, **282**, 98–100.
301 K. Kim, C.-Y. Yoo, J.-N. Kim, H. C. Yoon and J.-I. Han, *J. Electrochem. Soc.*, 2016, **163**, F1523.
302 L. M. Wilder, K. Wyatt, C. A. Skangos, W. E. Klein, M. R. Parimuha, J. L. Katsirubas, J. L. Young and E. M. Miller, *ACS Appl. Energy Mater.*, 2024, **7**, 536–545.
303 D. Mateo, J. L. Cerrillo, S. Durini and J. Gascon, *Chem. Soc. Rev.*, 2021, **50**, 2173–2210.
304 M. Gao, T. Zhang and G. W. Ho, *Nano Res.*, 2022, **15**, 9985–10005.
305 Y. Peng, J. Albero, A. Franconetti, P. Concepción and H. García, *ACS Catal.*, 2022, **12**, 4938–4946.
306 Y. Peng, A. Melillo, R. Shi, A. Forneli, A. Franconetti, J. Albero and H. García, *Appl. Catal., B*, 2023, **339**, 123143.
307 X. Li, X. Zhang, H. O. Everitt and J. Liu, *Nano Lett.*, 2019, **19**, 1706–1711.
308 X. Bian, Y. Zhao, G. I. N. Waterhouse, Y. Miao, C. Zhou, L. Z. Wu and T. Zhang, *Angew. Chem., Int. Ed.*, 2023, **62**, 1–8.
309 J. Zheng, L. Lu, K. Lebedev, S. Wu, P. Zhao, I. J. McPherson, T.-S. Wu, R. Kato, Y. Li, P.-L. Ho, G. Li, L. Bai, J. Sun, D. Prabhakaran, R. A. Taylor, Y.-L. Soo, K. Suenaga and S. C. E. Tsang, *Chem. Catal.*, 2021, **1**, 162–182.
310 C. Mao, J. Wang, Y. Zou, Y. Shi, C. J. Viasus, J. Y. Y. Loh, M. Xia, S. Ji, M. Li, H. Shang, M. Ghoussoub, Y. F. Xu, J. Ye, Z. Li, N. P. Kherani, L. Zheng, Y. Liu, L. Zhang and G. A. Ozin, *J. Am. Chem. Soc.*, 2023, **145**, 13134–13146.
311 S. Wang, W. Yu, S. Xu, K. Han and F. Wang, *ACS Sustainable Chem. Eng.*, 2022, **10**, 115–123.
312 C. Mao, L. Yu, J. Li, J. Zhao and L. Zhang, *Appl. Catal., B*, 2018, **224**, 612–620.
313 W. K. Fan and M. Tahir, *Chem. Eng. J.*, 2022, **427**, 131617.

314 L. F. Greenlee, J. N. Renner and S. L. Foster, *ACS Catal.*, 2018, **8**, 7820–7827.
315 Y. Zhao, F. Wu, Y. Miao, C. Zhou, N. Xu, R. Shi, L. Wu, J. Tang and T. Zhang, *Angew. Chem.*, 2021, **133**, 21896–21899.
316 Y. Zhao, R. Shi, X. Bian, C. Zhou, Y. Zhao, S. Zhang, F. Wu, G. I. N. Waterhouse, L. Z. Wu, C. H. Tung and T. Zhang, *Adv. Sci.*, 2019, **6**, 1802109.
317 M. Li, H. Huang, J. Low, C. Gao, R. Long and Y. Xiong, *Small Methods*, 2018, 1800388.
318 K. Wang, D. Smith and Y. Zheng, *Carbon Resour. Convers.*, 2018, **1**, 2–31.
319 M. Kolen, W. A. Smith and F. M. Mulder, *ACS Omega*, 2021, **6**, 5698–5704.
320 G. W. Watt and J. D. Chrisp, *Anal. Chem.*, 1952, **24**, 2006–2008.
321 S. J. Yuan, J. J. Chen, Z. Q. Lin, W. W. Li, G. P. Sheng and H. Q. Yu, *Nat. Commun.*, 2013, **4**, 2249.
322 Y. Shiraishi, M. Hashimoto, K. Chishiro, K. Moriyama, S. Tanaka and T. Hirai, *J. Am. Chem. Soc.*, 2020, **142**, 7574–7583.
323 C. Gal, W. Frenzel and J. Möller, *Microchim. Acta*, 2004, **146**, 155–164.
324 P. Griess, *Ber. Dtsch. Chem. Ges.*, 1879, **12**, 426–428.
325 M. J. Moorcroft, J. Davis and R. G. Compton, *Talanta*, 2001, **54**, 785–803.
326 A. Machado, G. Marshall, A. A. Bordalo and R. B. R. Mesquita, *Anal. Methods*, 2017, **9**, 1876–1884.
327 G. F. Chen, S. Ren, L. Zhang, H. Cheng, Y. Luo, K. Zhu, L. X. Ding and H. Wang, *Small Methods*, 2019, **3**, 1–20.
328 Y. Shiraishi, S. Shiota, Y. Kofuji, M. Hashimoto, K. Chishiro, H. Hirakawa, S. Tanaka, S. Ichikawa and T. Hirai, *ACS Appl. Energy Mater.*, 2018, **1**, 4169–4177.
329 B. M. Comer, P. Fuentes, C. O. Dimkpa, Y. H. Liu, C. A. Fernandez, P. Arora, M. Realff, U. Singh, M. C. Hatzell and A. J. Medford, *Joule*, 2019, **3**, 1578–1605.
330 S. Z. Andersen, V. Čolić, S. Yang, J. A. Schwalbe, A. C. Nielander, J. M. McEnaney, K. Enemark-Rasmussen, J. G. Baker, A. R. Singh, B. A. Rohr, M. J. Statt, S. J. Blair, S. Mezzavilla, J. Kibsgaard, P. C. K. Vesborg, M. Cargnello, S. F. Bent, T. F. Jaramillo, I. E. L. Stephens, J. K. Nørskov and I. Chorkendorff, *Nature*, 2019, **570**, 504–508.
331 J. Choi, B. H. R. Suryanto, D. Wang, H. Du, R. Y. Hodgetts, F. M. F. Vallana, D. R. Macfarlane and A. N. Simonov, *Nat. Commun.*, 2020, **11**(5546), 1–10.
332 L. Li, C. Tang, D. Yao, Y. Zheng and S. Z. Qiao, *ACS Energy Lett.*, 2019, **4**, 2111–2116.
333 P. W. Huang and M. C. Hatzell, *Nat. Commun.*, 2022, **13**, 1–7.
334 E. Truszkiewicz, W. Raróg-Pilecka, K. Schmidt-Szałowski, S. Jodzis, E. Wilczkowska, D. Łomot, Z. Kaszkur, Z. Karpiński and Z. Kowalczyk, *J. Catal.*, 2009, **265**, 181–190.
335 L.-M. Kwedi-Nsah and T. Kobayashi, *Ultrason. Sonochem.*, 2020, **66**, 105051.
336 L. Collado, P. Reñones, J. Fermoso, F. Fresno, L. Garrido, V. Pérez-Dieste, C. Escudero, M. D. Hernández-Alonso, J. M. Coronado, D. P. Serrano and V. A. de la Peña O'Shea, *Appl. Catal., B*, 2022, **303**, 120931.
337 G. Chehade and I. Dincer, *Fuel*, 2021, **299**, 120845.
338 D. R. Strongin and G. A. Somorjai, Surface Science and Catalytic Study of the Effects of Aluminum Oxide and Potassium on the Ammonia Synthesis Over Iron Single-Crystal Surfaces, in *Catalytic Ammonia Synthesis: Fundamentals and Practice*, ed. J. R. Jennings, Springer US, 1991, ch. 4, pp. 133–177.
339 A. Patonia, *Ammonia as a storage solution for future decarbonized energy systems*, 2020.
340 S. Giddey, S. P. S. Badwal, C. Munnings and M. Dolan, *ACS Sustainable Chem. Eng.*, 2017, **5**, 10231–10239.
341 A. Valera-Medina, F. Amer-Hatem, A. K. Azad, I. C. Dedoussi, M. De Joannon, R. X. Fernandes, P. Glarborg, H. Hashemi, X. He, S. Mashruk, J. McGowan, C. Mounaim-Rouselle, A. Ortiz-Prado, A. Ortiz-Valera, I. Rossetti, B. Shu, M. Yehia, H. Xiao and M. Costa, *Energy Fuels*, 2021, **35**, 6964–7029.
342 J. W. Makepeace, T. J. Wood, H. M. A. Hunter, M. O. Jones and W. I. F. David, *Chem. Sci.*, 2015, **6**, 3805–3815.
343 M. E. Solutions, Unlocking ammonia's potential for shipping, **https://www.man-es.com/discover/two-stroke-ammonia-engine**.
344 Wärtsilä, AMMONIA 2-4 project, **https://www.ammonia2-4.eu/**.
345 A. E. Association, *Ammonia fueled sports car: Marangoni Toyota GT86 Eco Explorer*, **https://www.ammoniaenergy.org/articles/ammonia-fueled-sports-car-marangoni-toyota-gt86-eco-explorer/**.
346 International Energy Agency, Net Zero by 2050: *A Roadmap for the Global Energy Sector*, 2021.
347 JERA, JERA and IHI to Start a Demonstration Project Related to Ammonia Co-firing at a Large-Scale Commercial Coal-Fired Power Plant, **https://www.jera.co.jp/en/news/information/20210524_677**.
348 N. Morlanés, S. P. Katikaneni, S. N. Paglieri, A. Harale, B. Solami, S. M. Sarathy and J. Gascon, *Chem. Eng. J.*, 2021, **408**, 127310.
349 N. Salmon and R. Bañares-Alcántara, *Sustainable Energy Fuels*, 2021, **5**, 2814–2839.
350 K. Smart, *Johnson Matthey Technol. Rev.*, 2021, 230–244.
351 L. Ye, R. Nayak-Luke, R. Bañares-Alcántara and E. Tsang, *Chemistry*, 2017, **3**, 712–714.
352 A. E. Association, H2biscus: green ammonia in Malaysia, **https://www.ammoniaenergy.org/articles/h2biscus-green-ammonia-in-malaysia/**.
353 Ammonia Energy Association, Blue ammonia in the Northern Territory & Wyoming, **https://www.ammoniaenergy.org/articles/blue-ammonia-in-the-northern-territory-wyoming/**.
354 Ammonia Energy Association, $4.5 billion blue ammonia project in Louisiana, **https://www.ammoniaenergy.org/articles/4-5-billion-blue-ammonia-project-in-louisiana/**.
355 Ammonia Energy Association, "Jordan Green Ammonia": a new ammonia partnership in the Middle East, **https://www.ammoniaenergy.org/articles/jordan-green-ammonia-a-new-ammonia-partnership-in-the-middle-east/**.

356 G. Centi and S. Perathoner, *Green Chem.*, 2023, **26**, 15–41.
357 O. A. Ojelade, S. F. Zaman and B. J. Ni, *J. Environ. Manage.*, 2023, **342**, 118348.
358 Clean Ammonia in the Future Energy System. Hydrogen Europe., 2023.
359 Kapsom, The World's First Green Ammonia Plant Was Made By Kapsom., **https://www.kapsom.com/the-worlds-first-green-ammonia-plant-was-made-by-kapsom/#:~:text=Green ammonia produced from renewable,to a renewable energy drive**.
360 ENGIE-YARA, Renewable Hydrogen and Ammonia Deployment in Pilbara. YURI Phase 0: Feasibility study public report, 2020.
361 H2F *project. Green hydrogen, green ammonia and green fertiliser plant*, **https://www.fertiberia.com/en/amoniacoverde/h2f-project/**.
362 CEPSA, *Cepsa and Fertiberia form a strategic alliance to boost green hydrogen production and decarbonize industry in Huelva*., **https://www.cepsa.com/en/press/cepsa-and-fertiberia-will-produce-green-hydrogen**.
363 Kapsom, The First 2,*000 TPA Green Ammonia Pilot Project in South America*, **https://www.kapsom.com/the-first-**2000-tpa-green-ammonia-pilot-project-in-south-america/ (**http://-tpa-green-ammonia-pilot-project-in-south-america/**).
364 H. Liu, *Chin. J. Catal.*, 2014, **35**, 1619–1640.
365 S. A. Nosherwani and R. C. Neto, *J. Energy Storage*, 2021, **34**, 102201.
366 The World Bank indicators.
367 USGS, historical-statistics-mineral-and-material-commodities. *Nitrogen*.
368 Nitrogen (fixed) ammonia statistics.
369 USGS.
370 W. Bank, Worls Bank Commodity Prices.
371 Statista, Distribution of agricultural fertilizer production capacity worldwide in 2021, by region.
372 R. F. Service, *Science*, 2018, **361**, 120–123.
373 OECD/IEA, Tracking industrial energy efficiency and CO_2 emissions, Paris, 2007.
374 D. Saygin, H. Blanco, F. Boshell, J. Cordonnier, K. Rouwenhorst, P. Lathwal and D. Gielen, *Sustainability*, 2023, 15.
375 M. Wang, M. A. Khan, I. Mohsin, J. Wicks, A. H. Ip, K. Z. Sumon, C. T. Dinh, E. H. Sargent, I. D. Gates and M. G. Kibria, *Energy Environ. Sci.*, 2021, **14**, 2535–2548.
376 K. H. R. Rouwenhorst, P. M. Krzywda, N. E. Benes, G. Mul and L. Lefferts, *Ammonia Production Technologies, Techno-Economic Challenges of Green Ammonia as an Energy Vector*, Elsevier Inc., 2021, ch. 4, pp. 41–83.
377 V. Kyriakou, I. Garagounis, A. Vourros, E. Vasileiou and M. Stoukides, *Joule*, 2020, **4**, 142–158.
378 A. Raghuveer and Tejasvi Wilczewski, *Today in Energy*, 2022.
379 S. Canel Soria and S. Soh, Analysis: Global ammonia prices fall 50% on year, sparking concerns over future low-carbon market, **https://cilive.com/commodities/energy-transition/thought-leadership/082323-conflive-analysis-global-ammonia-prices-fall**.
380 G. Hochman, A. S. Goldman, F. A. Felder, J. M. Mayer, A. J. M. Miller, P. L. Holland, L. A. Goldman, P. Manocha, Z. Song and S. Aleti, *ACS Sustainable Chem. Eng.*, 2020, **8**, 8938–8948.
381 A. Makhlouf, T. Serradj and H. Cheniti, *Environ. Impact Assess. Rev.*, 2015, **50**, 35–41.
382 N. Morlanés, S. P. Katikaneni, S. N. Paglieri, A. Harale, B. Solami, S. M. Sarathy and J. Gascon, *Chem. Eng. J.*, 2021, **408**, 127310.
383 G. Schnitkey, Farmdoc Dly.
384 J. Bartels, PhD thesis, Iowa State University, 2008.
385 UNIDO & IFCD, *Fertilizer Manual*, Kluwer Academic Publisher, 1998.
386 T. A. Czuppon, S. A. Knez and J. M. Rovner, in *Kirk-Othmer Encyclopedia of Chemical Technology*, ed. C. Ley, Ammonia, Wiley, 5th edn, 2000.
387 D. Frattini, G. Cinti, G. Bidini, U. Desideri, R. Cioffi and E. Jannelli, *Renewable Energy*, 2016, **99**, 472–482.
388 D. Saygin and D. Gielen, *Energies*, 2021, 14.
389 Our World in Data, Electricity production by source, *World*.
390 Enerdata, World Energy & Climate Statistics-Yearbook 2022.
391 A. Faaij, *Mitig. Adapt. Strateg. Glob. Chang.*, 2006, **11**, 343–375.
392 D. B. Pal, A. Singh and A. Bhatnagar, *Int. J. Hydrogen Energy*, 2022, **47**, 1461–1480.
393 B. Parkinson, P. Balcombe, J. F. Speirs, A. D. Hawkes and K. Hellgardt, *Energy Environ. Sci.*, 2019, **12**, 19–40.
394 S. G. Nnabuife, J. Ugbeh-Johnson, N. E. Okeke and C. Ogbonnaya, *Carbon Capture Sci. Technol.*, 2022, **3**, 100042.
395 J. R. Bartels, M. B. Pate and N. K. Olson, *Int. J. Hydrogen Energy*, 2010, **35**, 8371–8384.
396 P. Arora, A. F. A. Hoadley, S. M. Mahajani and A. Ganesh, *Ind. Eng. Chem. Res.*, 2016, **55**, 6422–6434.
397 P. Gilbert, S. Alexander, P. Thornley and J. Brammer, *J. Cleaner Prod.*, 2014, **64**, 581–589.
398 P. Tunå, C. Hulteberg and S. Ahlgren, *Environ. Prog. Sustainable Energy*, 2014, **33**, 1290–1297.
399 J. Andersson and J. Lundgren, *Appl. Energy*, 2014, **130**, 484–490.
400 L. Tock, F. Maréchal and M. Perrenoud, *Can. J. Chem. Eng.*, 2015, **93**, 356–362.
401 J. Armijo and C. Philibert, *Int. J. Hydrogen Energy*, 2020, **45**, 1541–1558.
402 X. Liu, A. Elgowainy and M. Wang, *Green Chem.*, 2020, **22**, 5751–5761.
403 J. Ikäheimo, J. Kiviluoma, R. Weiss and H. Holttinen, *Int. J. Hydrogen Energy*, 2018, **43**, 17295–17308.
404 P. H. Pfromm, *J. Renew. Sustainable Energy*, 2017, **9**, 34702.
405 H2view, Plug Power reveals record production of 122MW PEM electrolyser stacks in Q1.
406 Y. Ishimoto, M. Voldsund, P. Nekså, S. Roussanaly, D. Berstad and S. O. Gardarsdottir, *Int. J. Hydrogen Energy*, 2020, **45**, 32865–32883.
407 M. H. Hasan, T. M. I. Mahlia, M. Mofijur, I. M. Rizwanul Fattah, F. Handayani, H. C. Ong and A. S. Silitonga, A comprehensive review on the recent development of

ammonia as a renewable energy carrier, *Energies*, 2021, **14**, 3732.
408 A. H. Reksten, M. S. Thomassen, S. Møller-Holst and K. Sundseth, *Int. J. Hydrogen Energy*, 2022, **47**, 38106–38113.
409 G. Bristowe and A. Smallbone, *Hydrogen*, 2021, **2**, 273–300.
410 A. Sánchez and M. Martín, *Sustainable Prod. Consum.*, 2018, **16**, 176–192.
411 C. Kost, S. Shammugam, V. Jülch, H.-T. Nguyen and T. Schlegl, Levelized cost of electricity, *Renewable Energy Technol.*, 2018.
412 Z. Cesaro, M. Ives, R. Nayak-Luke, M. Mason and R. Bañares-Alcántara, *Appl. Energy*, 2021, **282**, 116009.
413 K. H. R. Rouwenhorst, A. G. J. Van der Ham and L. Lefferts, *Int. J. Hydrogen Energy*, 2021, **46**, 21566–21579.
414 M. Yoshida, T. Ogawa, Y. Imamura and K. N. Ishihara, *Int. J. Hydrogen Energy*, 2021, **46**, 28840–28854.
415 H. Zhang, L. Wang, J. Van herle, F. Maréchal and U. Desideri, *Appl. Energy*, 2020, **259**, 114135.
416 R. Bañares-Alcántara, G. Dericks, M. Fiaschetti, G. Philipp, L. Joaquín Masa, E. Tsang, Y. Aidong, Y. Lin and Z. Shangyi, *Analysis of Islanded Ammonia-based Energy Storage Systems*, Oxford, 2015.
417 M. Matzen, M. Alhajji and Y. Demirel, *J. Adv. Chem. Eng.*, 2015, **5**, 3.
418 V. Parmar, J. Manwell and J. McGowan, *J. Phys. Conf. Ser.*, 2020, **1452**, 012015.
419 ISPT, Power to Ammonia: Feasibility study for the value chains and business cases to produce CO2-free ammonia suitable for various market applications (REF TESI115001), 2017.
420 G. Wang, A. Mitsos and W. Marquardt, *AIChE J.*, 2017, **63**, 1620–1637.
421 E. R. Morgan, J. F. Manwell and J. G. McGowan, *ACS Sustainable Chem. Eng.*, 2017, **5**, 9554–9567.
422 A. Sánchez and M. Martín, *J. Clean. Prod.*, 2018, **178**, 325–342.
423 M. Rivarolo, G. Riveros-Godoy, L. Magistri and A. F. Massardo, *ChemEngineering*, 2019, 3.
424 R. Nayak-Luke, R. Bañares-Alcántara and I. Wilkinson, *Ind. Eng. Chem. Res.*, 2018, **57**, 14607–14616.
425 A. Allman, M. J. Palys and P. Daoutidis, *AIChE J.*, 2019, **65**, e16434.
426 B. Lin, T. Wiesner and M. Malmali, *ACS Sustainable Chem. Eng.*, 2020, **8**, 15517–15531.
427 O. Osman, S. Sgouridis and A. Sleptchenko, *J. Cleaner Prod.*, 2020, **271**, 121627.
428 M. J. Palys and P. Daoutidis, *Comput. Chem. Eng.*, 2020, **136**, 106785.
429 C. Quintero-Masselski, J.-F. Portha and L. Falk, *Chem. Eng. Res. Des.*, 2022, **177**, 826–842.
430 N. Campion, H. Nami, P. R. Swisher, P. Vang Hendriksen and M. Münster, *Renewable Sustainable Energy Rev.*, 2023, **173**, 113057.
431 O. Elishav, D. R. Lewin, G. E. Shter and G. S. Grader, *Appl. Energy*, 2017, **185**, 183–188.
432 P. Mayer, A. Ramirez, G. Pezzella, B. Winter, S. M. Sarathy, J. Gascon and A. Bardow, *iScience*, 2023, **26**, 107389.
433 V. N. Sagel, K. H. R. Rouwenhorst and J. A. Faria, *Renewable Sustainable Energy Rev.*, 2022, **161**, 112381.
434 V. N. Sagel, K. H. R. Rouwenhorst and J. A. Faria, *Energies*, 2022, 15.
435 M. Fasihi, R. Weiss, J. Savolainen and C. Breyer, *Appl. Energy*, 2021, **294**, 116170.
436 N. Salmon and R. Bañares-Alcántara, *J. Clean. Prod.*, 2022, **367**, 133045.
437 K. H. R. Rouwenhorst, P. M. Krzywda, N. E. Benes, G. Mul and L. Lefferts, *Ullmann's Encycl. Ind. Chem.*, 2020, 1–20.
438 I. C. Ten Have, *Feeding and fueling a greener future: everything you need to know about green ammonia*.
439 A. Patil, L. Laumans and H. Vrijenhoef, *Procedia Eng.*, 2014, **83**, 322–327.
440 C. A. Fernandez and M. C. Hatzell, *J. Electrochem. Soc.*, 2020, **167**, 143504.
441 J. M. McEnaney, A. R. Singh, J. A. Schwalbe, J. Kibsgaard, J. C. Lin, M. Cargnello, T. F. Jaramillo and J. K. Nørskov, *Energy Environ. Sci.*, 2017, **10**, 1621–1630.
442 F. B. Juangsa, A. R. Irhamna and M. Aziz, *Int. J. Hydrogen Energy*, 2021, **46**, 14455–14477.
443 B. Yang, W. Ding, H. Zhang and S. Zhang, *Energy Environ. Sci.*, 2021, **14**, 672–687.
444 Z.-H. Xue, S.-N. Zhang, Y.-X. Lin, H. Su, G.-Y. Zhai, J.-T. Han, Q.-Y. Yu, X.-H. Li, M. Antonietti and J.-S. Chen, *J. Am. Chem. Soc.*, 2019, **141**, 14976–14980.
445 H. He, Q. Q. Zhu, Y. Yan, H. W. Zhang, Z. Y. Han, H. Sun, J. Chen, C. P. Li, Z. Zhang and M. Du, *Appl. Catal., B*, 2022, **302**, 120840.
446 M. Wang, S. Liu, T. Qian, J. Liu, J. Zhou, H. Ji, J. Xiong, J. Zhong and C. Yan, *Nat. Commun.*, 2019, **10**, 341.
447 Y. Liu, Q. Li, X. Guo, X. Kong, J. Ke, M. Chi, Q. Li, Z. Geng and J. Zeng, *Adv. Mater.*, 2020, **32**, 1907690.
448 Y. Liu, L. Huang, X. Zhu, Y. Fang and S. Dong, *Nanoscale*, 2020, **12**, 1811–1816.
449 M. A. Mushtaq, M. Arif, G. Yasin, M. Tabish, A. Kumar, S. Ibraheem, W. Ye, S. Ajmal, J. Zhao, P. Li, J. Liu, A. Saad, X. Fang, X. Cai, S. Ji and D. Yan, *Renewable Sustainable Energy Rev.*, 2023, **176**, 113197.
450 Y. Bicer and I. Dincer, *Int. J. Hydrogen Energy*, 2019, **44**, 18875–18890.
451 J. R. Gomez, J. Baca and F. Garzon, *Int. J. Hydrogen Energy*, 2020, **45**, 721–737.
452 V. Kyriakou, I. Garagounis, E. Vasileiou, A. Vourros and M. Stoukides, *Catal. Today*, 2017, **286**, 2–13.
453 Y. Bicer and I. Dincer, *ACS Sustainable Chem. Eng.*, 2017, **5**, 8035–8043.
454 N. C. Kani, A. Prajapati and M. R. Singh, *ACS ES&T Eng.*, 2022, **2**, 1080–1087.
455 J. H. Guo, X. J. Liu, Y. Zhang, J. L. Shen, W. X. Han, W. F. Zhang, P. Christie, K. W. T. Goulding, P. M. Vitousek and F. S. Zhang, *Science*, 2010, **327**, 1008–1010.
456 Y. Wei, W. Jiang, Y. Liu, X. Bai, D. Hao and B. J. Ni, *Nanoscale*, 2022, **14**, 2990–2997.

457 A. J. Medford and M. C. Hatzell, *ACS Catal.*, 2017, **7**, 2624–2643.
458 S. M. Swarbreck, M. Wang, Y. Wang, D. Kindred, R. Sylvester-Bradley, W. Shi, Varinderpal-Singh, A. R. Bentley and H. Griffiths, *Trends Plant Sci.*, 2019, **24**, 892–904.
459 Fertilizer consumption (kilograms per hectare of arable land)—World, 2021.
460 R. Einarsson, A. Sanz-Cobena, E. Aguilera, G. Billen, J. Garnier, H. J. M. van Grinsven and L. Lassaletta, *Sci. Data*, 2021, **8**, 288.
461 W. Adalibieke, X. Cui, H. Cai, L. You and F. Zhou, *Sci. Data*, 2023, **10**, 617.
462 World Bank, Fertilizer consumption (kilograms per hectare of arable land)—China, 2021.
463 K. Smart, *Johnson Matthey Technol. Rev.*, 2022, **66**, 230–244.
464 M. R. Shaner, H. A. Atwater, N. S. Lewis and E. W. McFarland, *Energy Environ. Sci.*, 2016, **9**, 2354–2371.
465 J. Osorio-Tejada, N. N. Tran and V. Hessel, *Sci. Total Environ*, 2022, **826**, 154162.